Estimation and Mapping of Ship Airwake Using RC Helicopters as a Sensing Platform

Anil Kumar

Dissertation submitted to the faculty of the Virginia Polytechnic Institute and State University in partial fulfillment of the requirements for the degree of

Doctor of Philosophy
In
Mechanical Engineering

Pinhas Ben-Tzvi, Chair
Craig A. Woolsey
Alfred L. Wicks
Kevin B. Kochersberger
Andrew J. Kurdila

February 26, 2018
Blacksburg, Virginia

Keywords: Ship Airwake, Helicopter Dynamics, Artificial Neural Networks, Active Particle Filters, Extended Kalman Filter, Particle Swarm Optimization, Indoor Motion Tracking, Wind Mapping, Wireless Telemetry

Estimation and Mapping of Ship Airwake Using RC Helicopters as a Sensing Platform

Anil Kumar

ABSTRACT

This dissertation explores the applicability of RC helicopters as a tool to map wind conditions. This dissertation presents the construction of a robust instrumentation system capable of wireless in-situ measurement and mapping of ship airwake. The presented instrumentation system utilizes an RC helicopter as a carrier platform and uses the helicopter's dynamics for spatial 3D mapping of wind turbulence. The system was tested with a YP676 naval training craft to map ship airwake generated in controlled heading wind conditions. Novel system modelling techniques were developed to estimate the dynamics of an instrumented RC helicopter, in conjunction with onboard sensing, to estimate spatially varying (local) wind conditions. The primary problem addressed in this dissertation is the reliable estimation and separation of pilot induced dynamics from the system measurements, followed by the use of the dynamics residuals/discrepancies to map the wind conditions.

This dissertation presents two different modelling approaches to quantify ship airwake using helicopter dynamics. The helicopter systems were characterized using both machine learning and analytical aerodynamic modelling approaches. In the machine learning based approaches, neural networks, along with other models, were trained then assessed in their capability to model dynamics from pilot inputs and other measured helicopter states. The dynamics arising from the wind conditions were fused with the positioning estimates of the helicopter to generate ship airwake maps which were compared against CFD generated

airwake patterns. In the analytical modelling based approach, the dynamic response of an RC helicopter to a spatially varying parameterized wind field was modeled using a 30-state nonlinear ordinary differential equation-based dynamic system, while capturing essential elements of the helicopter dynamics. The airwake patterns obtained from both types of approach were compared against anemometrically produced wind maps of turbulent wind conditions artificially generated in a controlled indoor environment.

Novel hardware architecture was developed to acquire data critical for the operation and calibration of the proposed system. The mechatronics design of three prototypes of the proposed system were presented and performance evaluated using experimental testing with a modified YP676 naval training vessel in the Chesapeake Bay area. In closing, qualitative analysis of these systems along with potential applications and improvements are discussed to conclude this dissertation.

Estimation and Mapping of Ship Airwake Using RC Helicopters as a Sensing Platform

Anil Kumar

GENERAL AUDIENCE ABSTRACT

Ship airwake is a trail of wind turbulence left behind the superstructure of cruising naval vessels and are considered as a serious safety concern for aviators during onboard operations. Prior knowledge of the airwake distribution around the ship can alert pilots of possible hazards ahead of time and mitigate operational risks during the launch and recovery of the aircraft on the flight deck. This dissertation presents a novel application of Remote Control (RC) helicopters as tools to measure and map ship airwake.

This dissertation presents two approaches to extract wind conditions from helicopter dynamics: (1) using machine learning based modeling, and (2) using analytic aerodynamic modeling-based estimation. Machine Learning is a modern engineering tool to model and simulate any system using experimental data alone. Under the machine learning based approach, the helicopter's response to pilot inputs was modeled using multiple algorithms, with experimental flight data collected the absence of the ship airwake. With an assumption of capturing all the aerodynamic effects with the machine learning algorithms, the deviations in the dynamics estimates during testing environment were used to characterize and map ship airwake. In contrast to the machine learning model, the analytical approach modeled all critical aerodynamic processes of the RC helicopter as functions of pilot inputs and wind conditions using well defined physics laws, thus eliminating any need for training data. This approach predicts wind conditions on the basis of the model's capability to match the estimates of helicopter dynamics to the actual measurements.

Both presented approaches were tested on wind conditions created in indoor and outdoor environments. The performance of the proposed system was evaluated in experimental testing with a modified YP676 naval training vessel in the Chesapeake Bay area. The dissertation also presents the mechatronic design details of the novel hardware prototypes and subsystems used in the various studies and experiments. Finally, qualitative analysis of these systems along with their potential applications and improvements are discussed to conclude this dissertation.

ACKNOWLEDGEMENTS

I would like to thank several people who made this research possible. First, I would like to express my deepest gratitude to my advisor Dr. Pinhas Ben-Tzvi for his continued support and guidance. I would like to thank the members of my doctoral committee Dr. Pinhas Ben-Tzvi, Dr. Craig Woolsey, Dr. Alfred Wicks, Dr. Kevin Kochersberger and Dr. Andrew J. Kurdila for their constructive comments. I would like to thank Office of Naval Research (ONR) for their support of this work under the "USNA Ship Airwake Program" (Code 351). I owe special thanks to Dr. Murray R. Snyder of the George Washington University and the United States Naval Academy for his guidance and support to this work. I am thankful to YP676 crew, USNA, Davison Army Airfield and Virginia Tech Athletics Department for assistance with experimentation and data collection.

I would also like to thank my current and former colleagues Adam Williams, Bijo Sebastian, Hailin Ren, Sina Aghli, Vinaykarthik Kamidi, Wael Saab, William Rone and Zhou Ma for their friendship and support. I am thankful to my fourth-grade science teacher Mrs. Anita Kapoor for motivating me to pursue my higher studies in science and engineering. Lastly, I am very grateful to my parents and family for their tremendous amount of love and support over the years.

DEDICATION

This dissertation is dedicated to

My Grandparents: Late. Sh. Goverdhan Dass Sonkaria and Smt. Ganga Devi

My Parents: Sh. Bhanwar Singh and Smt. Kamlesh Sonkaria

My Siblings. Dr. Vikas Kumar Sonkaria and Ms. Poonam Bala

TABLE OF CONTENTS

ABSTRACT ii

GENERAL AUDIENCE ABSTRACT iv

ACKNOWLEDGEMENTS v

DEDICATION vii

TABLE OF CONTENTS viii

LIST OF FIGURES xiii

LIST OF TABLES xix

NOMENCLATURE xx

CHAPTER 1: INTRODUCTION 1

1.1 Background 1

1.2 Literature Review 3

1.2.1 Wind Tunnel Testing 3

1.2.2 In-Situ measurements using anemometers: 5

1.2.3 Other in-situ measurement approaches: 6

1.2.4 Statement of Contributions 9

1.3 Dissertation Structure 10

1.4 Selected Publications 12

CHAPTER 2: PRILIMINARY STUDIES 14

2.1 RC Helicopters as Sensing Platform 14
2.1.1 Spatial Distribution of Helicopter Dynamics 14
2.1.2 Automated Airwake Analysis 17
2.1.3 Pilot Input Compensation 20
2.1.4 Back Propagation Neural Network Architecture 21
2.1.5 Airwake Measurement 25
2.2 Wireless Telemetry Approach 27
2.2.1 System Implementation 32
2.2.2 Network Training and Pilot Inputs Compensation 34
2.2.3 Airwake Distribution 38
2.3 Other Machine Learning Approaches: 40
2.3.1 System Architecture 41
2.3.2 System Modeling 43
2.3.3 System Training 44
CHAPTER 3: INDOOR MOTION TRACKING AND WIND MAPPING 50
3.1 3D Wind Mapping Methods: 50
3.2 Indoor Positioning Systems Review: 51
3.2.1 Marker-less Camera-based Tracking 52
3.2.2 Marker-based Tracking 52
3.3 Proposed Indoor Motion Tracking System 53

3.3.1 Tracking System Implementation 54

3.3.2 Data Fusion using EKF for 3D Position and Attitude Tracking 62

3.3.3 Tracking System Evaluation 69

3.4 Wind Map Generation 73

CHAPTER 4: WIND ESTIMATION FROM RC HELICOPTER USING CALIBRATED NEURAL NETS 78

4.1 Interaction between Helicopter and Ship Airwake 79

4.1.1 Pilot Inputs 81

4.1.2 Aerodynamic Loading and Helicopter Dynamics 81

4.2 Telemetry System Hardware 86

4.2.1 Rover Module 87

4.2.2 Base Module 88

4.3 System Training 89

4.3.1 Feed Forward Network 90

4.3.2 Particle Swarm Optimization 91

4.3.3 Training Neural Networks using PSO 92

4.4 RC Helicopter as an Airwake Sensor 94

4.4.1 System Calibration 94

4.4.2 Frequency Response 96

4.4.3 Accuracy Assessment 97

4.5 Interaction between RC Helicopter and Ship Airwake 99

4.5.1 Airwake Flow Conditions 100

4.5.2 System Performance 101

4.6 Direct Estimation of Wind conditions using Neural Network 104

4.6.1 Modeling Background 104

4.6.2 System Training and Results 106

CHAPTER 5: WIND ESTIMATION USING RC HELCIOPTER AERODYNAMICS MODEL 110

5.1 Helicopter Dynamics and Airwake 111

5.1.1 Nonlinear Helicopter Flight Dynamics Model 111

5.1.2 Main Rotor Dynamics 115

5.1.3 Tail Rotor Dynamics 118

5.1.4 Fuselage/Empennage Dynamics 119

5.1.5 Stabilizer/Flybar Dynamics 120

5.2 Telemetry System and Experimental Setup 121

5.3 Model Parameters Optimization 124

5.4 Wind Estimation and Results 129

5.4.1 Active Particle Filters 130

5.4.2 Wind Estimation using APF 131

5.4.3 Results and Discussions 132

CHAPTER 6: CONCLUSION AND FUTURE WORK 136

6.1 Summary 136

6.2 System Limitations and Future Work 138

REFERENCES 140

LIST OF FIGURES

Figure 1.1: Typical 3D flow geometry in backward facing step similar to ship airwake [1]. 1

Figure 1.2: Launch and recovery envelopes for MH-60S helicopters on USS Ticonderoga (CG 47) class cruiser [2]. 2

Figure 1.3: Existing wind tunnel setups for ship airwake analysis: (A) Bardera-Mora et al. [14]; (B) Snyder et al [3]; (C) Guedes et al.[15]; (D) Polsky et al [7]; (E) Wadcock et al. [16]; (F) Kääriä et al. [17]. 4

Figure 1.4: In situ airwake measurement using anemometers: (A) Bardera-Mora et al. [14]; (B) Snyder et al [3]; (C) Mallon et al. and Gamagedara et al. [19], [20]; (D) Guedes et al. [15]. 6

Figure 1.5: Wind conditions estimation using quadrotors: (A) Hardware Setup, (B) Quadrotor flying next to anemometer [24]. 7

Figure 1.6: Wind conditions estimation using fixed wing: (A) UAV [25], (B) Glider [26]. 8

Figure 1.7: Dense wind mapping sensors: (A) Wind LiDAR; (B) SoDAR [27]. 8

Figure 2.1: Radio controlled instrumented helicopter flying astern of YP676 in the Chesapeake Bay [22]. 15

Figure 2.2: Measured airwake location (blue dashed lines) and CFD simulation (colored background) for: (A) $\beta = 15°$, (B) $\beta = 30°$ at the top of the hangar structure. 16

Figure 2.3: Pitch and roll gyroscopic data along a flight path into the airwake. Dashed line indicates time at which the helicopter entered the wake. 17

Figure 2.4: Sample processing of IMU data. Upper figure is raw data (green) plus low pass filtered data (blue) and local standard deviation (red). Lower figure shows processed data. 19

Figure 2.5: Hypothesized airwake data A_ω for β = 0° plotted over helicopter relative position with identified local peaks. 20

Figure 2.6: Experimental Setup: (A) YP676 training vessel (Top); (B) Instrumented RC Helicopter on Deck; (C) Pilot Input Receiver; (D) IMU and GPS sensor (Bottom). 21

Figure 2.7: Histogram for prediction error of the neural network [11]. 24

Figure 2.8: Predicted gyroscope data overlaid on actual measurements [11]. A good overlap between predicted and measured angular rate is observed. 25

Figure 2.9: Ship airwake distribution for test flights with: (A) β = 0°; (B) β = 15° [11]. 27

Figure 2.10: Interaction of airwake with helicopter resulting in tilting [30] 28

Figure 2.11: Schematics of the wireless telemetry system [30]. 31

Figure 2.12: Hardware schematics of sensor modules [30]..... 33

Figure 2.13: Hardware Setup: (A) Helicopter fitted with Data Package and Flotation system; (B) Data package with transmitter module inside; (C) Transmitter module (Top); (D) Transmitter module (Bottom); (E) Receiver module [30]..... 33

Figure 2.14: Topology of Neural Networks used in WTS [30]. 35

Figure 2.15: Prediction by neural networks corresponding to Heli 1 (showing 25 seconds of data) [30]..... 37

Figure 2.16: Error distributions for the prediction by the neural networks corresponding to the three helicopters [30]. 38

Figure 2.17: GUI for proposed wireless telemetry system [30]. 39

Figure 2.18: Ship airwake distribution (with airwake zones marked using black dashed lines) for: (a) test flight with beta angle of 0 °, (b) test flight with beta angle of 15° with skewness observed towards right [30]. 40

Figure 2.19: Telemetry System hardware setup[28]..... 42

Figure 2.20: (A) Experimental Setup; (B) Free body diagram of helicopter [28]. 43

Figure 2.21: Topology of BME used in proposed telemetry system [28]. 47

Figure 2.22: Prediction error distribution for all the three algorithms [28]. 48

Figure 2.23: Prediction results from all the three machine learning algorithms [28]..... 49

Figure 3.1: LOSA 3D tracking system: (A) Front View; (B) Rear View with cover removed; (C) CAD of sensor module arm [67]. 55

Figure 3.2: CAD model of the LOSA sensor assembly [67]. 55

Figure 3.3: Field of view of a LOSA sensor module with three slots [67]..... 57

Figure 3.4: IR LED light source (Active Marker) with controller [67]. 59

Figure 3.5: Schematics of the proposed tracking system..... 60

Figure 3.6: Peak Detection: (A) Raw data from one sensor module; (B) Estimated peak position on zoomed peak area. 61

Figure 3.7: LOSA sensor pair geometry for triangulation [67]. 62

Figure 3.8: Experimental Setup with coordinate frames (mounting plates are parallel and face each other) (A) tracking system; (B) Active LED marker [67]. 65

Figure 3.9: LabVIEW GUI for the LOSA tracking system [67]. 68

Figure 3.10: Positional accuracy and resolution of the LOSA sensor at different operating ranges [67]: (A) Position Estimates; (B) Sensor Positioning Error; (C) Sensor Tracking Resolution 70

Figure 3.11: Comparison of EKF output with raw positional estimates [67]. 71

Figure 3.12: Dynamic orientation measurement with VN200 INS and proposed LOSA tracking system [67]..... 72

Figure 3.13: (A) Wind mapping setup [77]; (B) Ultrasonic anemometer; (C) Electrical schematics. 73

Figure 3.14: Validation of steady state wind model: (A) Spatial distribution of modeling error; (B) Histogram distribution of model error as a percentage of input wind. 75

Figure 3.15: Indoor wind flow map: (A) 3D steady-state wind flow with turbulence map; (B) Sectional view of the 3D flow field at plane X=0; (C) Zoomed-in flow field. 76

Figure 4.1: (A) Frame of reference assignment for the helicopter's fuselage and rotor blades; (B) Aerodynamic loads on an airfoil section of rotor blade [79] 80

Figure 4.2: Factors affecting helicopter dynamics (angular rates) [79]..... 85

Figure 4.3: Telemetry System hardware setup: (A) Rover Module (Bottom view with cover removed); (B) Base module (Rearview without cover) [79]. 86

Figure 4.4: Electrical Schematics of: (A) Rover Module, and (B) Base Module [79]. ... 87

Figure 4.5: Proposed Network Topology [79]. 90

Figure 4.6: Mean Absolute Error v/s Iteration count for PSO-NN [79]. 93

Figure 4.7: PSO-NN prediction results for pitch and roll accelerations and prediction error distribution [79]. 93

Figure 4.8: Helicopter response to wind turbulence, (A) Local (standard) deviation of the angular acceleration residuals; (B) Wind turbulence map [79]. 95

Figure 4.9: Calibration of angular acceleration residuals for estimation of wind turbulence [79]. 96

Figure 4.10: Frequency response of the helicopter's angular acceleration to cyclic (swash plate) rotor input. 97

Figure 4.11: Proposed system's wind turbulence measurement error distribution..... 98

Figure 4.12: Outdoor testing: (A) Telemetry system operating from YP676 flight deck; (B) YP676 as seen from the RC helicopter [79] 99

Figure 4.13: Ship airwake distribution: (A) CFD model simulation results with experimental trajectory overlaid; (B) Experimentally determined turbulence distribution [79]..... 101

Figure 4.14: Turbulence map comparison: (A) CFD mean flow simulation results; (B) Experimental ship airwake map; (C) Turbulence cross-correlation [77]..... 103

Figure 4.15: Neural Network prediction results (blue) with measured estimates (red) for wind vorticity [77]. 107

Figure 4.16: Neural Network output error distribution [77]. 108

Figure 4.17: Wind vorticity patterns: (A) Predicted Vorticity along X axis; (B) Measured Vorticity along X axis; (C) Predicted Vorticity along Y axis; (D) Measured Vorticity along Y axis [77]..... 109

Figure 5.1: Coordinate system for the proposed helicopter model [87]. 112

Figure 5.2: Helicopter dynamics models and subsystems [87]. 113

Figure 5.3: Helicopter's equivalent shape and aerodynamic drag surfaces [87]. 119

Figure 5.4: Hardware Setup for the presented study [87]. 121

Figure 5.5: Electrical Schematics of (A) Rover Module; (B) Base Module [87] 122

Figure 5.6: Experimental setup for the presented study [87]..... 123

Figure 5.7: Model optimization results: (A) Modelling Error Progression; (B) Model Error Distribution; (C) Model output along with pilot inputs (u) [87]..... 128

Figure 5.8: Wind Mapping Experiment: (A) Experiment setup; (B) Wind Map [87]... 130

Figure 5.9: Mean wind flow map using: (A) Proposed system; (B) Anemometer[87] . 132

Figure 5.10: Vorticity wind flow map using: (A) Proposed system; (B) Anemometer [87]. 133

Figure 5.11: Mean flow and vorticity estimation error distribution. 134

LIST OF TABLES

Table 2.1: BPNN Network Topologies 36

Table 2.2: BPNN Prediction RMS Error (deg/s) 37

Table 2.3: BPNN Network Topologies 46

Table 3.1: Relationship between sensor height and field of view 58

Table 5.1: Helicopter Model Initial Variables/Parameters 126

Table 5.2: Helicopter Model Variables/Parameters after Optimization 127

Table 5.3: Mean Flow and Vorticity Estimation Error Statistics 135

NOMENCLATURE

u, v, w	=	Translational velocities of helicopter in aircraft frame (m/s)
p, q, r	=	Angular rates of the helicopter fuselage in the aircraft frame (rad/s)
θ, φ, ψ	=	Attitude (Euler angles) of the helicopter fuselage (deg)
M_H	=	Mass of the helicopter (kg)
Ω	=	Nominal rotor speed (rad/s)
R	=	Main rotor length (m)
$I_{xx}, I_{yy}, I_{zz}, I_{xz}$	=	Moment of Inertia components ($kg.m^2$)
ψ_b	=	Rotor azimuth positon (rad)
θ_b	=	Main rotor blade pitch angle (rad)
θ_T	=	Tail rotor blade pitch angle
$\theta_0, \theta_c, \theta_s$	=	Main rotor blade pitch collective and cyclic components
δ	=	Commanded rotor blade pitch angle (rad)
a_0	=	Aerodynamic lift coefficient
δ_0, δ_2	=	Aerodynamic drag coefficients
ρ	=	Air Density (kg/m^3)
c	=	Main rotor blade chord length (m)
γ	=	Lock Number
χ	=	Inflow wake angle (rad)
$\lambda_0, \lambda_c, \lambda_s$	=	Rotor inflow collective and cyclic components
g	=	Acceleration due to gravity (m/s^2)
R_T	=	Tail rotor length (m)

β_b	=	Main rotor flapping angle (rad)
$\beta_0, \beta_c, \beta_s$	=	Main rotor flapping coefficients
ζ_b	=	Main rotor lead-lag angle (rad)
$\zeta_0, \zeta_c, \zeta_s$	=	Main rotor lead-lag angle components
A_d	=	Main rotor disk area (m^2)
A_{dT}	=	Tail rotor disk area (m^2)
I_β, I_ζ	=	Moment of Inertia of Rotor Blade ($kg.m^2$)
K_β, K_ζ	=	Equivalent spring constant for blade flapping and lead/lag (N.m/rad)
C_X, C_Y, C_Z	=	Equivalent fuselage drag coefficients ($N.s^2/m^2$)
C_{VF}, C_{VF}	=	Equivalent empennage drag coefficients ($N.s^2/m^2$)
N_b	=	Number of rotor blades
β	=	Incident wind over deck azimuthal angle (deg)
v_x, v_y, v_z	=	Local steady state wind flow estimates (m/s)
$\omega_x, \omega_y, \omega_z$	=	Local wind vorticity estimates (s^{-1})
e_ζ	=	Normalized main rotor hinge offset
μ	=	Helicopter forward advance ratio
μ_z	=	Axial advance ratio
γ_f	=	Flybar lock number
η_2	=	Flybar thrust scaling factor
c_1, c_2	=	Fractional contribution of swashplate and flybar in rotor pitch
q_0, q_1, q_2, q_3	=	Attitude quaternion components
A_ω	=	Airwake (equivalent gyroscope) data
CFD	=	Computational Fluid Dynamics

IMU	=	Inertial Measurement Unit
INS	=	Inertial Navigation System
BPNN	=	Back Propagation Neural Network
ANFIS	=	Adaptive Neuro Fuzzy Inference System
LOSA	=	Linear Optical Sensors Array
BME	=	Bayesian Mixture of Experts
PSO	=	Particle Swarm Optimization
EKF	=	Extended Kalman Filter
APF	=	Active Particle Filter

CHAPTER 1: INTRODUCTION

1.1 Background

Launch and recovery of rotary wing aircraft from naval vessels is one of the most challenging and potentially hazardous tasks in aviation operations. In addition to the limited area of the flight deck and ship's motion in the rough sea, the unsteady nature of the wind flow conditions increases the pilot's workload many-folds. This trail of wind turbulence left behind by the superstructure of cruising naval vessels is often referred to as ship airwake. The interactions of the ship airwake with the rotor generated wakes further complicate the helicopter dynamics. Figure 1.1 shows general flow geometry associated with 3D backward facing step (similar to naval vessel geometry) [1].

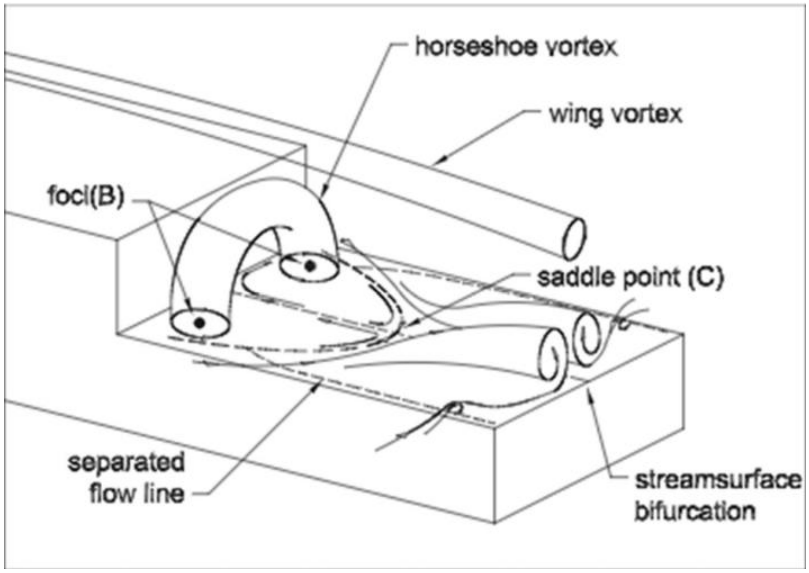

Figure 1.1: Typical 3D flow geometry in backward facing step similar to ship airwake [1].

Safe ‘launch and recovery’ envelopes (in terms of limiting the vessel speed) are often prescribed depending on the class of the vessel and the onboard operating aircraft to mitigate these operational risks [2]. Figure 1.2 shows one of such launch and recovery envelopes for MH-60S helicopters on USS Ticonderoga (CG 47) class navy cruiser ship.

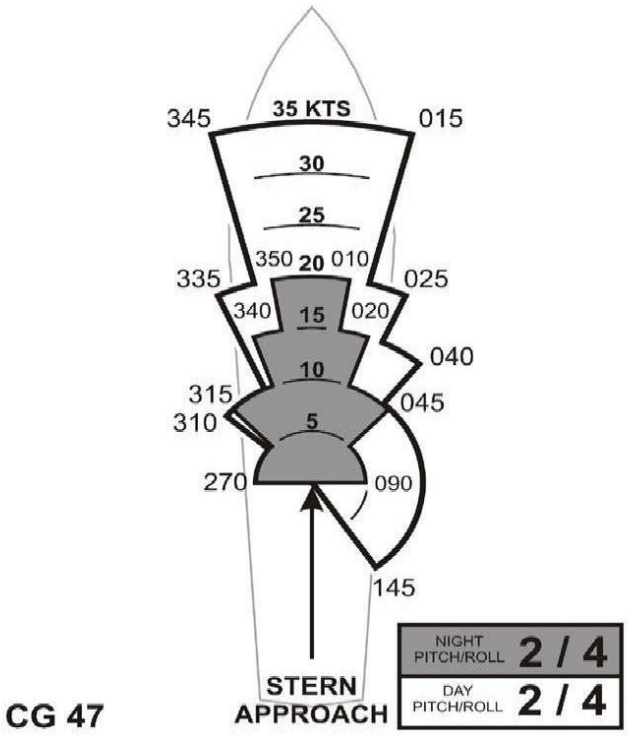

Figure 1.2: Launch and recovery envelopes for MH-60S helicopters on USS Ticonderoga (CG 47) class cruiser [2].

Figure 1.2 shows maximum allowed relative wind over the flight deck for different directions of approach of the concerned helicopter towards the flight deck area. Here, the radial markings denote the wind over the deck (in knots), and the azimuthal markings represent the direction of approach (in degrees) relative to the stern (from the rear to the front) direction of the vessel. As shown in the figure, the maximum allowed wind over the deck has been limited depending on the path of approach and lighting conditions to keep the ship airwake within safe limits. Such launch and recovery envelopes are often obtained

using intensive test flights by the test pilot's assessment of airwake (e.g., whether or not excessive flight control inputs are required to land on the flight deck safely). This type of flight testing is not only expensive but also difficult to schedule, potentially hazardous and above all, highly subjective. To overcome this issue, Computational Fluid Dynamics (CFD) model are being developed which require experimental data for validation and refinement [3]. The simplest solution to such issues is the complementary use of computational tools to predict test conditions and extrapolate test results, thereby reducing the number of actual flight test points required [4]–[10]. However, current computational methods are insufficiently validated for ships with a complex superstructure, such as a destroyer or cruiser [11], [12]. Validated computational airwake predictions can not only be used for ship design and operational safety analysis but also for building autonomy in control for shipboard operations [13]. Therefore, there is a need for non-subjective systems for experimental validations of CFD models for airwake patterns.

1.2 Literature Review

To obtain experimental ship airwake data, most researchers have pursued either wind tunnel testing or relied on in-situ wind velocity measurements using anemometers.

1.2.1 Wind Tunnel Testing

Wind tunnel testing has been the preliminary and most common source for ship airwake measurement in the naval science community. Such studies often use a scaled-down model of naval vessels in wind tunnel and measure wind flow field. These types of setups have used a variety of sensing modalities including laser Doppler anemometry [1], [14], hot wire

based Omniprobe anemometry [3], [7] and Particle Image Velocimetry [15], [16]. In a similar study, Kääriä et al. immersed a model helicopter in a water tunnel to validate the aerodynamic interactions of a helicopter with ship airwake [17].

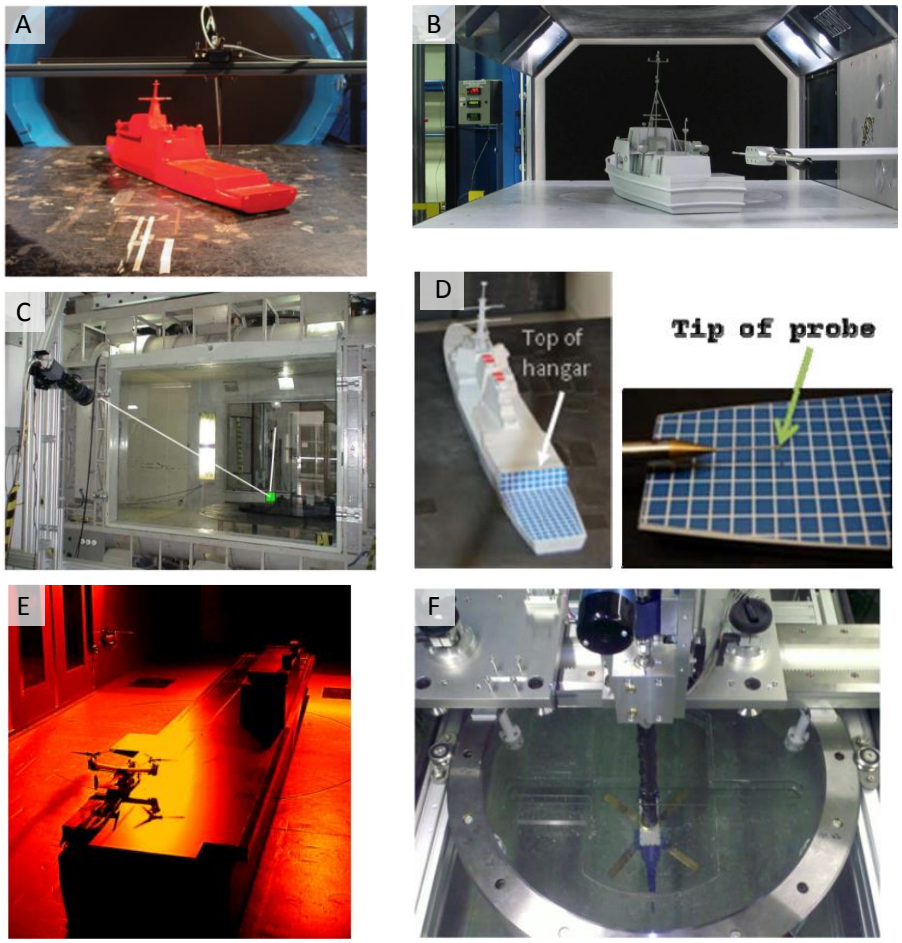

Figure 1.3: Existing wind tunnel setups for ship airwake analysis: (A) Bardera-Mora et al. [14]; (B) Snyder et al [3]; (C) Guedes et al.[15]; (D) Polsky et al [7]; (E) Wadcock et al. [16]; (F) Kääriä et al. [17].

Figure 1.3 shows a few examples of wind tunnels testing setups used by the researchers for ship airwake analysis. The transducers used in these measurements are very sensitive and expensive, so they can safely be operated only in controlled environments like wind tunnels. The wind tunnel testing does provide significant insight into wind flow in ship airwake zones, but lacks fine details in flow pattern due to scaling issues. Additionally,

both the model holder and the walls of wind tunnel affect the readings, and their effects must be accounted for in the experimentation.

1.2.2 In-Situ measurements using anemometers:

Use of anemometers is the most common means for in-situ wind pattern measurement. Allotta et al. have recently demonstrated use of MEMS sensor based low cost anemometers mounted on a sail boat mast to measure wind flow for autonomous control of the boat [18]. The sensor gives good temporal resolution but lacks spatial resolution as it depends on the motion and dynamics of the sailboat. However, in a more reliable approach, researchers placed ultrasonic anemometers at different locations on the flight deck of naval vessels and compared the measurements with CFD/wind tunnel testing results [3], [12], [14], [19]–[21]. This methodology did provide accurate wind flow measurements but proved to be expensive and time-consuming. The anemometer(s) needed to be moved from point to point to get the complete wind flow field. Figure 1.4 shows a few examples of anemometer-based ship airwake mapping systems.

To overcome this limitation, Mallon et al. [22], [23] in a similar study used airborne anemometers mounted on a quadrotor to map ship airwake (Figure 1.4C). This approach required compensation for the anemometers' motion relative to the inertial frame of reference and, most importantly, was susceptible to interaction with quadrotor generated wind wakes. Furthermore, the quadrotor's velocity accuracy limited the accuracy of the airwake measurement.

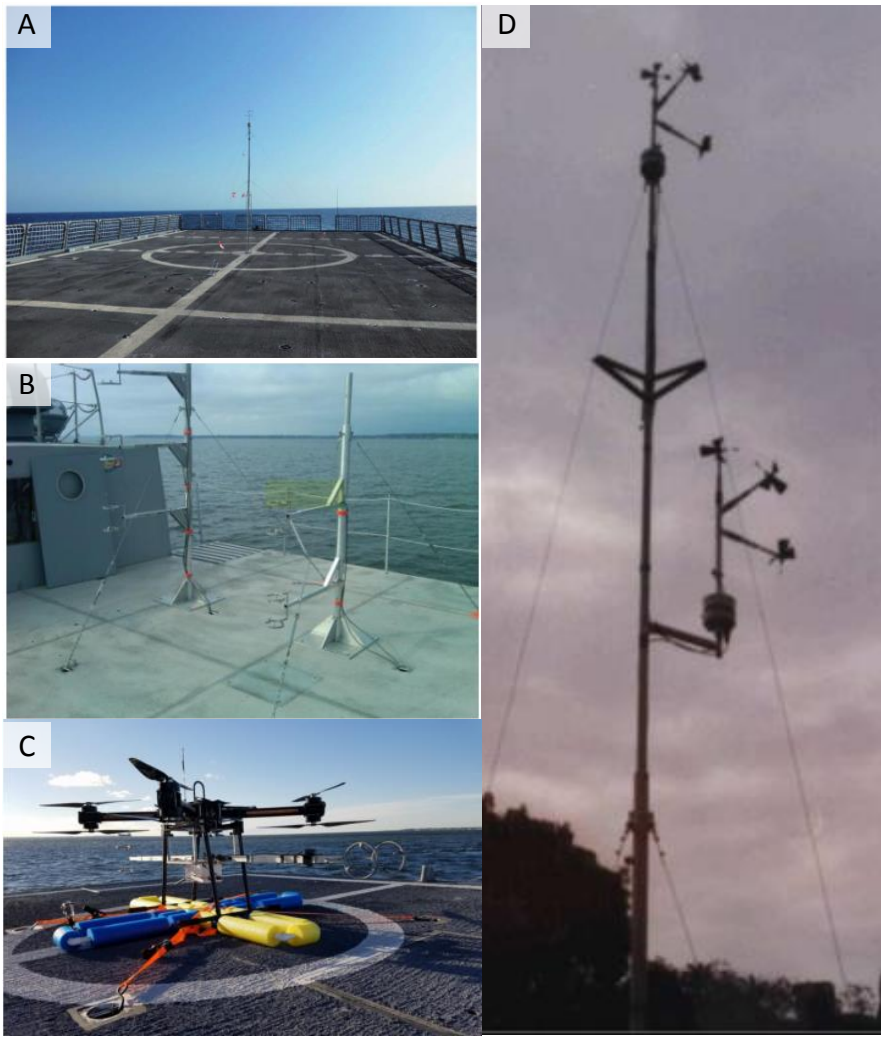

Figure 1.4: In situ airwake measurement using anemometers: (A) Bardera-Mora et al. [14]; (B) Snyder et al [3]; (C) Mallon et al. and Gamagedara et al. [22], [23]; (D) Guedes et al. [15].

1.2.3 Other in-situ measurement approaches:

In recent approaches, researchers have tried to explore the use of the dynamics of small unmanned aerial vehicles (UAVs) for the characterization of wind turbulence. Gonzalez-Rocha et al. in [24] demonstrated the use of a small quadrotor's motion to measure atmospheric winds (Figure 1.5). They used kinematic filtering based approach for the estimation of the mean flow field by comparing the system's velocity estimates to the UAV

velocity measurements (received from the GPS autopilot) using vector triangulation. Their system can also be used to measure ship airwake. However, it focused only on the mean component of the ambient wind flow. In addition to this, high rotor disk loading for quadrotors decreases its hovering efficiency, which limits its capability in terms of sensor payload and endurance.

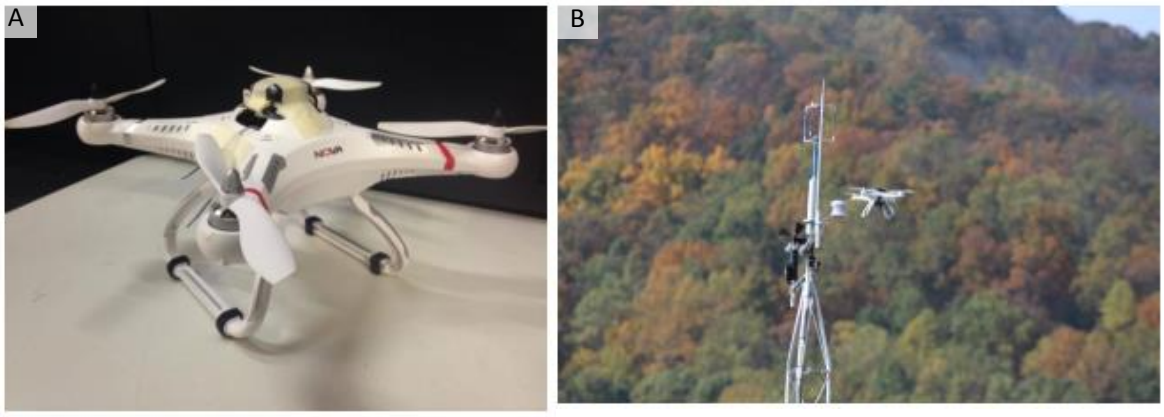

Figure 1.5: Wind conditions estimation using quadrotors: (A) Hardware Setup, (B) Quadrotor flying next to anemometer [24].

In a similar manner, Phelps et al. explored the use of dynamics of an instrumented fixed-wing UAVs for mapping ship airwake [25]. They flew the UAV in the lee of the superstructure of a cruising naval vessel and tried to map ship airwake through deviations in the acceleration (from the aerodynamic lift/drag) of the aircraft. This approach can be used to map airwake in large volumes. However, the absence of hovering capabilities reduces the temporal resolution of the system. On a similar track, Rodriguez et al. explored the use of fixed-wing RC gliders for the characterization and mapping of atmospheric wind [26].

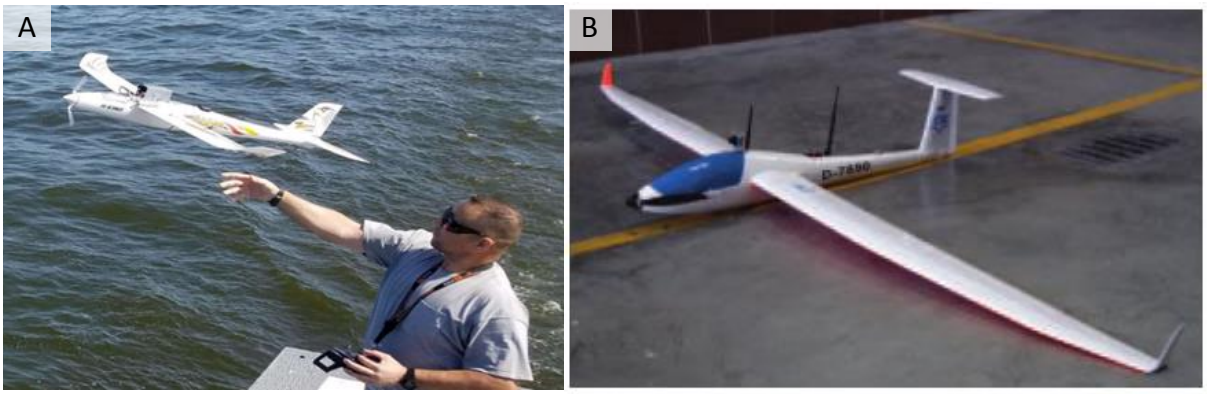

Figure 1.6: Wind conditions estimation using fixed wing: (A) UAV [25], (B) Glider [26].

In a different approach, use of dense wind profiling sensors such as Wind-LiDAR (Light Detection and Ranging) and SoDAR (Sound Detection and Ranging) (as shown in Figure 1.7) is theoretically possible, but these sensors are impractical for estimating ship airwake due to technological limitations. With the existing technologies, these sensors are bulky (size of the order of 1m) and massive (>50kg). As a result of which, these sensors (especially SoDARs) are only suitable for vertical profiling of atmospheric wind. Horizontal profiling of wind (as needed for ship airwake mapping) is possible using wind LiDARs, but limited field of view and lower sensing range of wind lidars requires significant distance between the laser sensor and area of interest (flight deck). The limited size of naval vessels restrains the use of LiDARs for horizontal wind profiling while avoiding direct laser reflections from the ground/sea surface.

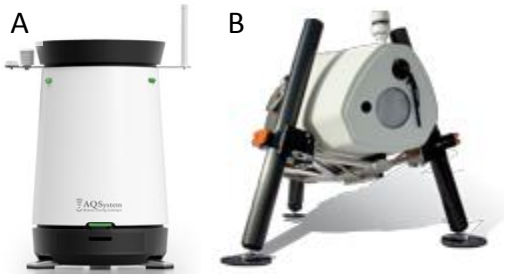

Source: http://www.ammonit.com/en/produkte/sodar-lidar

Figure 1.7: Dense wind mapping sensors: (A) Wind LiDAR; (B) SoDAR [27].

1.2.4 Statement of Contributions

In contrast to other existing techniques, this dissertation explores the applicability of RC helicopters in the estimation and mapping of ship airwake. The hovering capabilities of the RC helicopters, combined with their low cost and long operational range, make them a great transducer to determine wind conditions. The large rotor disc area and low mass make them sensitive to the dynamic effects of ship airwake.

This dissertation presents a hypothesis that the dynamics of an RC helicopter, after isolating the pilot induced components, can be used for the estimation and mapping of the ship airwake. To experimentally validate this hypothesis, this dissertation presents the design and integration of two wireless telemetry system prototypes to capture the helicopter dynamics in action. Both telemetry system prototypes were unique in terms of the onboard sensor technologies and performance characteristics. In addition to the telemetry systems, one prototype for the indoor wind calibration system with the novel positioning system is also presented in this dissertation. Machine learning and analytical aerodynamic modeling techniques were used to extract wind patterns using the RC helicopter dynamics. More specific contributions of this dissertation are summarized as follows:

1. A linear dynamics mixing model to demonstrate separability of pilot-induced and local wind components in the aerodynamics of the helicopter. The same property has been utilized to extract local wind conditions from the helicopter dynamics estimated using machine learning algorithms like Back Propagation Neural Networks (BPNN), Adaptive Neuro-Fuzzy Inference Systems (ANFIS) and Bayesian Mixture of Experts (BME) models.

2. Mechatronics design of a novel wireless telemetry system to simultaneously measure and record helicopter dynamics, location and pilot-inputs at a high update rate (>130 Hz).
3. A novel sensing system to generate and map reproducible wind flow conditions in a controlled indoor environment; thus, providing a means to calibrate helicopter aerodynamics models. The proposed sensing system is capable of tracking indoor motion of objects at a high update rate (>300Hz) with mm-level accuracy. This system has been used for robust motion tracking of the RC helicopter during indoor experiments.
4. A study to map wind turbulence generated by a cruising naval vessel using the proposed system and compares the map against the CFD-generated airwake patterns.
5. A novel wind–helicopter interaction model and demonstrates its application in wind flow estimation using active particle filters.

1.3 Dissertation Structure

The dissertation is organized as follows:

Chapter 1: Presents the background of this research and highlights the main contributions of this dissertation.

Chapter 2: Provides details on multiple (experimental) studies conducted to understand and explore means to extract external wind related effects in helicopter dynamics.

Chapter 3: Presents a novel opto-inertial motion tracking system and demonstrates its applicability in wind mapping and helicopter motion tracking for system calibration.

Chapter 4: Presents a Neural Networks based approach to map wind condition using RC helicopter dynamics and calibrated the system from predetermined wind flow field.

Chapter 5: Presents a novel helicopter dynamics model in spatially varying wind flow field and demonstrates applicability of this model in the estimation of local wind parameters using an active particle filtering approach.

Chapter 6: Concludes the dissertation by providing a summary of the work and a discussion about potential future work.

1.4 Selected Publications

Disclosure: Content from these publications has been used throughout this dissertation.

Journal Articles

1. **Kumar, A.,** Ben-Tzvi, P., "Estimation of Wind Conditions from RC Helicopter using Active Particle Filters", IEEE/ASME Transactions on Mechatronics, Submitted, Jan. 2018.
2. **Kumar, A**., Ben-Tzvi, P., "Novel Wireless Sensing Platform for Experimental Mapping and Validation of Ship Airwake", Mechatronics Journal, Submitted, Oct. 2017; Revised, Jan 2018, Accepted March 2018.
3. **Kumar, A.,** Ben-Tzvi, P., "Spatial Object Tracking System Based on Linear Optical Sensor Arrays", IEEE Sensors Journal , Vol.16 (22) pp.-7933-7940, Nov.15, 2016
4. **Kumar, A.,** Ben-Tzvi, P., Saab, W., Snyder, M.R., "Wireless Telemetry System for Real-time Estimation of Ship Airwake with UAVs", Mechatronics Journal, Vol. 36, pp. 18-26, April 2016

Conference Articles

1. **Kumar, A.,** Ben-Tzvi, P., "An Inertial Sensor to Measure Wind Turbulence with RC Helicopters", Proceedings of the ASME 2017 Dynamic Systems and Control Conf. (DSCC 2017), Tysons Corner, VA,Oct 11-13, 2017.
2. **Kumar, A.,** Ben-Tzvi, P., "Extraction of Impact of Wind Turbulence on RC Helicopters using Machine Learning", Proceedings of the 2016 ASME

IDETC/CIE, 40th Mechanisms & Robotics Conf., Charlotte, North Carolina, Aug..21-24, 2016.

3. **Kumar, A.,** Ben-Tzvi, P., Snyder, M.R., "UAV based Wireless Telemetry System for the Estimation of Ship Airwake Patterns", Proceedings of the 2015 ASME/IEEE Int. Conf. on Mechatronic and Embedded Systems and Applications (MESA) (IDETC/CIE 2015), Boston, MA, Aug. 2-5, 2015.
4. Snyder, M.R., **Kumar, A.,** Ben-Tzvi, P., "Off Ship Measurement of Ship Airwake Using Instrumented Unmanned Aerial Vehicles", 32nd AIAA Applied Aerodynamics Conf., AIAA Aviation and Aeronautics Forum and Exposition 2014, Atlanta, GA, 16-20 June 2014.
5. **Kumar, A.,** Ben-Tzvi, P., Snyder, M.R., "Instrumentation System for Ship Airwake Measurement", Proc. of IEEE Int. Symp. on Robotic and Sensors Environments (2013), Washington, DC, Oct. 21-23, 2013.
6. Snyder M.R., **Kumar A.,** Ben-Tzvi P. and Kang H.S., "Validation of Computational Ship Airwake for a Naval Research Vessel", 51st AIAA Aerospace sciences Meeting Including the New Horizons Forum and Aerospace Exposition, January 7 2013, Grapevine, Texas. DOI: 10.2514/6.2013-959

Patents

1. **Kumar A.,** Ben-Tzvi P., "Active 3D Motion Tracking System Using Linear Optical Sensor Arrays". U.S. Patent Application No: 15/709,766; Filed on: 9/20/2017 (Prov. App. US 62/397,503 filed on 9/21/2016)

CHAPTER 2: PRILIMINARY STUDIES

2.1 RC Helicopters as Sensing Platform

Ship airwake mapping is critical because it affects the aerodynamic operation of a helicopter. Wind sensing instruments like anemometers, Pitot tube, etc., can measure instantaneous wind conditions, but only in a tiny volume. Thus, such instruments cannot capture spatial variations in wind condition, a characteristic of turbulent flow, especially from a non-stationary platform.

Airwake interactions result in undesired swaying and tilting of helicopters due to uneven aerodynamic loading effects caused by wind turbulence. Thus, it is advantageous to use low-cost remotely operated helicopters as a transducer to determine wind conditions. Due to their low mass, RC helicopters are quite sensitive to ship airwake. The use of an RC helicopter's in-flight angular rates to quantify ship airwake was first proposed by Metzger et al. [27]. However, their approach had limitations: it ignored the motion induced by the pilot's inputs to the helicopter [28]. This concept has been extended by Kumar et al. in multiple iterations by modeling the effect of pilot inputs to the helicopter's dynamics [11], [28]–[31]. A YP676 naval vessel was used to generate ship airwake to be mapped by RC helicopters. Multiple preliminary studies were conducted to assess the sensitivity of the low mass/inertia RC helicopter to the pilot inputs and ship airwake.

2.1.1 Spatial Distribution of Helicopter Dynamics

During feasibility studies, a small remotely piloted helicopter (as shown in Figure 2.1), was flown in the aft of YP676 flight deck to find any correlation between the helicopter

and ship airwake [20]. During this study, an RC helicopter having a rotor diameter of 4.5ft (1.37m) was maneuvered through regions in the ship's airwake. The helicopter dynamics were recorded in an onboard data logger IMU. Concurrently, the relative position of the RC helicopter was estimated by comparing the GPS position of the helicopter with that of the reference ship. The relative position was determined to be accurate within one meter (approximately 3ft), [27] which is slightly smaller than the length scale of the main rotor of the helicopter. During underway flight operations the YP's craft master attempted to keep the ship under the same wind over deck condition as based upon the reference anemometer. Since winds typically shift during a given flight the craft master had to adjust ship's course to maintain an approximately constant wind over deck. Shifting winds with subsequent adjustment in ship's course explains the apparent drift of the measured wake towards the port side further aft of the flight deck.

Figure 2.1: Radio controlled instrumented helicopter flying astern of YP676 in the Chesapeake Bay [20].

The helicopter's motion was analyzed manually using video recordings of the test flights and the time instances with steep velocity gradients and noticeable changes in the

helicopter's flight path were recorded. Combining these two measurement systems, the locations of sharp gradients in the airwake can be mapped relative to the ship (accurate within one rotor diameter of the helicopter) and compared with CFD simulations of similar wind over deck configurations. Figure 2.2, shows helicopter detected flight path disturbances superimposed over CFD airwake predictions for wind heading angle (β) equal to 15° and 30°. Here, the background color represents the norm of wind vectors mean (steady state) in the simulated field. The red color represents areas with high mean flow value (representing less turbulence), whereas the blue represent regions with the low mean flow (resulting from more spatial variation in the wind flow field or ship airwake). More details on this CFD study are presented in Chapter 4 of this dissertation.

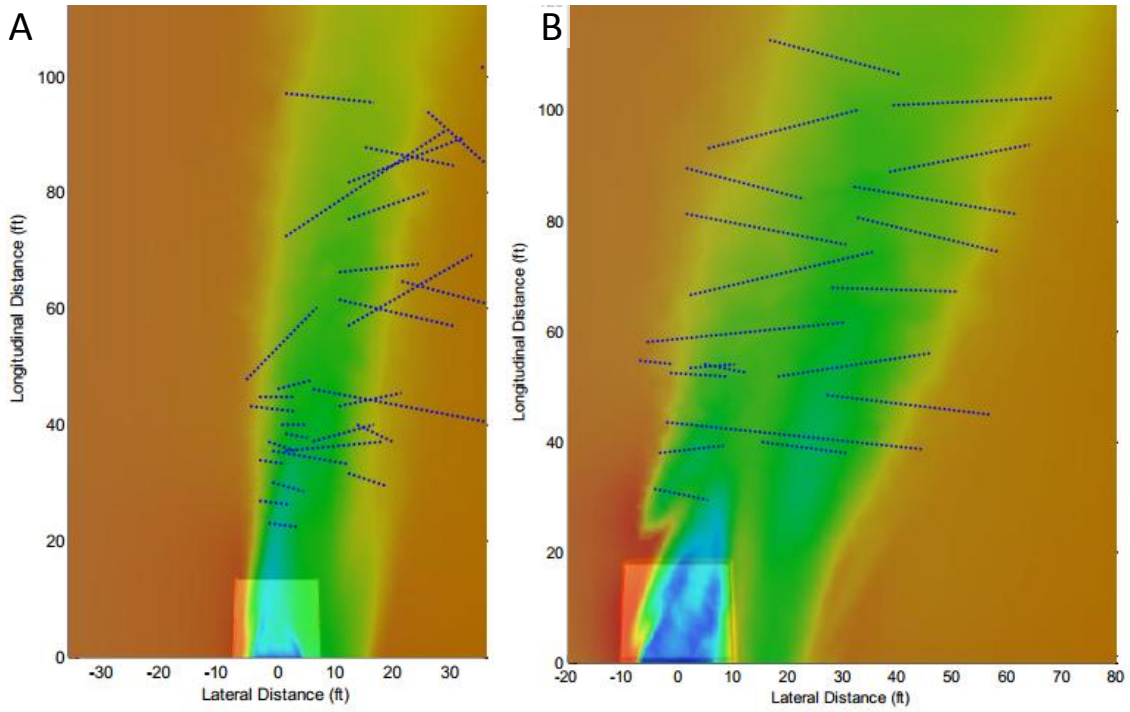

Figure 2.2: Measured airwake location (blue dashed lines) and CFD simulation (colored background) for: (A) β = 15°, (B) β = 30° at the top of the hangar structure.

When the helicopter encountered the ship airwake there was a noticeable increase in flight path disturbances, as measured by the IMU (Fig. 2.3), due to interaction with the

airwake. Such instances were accompanied with high angular rates measurements and higher variation in angular rates (which can be characterized using standard deviations). This encouraged us to use the product of the magnitude of the angular rate vector and local standard deviation of the magnitude of the angular rate vector as a metric for ship airwake. Also, it was observed that the regions with high airwake (marked on Figures 2.2) show good correlation between the location of the YP's airwake from the CFD simulations versus what was measured by the IMU onboard the helicopter during underway testing.

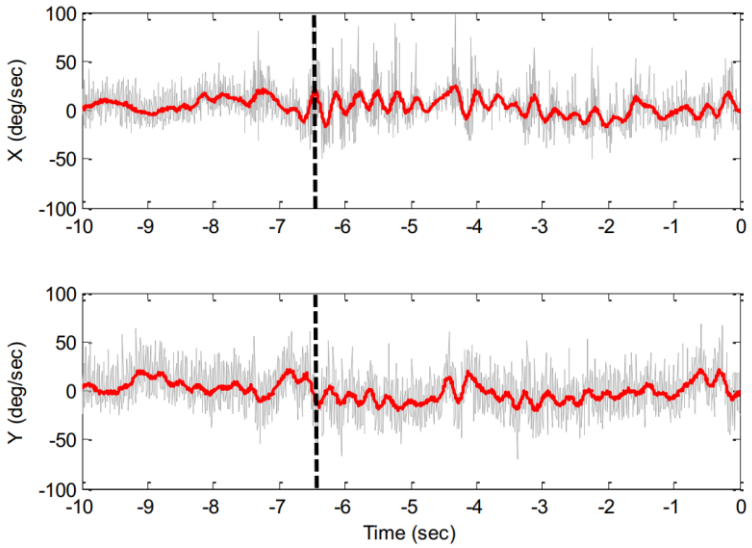

Figure 2.3: Pitch and roll gyroscopic data along a flight path into the airwake. Dashed line indicates time at which the helicopter entered the wake.

However this data analysis method was dependent upon manual review of all data, which is very time consuming and can be subjective.

2.1.2 Automated Airwake Analysis

In order to reduce the subjective nature of the off ship airwake data as discussed above, and to improve analysis efficiency, it is desirable to automate analysis of ship airwake data

collected using an instrumented RC helicopter. This section will discuss theoretical development and recent advances in automated data analysis of off ship airwake data.

Since the direction of rotation due to the airwake is generally random and not predictable, it can be inferred that only the magnitude of the IMU vibrations determines the intensity of the airwake. Therefore, when the airwake pattern only is of interest, it is advantageous to use the radial component of the gyroscope data rather than the three Cartesian components as it decreases the computational burden during analysis. In the automated system, the gyroscope data is converted to spherical coordinates system and the absolute magnitude (radial component) is used to automatically detect airwake peaks.

If { p, q, r } are the angular velocity components of the helicopter in the helicopter's frame of reference system, then the radial component of the angular velocity (ω_r) was obtained as the Euclidian norm of the angular velocity vector $[p, q, r]^T$. Furthermore, local standard deviation of the radial component of the angular velocity (ω_s) was calculated using non-linear local standard deviation filter. Then, as described in the previous section, the 'Airwake equivalent' of the helicopter dynamics (A_ω) was obtained from the product of ω_r and ω_s. Therefore, whenever the helicopter enters into an airwake zone, an increase in the gyroscope fluctuation readings is expected.

This fluctuation will appear as a peak in the gyroscope absolute magnitude (radial) component as well as a peak in the local standard deviation of the gyroscope radial component. Figure 2.4 shows the data related to various steps of IMU data processing. In the upper plot, the green colored data is the magnitude of the raw gyroscope data in spherical coordinates, which is very noisy due to the presence of the helicopter's vibrations. The blue colored waveform is the low pass filtered output of the raw gyroscope data and

the red colored waveform shows the local standard deviation of the raw gyroscope data. The lower plot shows airwake data resulting from the product of the low pass filtered data and local standard deviation of the gyroscope output.

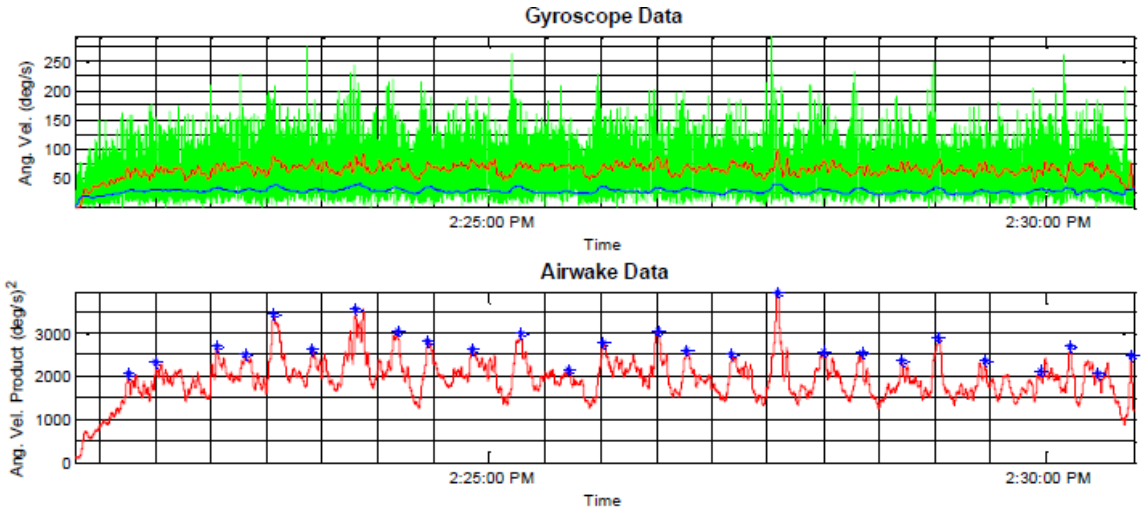

Figure 2.4: Sample processing of IMU data. Upper figure is raw data (green) plus low pass filtered data (blue) and local standard deviation (red). Lower figure shows processed data.

Since simultaneous occurrence of the peaks in both absolute angular velocity and standard deviation of the absolute angular velocity is a characteristic of airwake interaction, A_ω was used to detect local maxima/peaks for the localization of airwake instances. The local maxima peak points that were retained were only those which were at least 15 sec apart and were at least 1.5 times higher than the standard deviation (of the whole waveform data) of the points in the neighborhood of the 10 sec window. The value of the neighborhood window size and the adaptive threshold are experimentally determined such that these values work well for a wide range of flight experiments.

The location of the peaks can be related to airwake interactions. The peaks in (hypothesized) airwake data A_ω were also compared with airwake peaks detected by visual inspection of the helicopter flight video recordings. There was a good correlation in the

occurrence of peaks detected by the two methods. Figure 2.5 shows (hypothesized) airwake data A_ω plotted on the GPS trajectory as a color plot with the color indicating airwake intensity for a headwind β = 0° condition. The local peak location in the hypothesized airwake data A_ω are represented by blue circles.

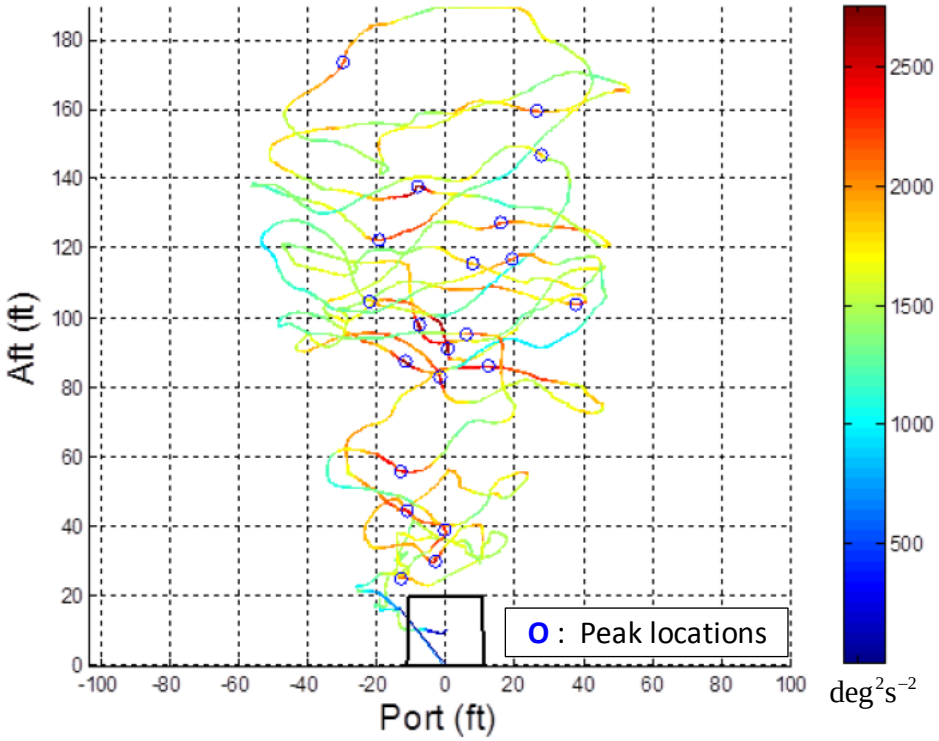

Figure 2.5: Hypothesized airwake data A_ω for β = 0° plotted over helicopter relative position with identified local peaks.

2.1.3 Pilot Input Compensation

The study presented in the previous section demonstrated applicability of RC helicopter in capturing effects of ship airwake in the helicopter dynamics, but it ignored the motion induced by the pilot's inputs to the helicopter. To measure the airwake induced vibrational intensity, it is important to remove the contribution of pilot induced dynamic inputs from the IMU readings.

Since the angular velocity is a vector quantity, the measurement from the IMU can be assumed to be a vector sum of the external disturbances and internal dynamics. If the IMU readings caused by pilot inputs alone can be estimated, the external disturbances (airwake) can be measured by subtracting the estimated readings from the actual readings. This study explores the use of a Back Propagation Neural Networks (BPNN) (trained on a highly diverse pilot input dataset), in predicting the component of IMU readings arising from pilot inputs alone. To accomplish this, a pilot input receiver module was added to the system (used for previous study) to acquire RC signals transmitted by the pilot radio to the helicopter. Figure 2.6 sows the experimental setup used for this study.

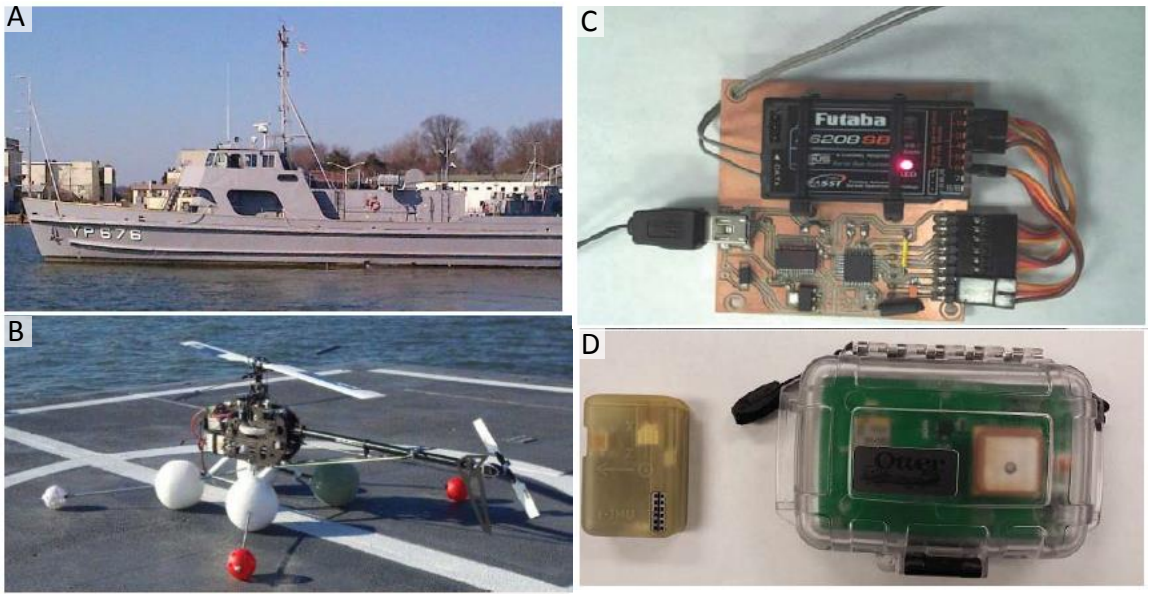

Figure 2.6: Experimental Setup: (A) YP676 training vessel (Top); (B) Instrumented RC Helicopter on Deck; (C) Pilot Input Receiver; (D) IMU and GPS sensor (Bottom).

2.1.4 Back Propagation Neural Network Architecture

Artificial neural network (ANN) [32]–[34] is usually defined as a network composed of a large number of processing units (neurons) that are massively inter connected, operate in parallel and learn from experience (training samples). ANNs are widely used as a pattern

recognition tool especially for nonlinear regression problems. BPNN is a multilayer feed-forward network based on error back propagation algorithm [34], [35].

2.1.4.1 Network Training

The proposed system approximates the pilot input data points (within a fixed time window) to a line and then uses the line parameters to describe the pilot input history. For each pilot input channel (total of five), a history window of 15 samples (equivalent to 0.5 s of data) was modeled with a line equation $y = mx + c$. Here y is the concerned pilot input channel sample, m is the slope, x is the sample index (equivalent to time) and c is the offset in this linear model. If N is the number of samples in the history window (N=15 in our case) then the parameters m and c are calculated using the least square method as follows:

$$m = \frac{N\sum_{i=1}^{N} x_i y_i - \sum_{i=1}^{N} x_i \sum_{i=1}^{N} y_i}{N\sum_{i=1}^{N} x_i^2 - \left(\sum_{i=1}^{N} x_i\right)^2}; \quad c = \frac{\sum_{i=1}^{N} x_i^2 \sum_{i=1}^{N} y_i - \sum_{i=1}^{N} x_i \sum_{i=1}^{N} x_i y_i}{N\sum_{i=1}^{N} x_i^2 - \left(\sum_{i=1}^{N} x_i\right)^2}. \qquad (2.1)$$

Since the pilot data is not a perfect fit to the linear model it is required to consider curve-fitting error while linearizing the pilot data. The proposed system uses sum of the absolute errors (e) as the third parameter for modeling pilot input data, which is calculated as follows:

$$e = \sum_{i=1}^{N} \left| y_i - (mx_i + c) \right| \qquad (2.2)$$

Three parameters $\{m, c, e\}$ were obtained from each pilot input data channel. Five data channels resulted in 15 parameters to represent pilot input data signals. In the proposed method, four channels of gyroscope data were used by BPNN. First three channels were Cartesian components of low pass filtered gyroscope data. The fourth predicted channel was the local standard deviation of the magnitude (in spherical coordinate system) of the

Gyroscope data in a fixed sized window. Therefore, the Neural Network took a 15-dimensional input vector (i.e. pilot data) to predict a 4-dimensional output vector {p, q, r, ω_s} (i.e. gyroscope data). The input and output layer had fixed number of nodes, i.e. 15 and 4 respectively because these are determined by the dimensionality of the input and the output data. The network topology for the hidden layers was selected using 'trial and error' method. It was found that the topology with 12 and 8 nodes respectively in the two hidden layers give the best prediction accuracy. A 10-fold cross validation [36] was implemented to prevent overtraining of the network.

2.1.4.2 Network Performance

Training the network consisted of collecting flight data from experiments conducted in the Rotor testing Lab at the US Naval Academy. The Rotor Lab provided an airwake natural wind free zone for data collection. A variety of Data was collected from five flights conducted on three different helicopters (two Pro and one ESP T-REX 600 models). Out of the three total flights conducted with the ESP model, two were used for training the neural network, which provided approximately a total of 37,000 data samples. To collect a highly diverse training dataset for modeling the helicopter dynamics in full range of operating conditions, a variety of maneuvers were conducted from hovering to oscillations/heaving with varying frequencies. One fourth of the total data was used for actually training the network. The accuracy of the network was assessed by testing it on a complete data set. The histogram chart in Fig. 2.7 plots the error in predicting IMU gyroscope data which indicates that the most probable error is ±2˚/s. which is believed to be a good result given the noise produced by the flying RC helicopter.

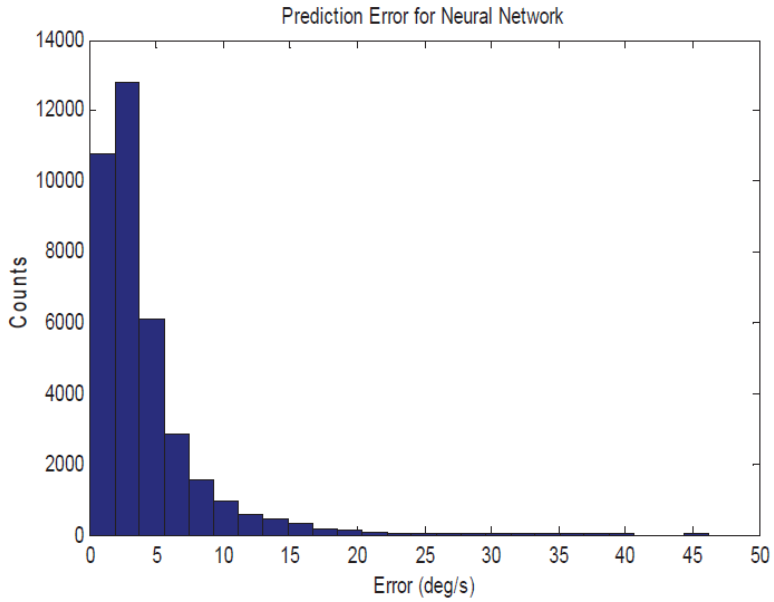

Figure 2.7: Histogram for prediction error of the neural network [11].

Fig. 2.8 shows prediction results of the neural network along with actual measurements. Ideally, there should be a perfect overlap between the actual measurement (in blue) and the predicted data (in red). In this case the predicted X and Y components of the gyroscope do not overlap very well with the actual measurements. This is because of the limited ability to vary the X and Y components of the gyroscope data as compared to the Z component due to limited space in the Rotor Lab and the need to ensure helicopter safety. Therefore, the neural network preformed much better in predicting the Z component and the standard deviation of the gyroscope. The overall overlap between the predicted data and actual measurement proves the capabilities of this system to predict the gyroscope data from the pilot inputs with fairly good accuracy.

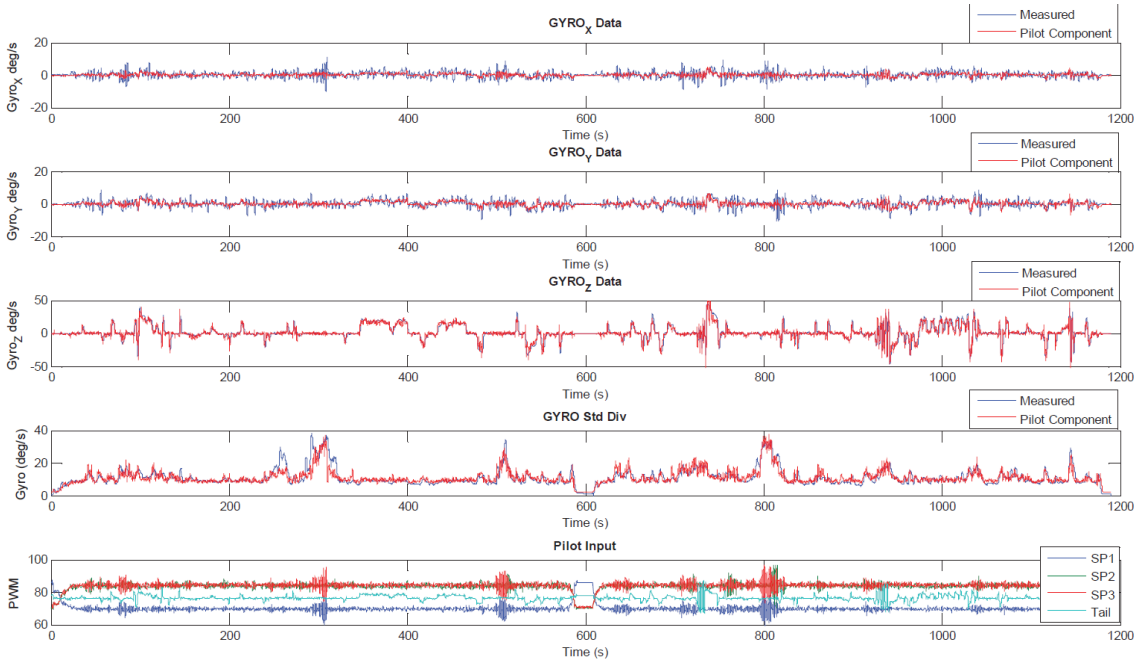

Figure 2.8: Predicted gyroscope data overlaid on actual measurements [11]. A good overlap between predicted and measured angular rate is observed.

2.1.5 Airwake Measurement

High rotor speeds introduce noise in IMU readings in the form in internal oscillations. Since the frequency of such oscillations is much higher than that caused by airwake, effect of the helicopter's own vibrations in the gyroscope output can be nullified by applying a Gaussian low pass filter G (2.3). Through empirical optimization, it was found that a Gaussian filter of length (t_L) 1.0 s and standard deviation (t_σ) of 0.6 s worked well over the wide range of data acquired.

$$G(x) = \frac{1}{\sqrt{2\pi\sigma^2}} e^{-\frac{x^2}{2\sigma^2}};\ \sigma = N_s t_\sigma,\ x \in \boldsymbol{I},\ x \in \left[-N_s t_L, N_s t_L\right],\ t_\sigma < t_L \tag{2.3}$$

where, N_s represents the sampling rate of the data. Similar to the previous study, magnitudes of the angular velocity vector and standard deviation were used to quantize ship airwake (A_ω). However, in this approach, the induced components (predicted using

the neural networks) were subtracted from the measured quantities to characterize airwake data. The airwake data (A_ω) was computed as follows:

$$A_\omega = \left(\omega_s - \omega_s'\right)\left\|\boldsymbol{\omega} - \boldsymbol{\omega}'\right\| \text{ where, } \boldsymbol{\omega} = \begin{bmatrix} p & q & r \end{bmatrix}^T \text{ and } \boldsymbol{\omega}' = \begin{bmatrix} p' & q' & r' \end{bmatrix}^T \quad (2.4)$$

where, the quantities {p, q, r, ω_s} are the angular rates measurements taken from the IMU whereas {p', q', r', ω_s'} are the counterpart quantities estimated using the pilots inputs from the neural network.

Since the ship airwake magnitude (A_ω) is also a function of the position relative to the superstructure of the vessel, the airwake data should be associated with helicopter relative position in reference to the training vessel. The relative position of instrumented helicopter was estimated by subtracting the ship's geographic coordinates from helicopter's geographic coordinates. The relative trajectory of the helicopter was then rotated by the heading angle of the boat to project the trajectory in boat's frame of reference.

In order to test the capabilities of the proposed system, a number of test flights have been conducted in Chesapeake Bay to measure the airwake produced by YP 676 boat for relative wind angles of 0° and 15° (as measured from the bow the ship in the clockwise direction). For each test flight, the Airwake data was generated and overlaid on the helicopter trajectory in the form of a color plot.

Fig. 2.9 show airwake distribution estimated from the proposed system for relative wind from 0° and 15° respectively. In naval terminology *Aft* and *Port* represent the direction towards the rear and the left side of the ship, respectively. In these distribution plots, the color on the helicopter trajectory represents the airwake magnitude in the form of vibrations sustained by the helicopter. In accordance with the CFD results [3], [19], [27],

the high airwake zone is concentrated along the center line for β = 0°, and tilted to the right in case of β = 15°.

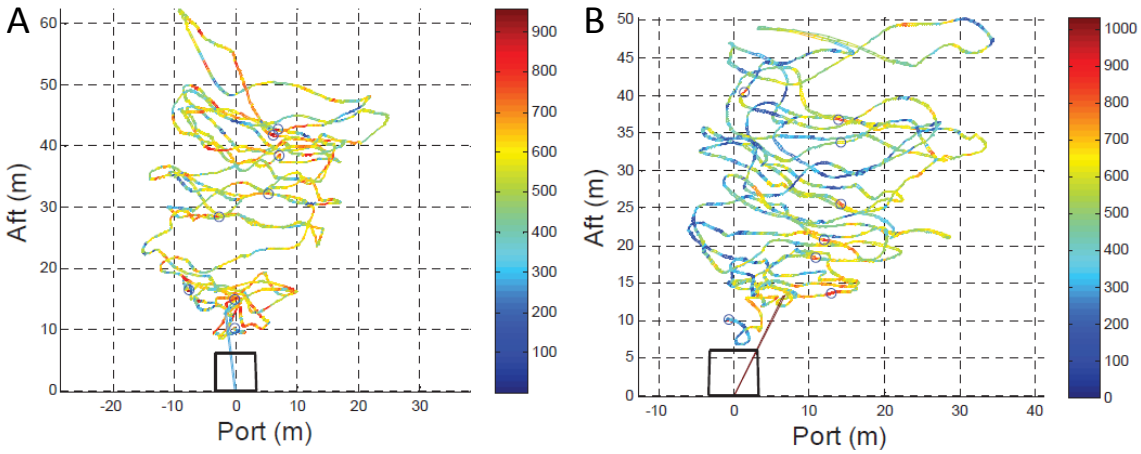

Figure 2.9: Ship airwake distribution for test flights with: (A) β = 0°; (B) β = 15° [11].

2.2 Wireless Telemetry Approach

In the previous approaches, data loggers were used for obtaining helicopter data and pilot inputs. As the helicopter position, dynamics (Gyroscope data) and pilot inputs were recorded on three different hardware platforms; data synchronization was always a concern in the analysis; especially in case of IMU data logger, where the clock synchronization was accurate only to a second. Therefore, any mismatch in the clock time could result in incorrect airwake estimates. A novel unified wireless telemetry system was developed to overcome this limitation and exercise better control over data sampling/acquisition for real-time processing.

Airwake is a form of wind turbulence originating from pressure gradients that result in extreme wind gusts. The motivation of the Wireless Telemetry System (WTS) comes from observing an RC helicopter flying through active airwake zones. During the flight, it

experiences differential airflow velocities that cause tilting of the aircraft since the center of mass, and effective geometric center does not coincide. We can infer that monitoring angular velocity patterns of a helicopter will provide a good description of airwake patterns. Thus, the proposed system detects airwake patterns in wide open areas by monitoring the angular rates of the test RC helicopter using a Gyroscope. Figure 1 shows the tilting of an RC helicopter with angular velocity ω as a result of differential wind velocity (*V1>V2*).

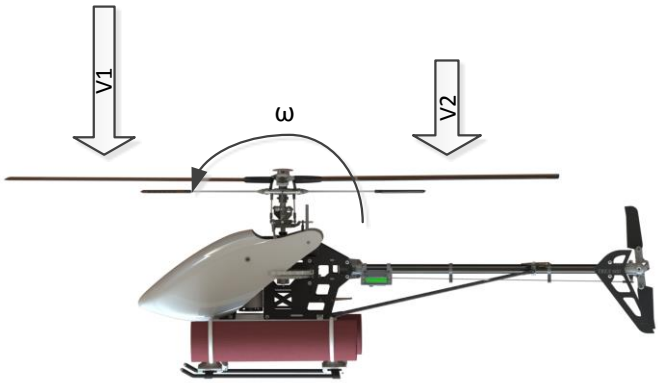

Figure 2.10: Interaction of airwake with helicopter resulting in tilting [30]

It is important to note that the presence of airwake is not the only cause of angular velocity changes of a helicopter during flight. Cyclic pilot inputs change the pitch angles of the rotor blade and result in differential thrust and consequently force moment on the helicopter fuselage. Thus, if this angular acceleration due to pilot inputs is known and the data sampling rate remains constant, the angular rate due to pilot input at any point of time can be estimated from the previous angular rate measurement. In general, the helicopter is as a non-linear 'multiple inputs and multiple output' system which can be modeled as follows:

$$\boldsymbol{x}(t) = f\left(\boldsymbol{x}(t-1), \boldsymbol{u}\right) \tag{2.5}$$

where $\boldsymbol{x}(t)$ represents the system state variables like angular and linear positions/velocities at any time t and $\boldsymbol{u}$ represents the history of external inputs to the system. These external inputs constitute both pilot inputs and ship airwake disturbances. Angular rates of the RC helicopters measured at any time from the Gyroscope mainly depends on parameters previous state variables [31], [37] (like linear velocities, angular rates, rotor speed and altitude etc.) and external inputs as shown in (1). During airwake measurements, if flight parameters like rotor speed, altitude and linear velocities are not drastically changed, then it is safe assumed that the angular rates are mainly depend on to pilot inputs, ship airwake and previous measurements of angular rates. The major components of tilting and oscillations are caused by pilot input responses. The proposed system utilizes machine-learning techniques to estimate and compensate for dynamics arising from pilot inputs in order to isolate airwake induced effects on the aircraft.

The proposed WTS in this study, is composed of three components viz. transmitter module, receiver module and transmitter carrier (RC Helicopter). Both the transmitter module and the receiver module are similar custom-made instrumentation boards mounted with sensors such as IMU, GPS, Thermometer, and Barometer sensors. The transmitter module measures the dynamics of the helicopter and sends the data to the receiver module over Xbee™ long range RF transceiver. The receiver module measures the dynamics of the boat and sends the measured data along with the transmitter module's data to a computer via a USB channel for real time processing. The RC helicopter was selected to carry the transmitter because of its low cost, high maneuverability and hovering capabilities.

The WTS was used to detect ship airwake turbulence in the aft of a cruising US Naval Academy's YP676 for estimation of safe launch and recovery envelopes. The data measured by the transmitting module on helicopter was routed wirelessly to the receiver module connected to a laptop located on the ship and displayed on a GUI. During data collection, the YP craft master maintained consistent speed and wind conditions based on the reference anemometer while the pilot swept the RC helicopter back and forth behind the ship. An experienced pilot maneuvered the RC helicopter (with the transmitting module) in a wave-like pattern at constant height in the aft of the boat. During helicopter maneuvers, the responded to wind gusts in order to keep the helicopter stable. Such responses introduce tilting/vibrations in the IMU data and are highly subjective in nature.

In order to accurately measure actual airwake interactions, pilot induced dynamic inputs must be removed from the IMU data. RC helicopters require five dimensional pilot input in the form of PWM signals. Three control swash plate kinematics and the remaining two control the tail rotor pitch and rotor speed. All five pilot input channels contribute to the helicopter's attitude. Since angular velocity measurements are a vector sum of external disturbances and pilot induced dynamics, external airwake disturbances can be obtained by subtracting the predicted IMU readings from the actual readings. Pilot input from the radio transmitter (Remote Controller) controls the helicopter's attitude and is sent in 'one-to-all' broadcasting mode. Thus, multiple RF receivers can receive the same signal from a single transmitter. Therefore, an additional RC receiver was used in the receiver module to read the pilot inputs sent by the transmitter. WTS uses Back Propagation Neural Networks (BPNN) to find the mapping of IMU reading with pilot input signals. The airwake intensity

was estimated by subtracting the BPNN generated IMU readings from the actual IMU readings in real-time.

The real-time location of the helicopter was estimated in the boat's frame of reference using GPSs in the receiver and the transmitter modules and a real-time trajectory of helicopter was obtained. The helicopter trajectory, IMU vibrational components, and pilot inputs are displayed and recorded in real time through GUI software developed using NI LabVIEW™. By fusing sensor data, possible locations of sharp gradients in the air velocities can be mapped relative to the ship representing helicopter/airwake interaction patterns (accurate within one rotor diameter of the helicopter). Figure 2.11 shows the architecture of WTS proposed to measure ship airwake patterns.

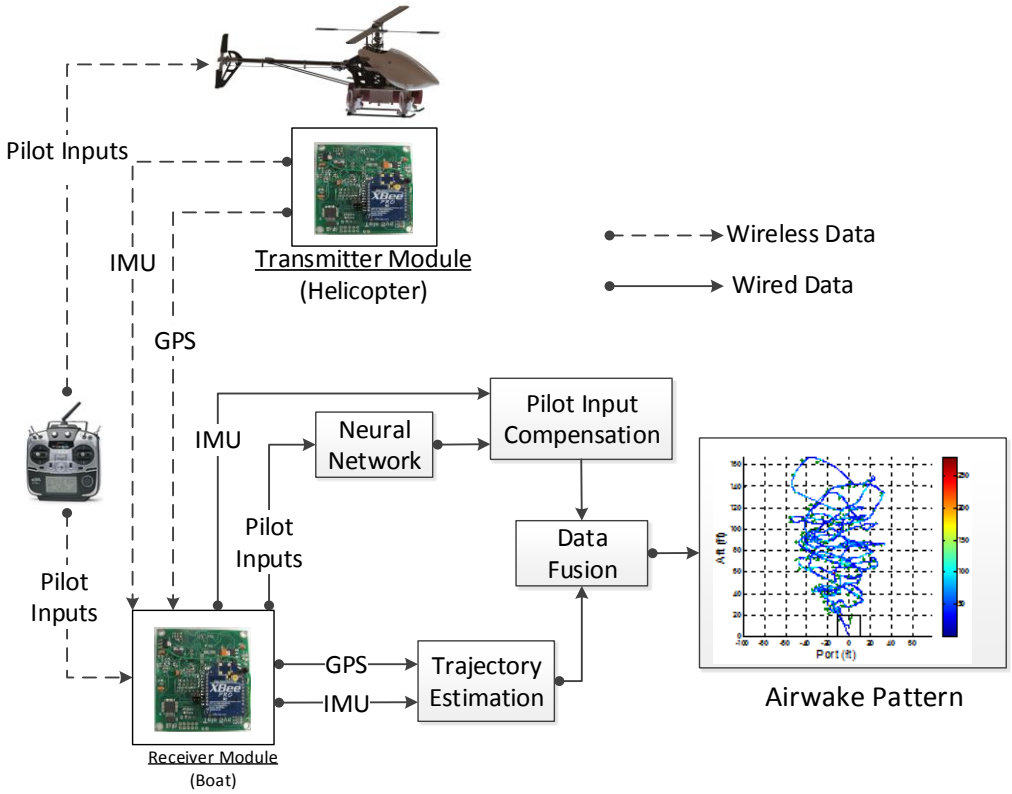

Figure 2.11: Schematics of the wireless telemetry system [30].

2.2.1 System Implementation

The WTS used three different off-the-shelf RC helicopters with rotor diameter of 1.3 m (4.5 ft) to detect airwake patterns generated by the YP676 vessel. The YP676 vessel was equipped with an eight channel ultrasonic anemometer array for maintaining a consistent wind condition during flight tests. Both transmitter and receiver modules are battery powered, independent sensor boards based on ATmega128 and ATmega8 microcontrollers. To ensure interchangeability, both sensor modules were deliberately designed to be similar both in terms of hardware and software. Each of the sensor modules contains GPS, 6 axes IMU, thermometer, 3D magnetometer, and barometer sensors. The sensor boards are equipped with micro SD card data logger, Quad USB to UART IC chip, micro USB interface, XBee RF module, and Futaba™ 8 channel 2.4GHz RC receiver interface. The task of the transmitter module is to read all the sensors, send all the data to the SD card over SPI bus and transmit the same data over XBee wireless link.

The receiver module connected to a computer via USB reads all of the onboard sensors, records the data on an SD card, and sends the same to the computer via one of the four virtual serial COM ports. The XBee link on the receiver module receives data from the transmitter module and directly sends data to the computer over another serial COM port. The microcontroller on the receiver module reads pilot inputs in the form of PWM signals and sends these signals to a computer over a third serial COM port at an update rate of 45 Hz. Therefore, the receiver module, over three serial ports, provides sensor data from the transmitter module and receiver module and pilot input data via USB link.

Since both sensor modules are interchangeable, the mode of operation of the module is selected by a jumper switch. Figure 2.12 shows the connections schematics of the sensor modules of the WTS.

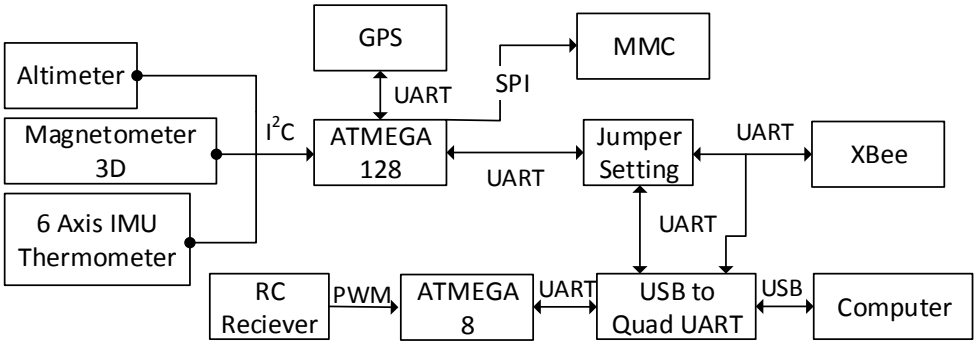

Figure 2.12: Hardware schematics of sensor modules [30]

The transmitter module and the receiver module were both rigidly fitted and oriented on the helicopter and the boat respectively using custom made 3D printed mountings.

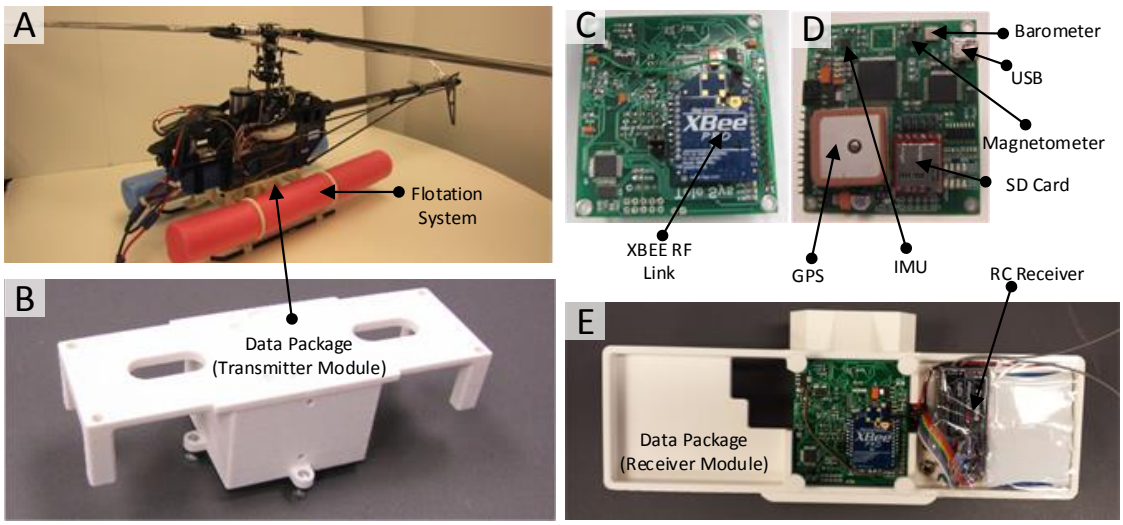

Figure 2.13: Hardware Setup: (A) Helicopter fitted with Data Package and Flotation system; (B) Data package with transmitter module inside; (C) Transmitter module (Top); (D) Transmitter module (Bottom); (E) Receiver module [30].

Rigid mounts were necessary in order to accurately capture angular velocity components of the helicopter while in flight due to the sensors high sensitivity. Figure 2.13 shows the transmitter module fitted on the helicopter and the receiver module fitted on the ship using 3D printed mountings.

2.2.2 Network Training and Pilot Inputs Compensation

Similar to the study presented in section 2.1, this study also used BPNN networks to model helicopter's rotational dynamics from the pilot inputs. However, in the previous study, undertraining in the X and Y axis gyroscope data was observed. To overcome this issue, the following changes were introduced in the neural network schema for this study:

- Recurrent Network approach was applied by feeding the previous state estimates in addition to the pilot inputs to predict current state estimates.
- Instead of training a single network for predicting four angular rate quantities, four separate neural networks were trained to predict the four angular rate channels individually.

RC helicopters, similar to every electro-mechanical system, require time to respond to pilot control inputs. Hence, rather than instantaneous input, there is a need to consider the pilot input history for predicting the IMU output at any instant in time. Due to dimensionality issues, it is not possible to directly use the pilot input history as input vector. To reduce the dimensionality of the training data, pilot input history was approximated (within a fixed time window) to a linear function of time and line parameters were used to describe the pilot input history. For each pilot input channel (total of five), a history window of 43 samples (equivalent to 0.944s of data, one cycle of cut-off frequency) were

used and modeled with a line equation $y = mx+c$. Similar to section 2.2.1, 15 parameter were used to describe the input history and the sets of $\{m,c,e\}$ were computed using equation (2.1) and (2.2) for each of the five input channels. In addition to this, additional 3 channels of the previous angular rates were also fed into the network bringing the input dimensionality of the networks to 18.

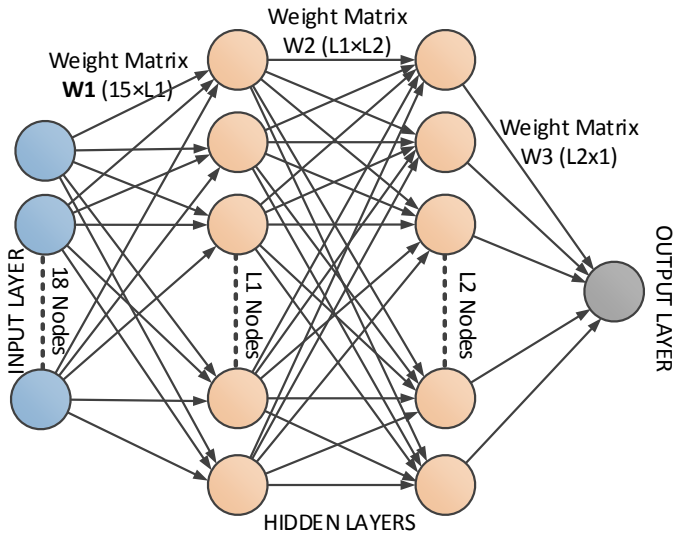

Figure 2.14: Topology of Neural Networks used in WTS [30].

Fig. 2.14 shows the general topology of the neural network used in the system. The size of the input and the output layer as determined by the dimensionality of input and output data that was 18 and 1 node respectively. The network topology for the hidden layers was selected using 'trial and error' method. The number of nodes was varied from 5 to 14 for the first hidden layer and from 2 to 8 for the second hidden layer and the topology giving the highest prediction accuracy was selected.

Back-Propagation Neural Network training involves assigning initial weights randomly; thus, it is possible that the training accuracy obtained from a particular topology is not the 'best' set of chosen parameters. This is due to the fact that the BPNN training

process is analogous to gradient descent algorithm and is susceptible to local minima in the weight-error space while obtaining optimum weights. To overcome this limitation, we trained the network 30 times for each topology and considered the 'overall best network' for the IMU prediction in the 'trial and error' procedure. To further introduce regularization in the presented study, the proposed networks were trained on data collected for three different RC Helicopters (of similar sizes). The three helicopters used in this study have been referred to as 'Heli 1' (Align™ T-TRex600E PRO, without fuselage cover), 'Heli 2' (Align™ T-TRex600E ESP, without fuselage cover) and 'Heli 3' (Align™ T-TRex600E PRO, with fuselage cover). Table 2.1 shows the network topologies finally selected for the twelve BPNNs. 10% the total data was used for training and a 10-fold cross validation [35], [36]was applied to prevent overtraining of the network.

Table 2.1: BPNN Network Topologies

	Neural Network							
	NET1		NET2		NET3		NET4	
	L1	L2	L1	L2	L1	L2	L1	L2
Heli 1	7	6	7	4	8	4	10	4
Heli 2	7	4	8	6	7	4	11	4
Heli 3	7	3	7	5	9	3	11	3

After obtaining the optimum sets of neutral networks for the three helicopters, the neural network sets were tested on the remaining 90% data. Figure 2.15 shows five performance subplots of the four neural networks in the estimation of the four Gyroscope data channels along with pilot inputs for 'Heli 1'. In these subplots, the red colored plots show data obtained from the sensor measurements whereas the blue plots show the

predictions from BPNN using pilot inputs.

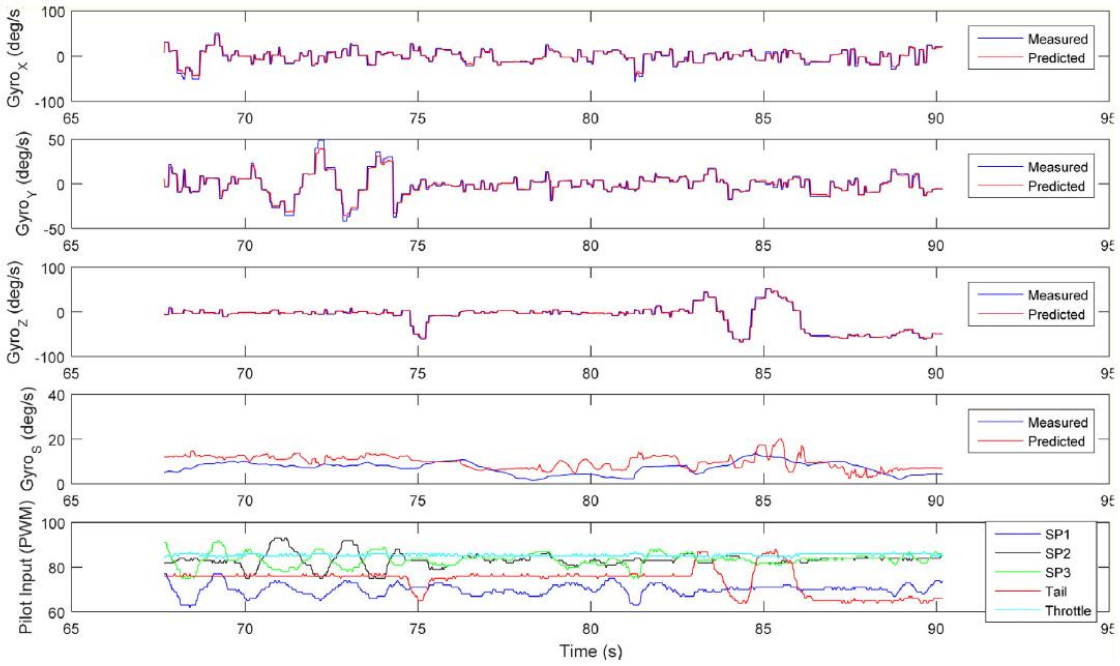

Figure 2.15: Prediction by neural networks corresponding to Heli 1 (showing 25 seconds of data) [30].

For quantitative analysis of predicting results, histograms were plotted in Fig. 2.16 showing the prediction error distribution of the neural networks trained for all the three helicopters. In addition to this, RMS prediction error for the neural networks is also shown in Table 2.2. The RMS values of the prediction errors varied between 2 and 7 deg/s, which is reasonably good for a noisy platform like RC helicopter.

Table 2.2: BPNN Prediction RMS Error (deg/s)

	Neural Network			
	NET1	NET2	NET3	NET4
Heli 1	8.28	5.93	5.10	3.44
Heli 2	3.84	6.81	2.93	2.13
Heli 3	7.61	17.16	5.62	3.55

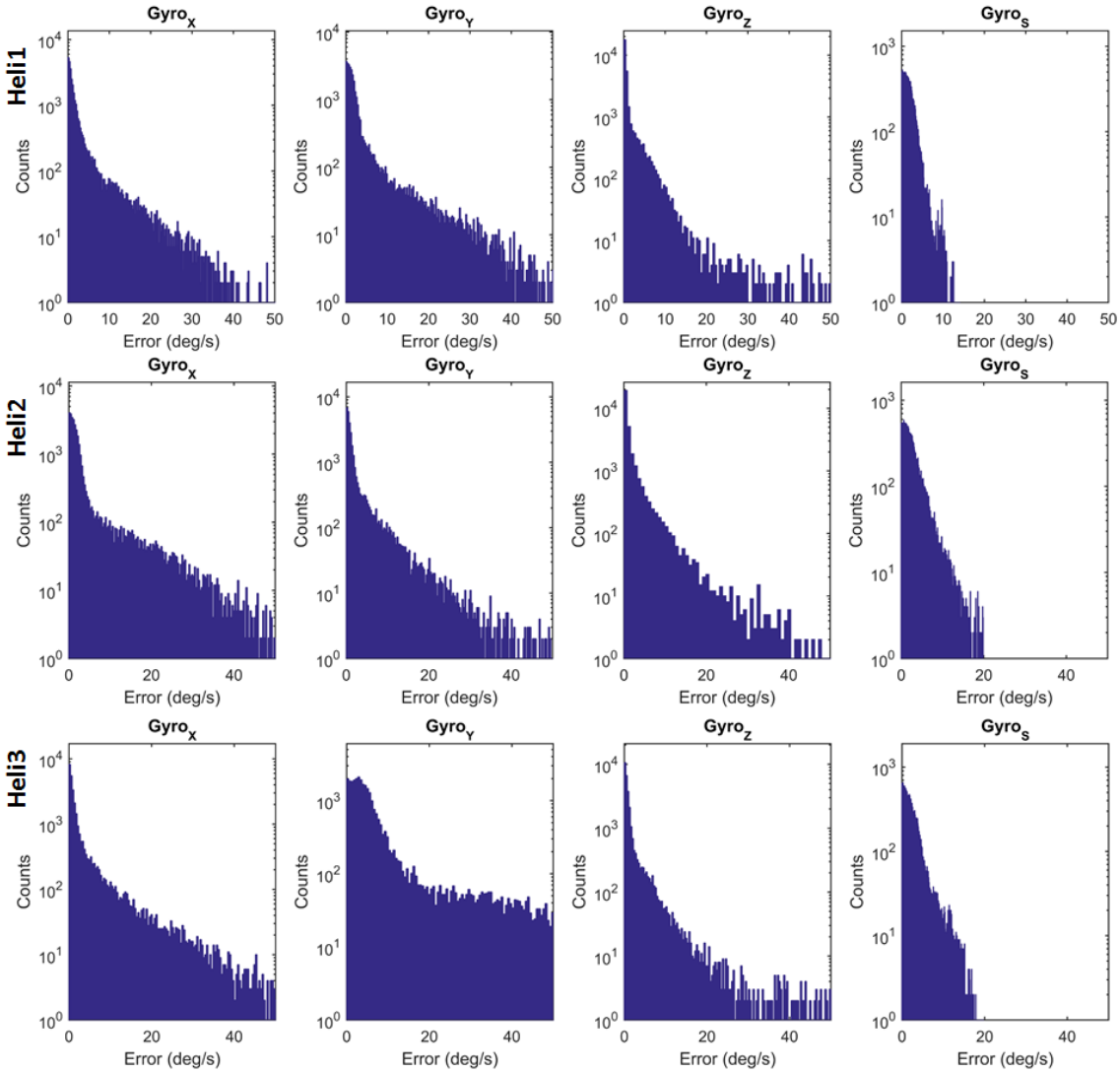

Figure 2.16: Error distributions for the prediction by the neural networks corresponding to the three helicopters [30].

2.2.3 Airwake Distribution

Similar to the pervious approach, airwake intensity was computed from the neural network residuals as shown in eqn. 2.4. To test the system's performance in an actual airwake measurement, multiple flight operations were conducted in the Chesapeake Bay, MD over a period of one year. The test flights were conducted at a constant height and heading direction of the helicopter. The wind conditions were maintained well within the

specified limits (± 1knots and ± 5˚ heading). Airwake status intensity along with the helicopter location (transmitter carrier) was presented and recorded in real-time through GUI software developed in National Instruments LabVIEW™. Fig 2.17 shows the GUI developed to interface with the hardware and for processing the data in real-time.

For the final estimation of airwake pattern, the airwake data as obtained through Eqn. (2.4) is overlaid on the trajectory of the helicopter in the form of spatial distribution plots. In these plots, the color on the helicopter trajectory represents the airwake magnitude after pilot input compensation.

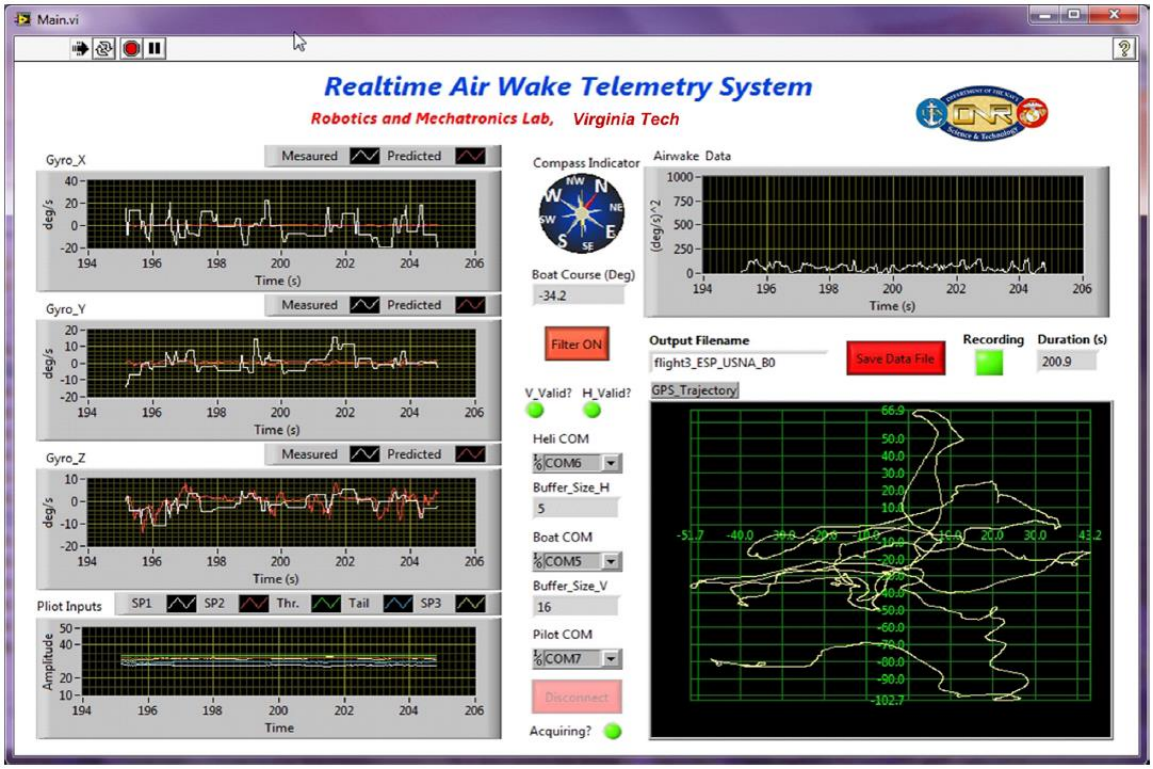

Figure 2.17: GUI for proposed wireless telemetry system [30].

Fig. 2.18 shows sample ship airwake pattern obtained in a test flight of relative wind angle (beta angle) 0° and 15°. A black dotted curve shows the region of high airwake with respect to the flight deck. A high perturbation is detected along the outer regions of the

trajectory as the WTS measured differential wind velocities. This is in accordance with the wind conditions and related numerical simulations as it is symmetric about the centerline of the helicopter trajectory. In this figure, the high airwake region as marked by the dotted curve is tilted towards the right relative to the stern of the ship, which again correlates this result with numerical simulations.

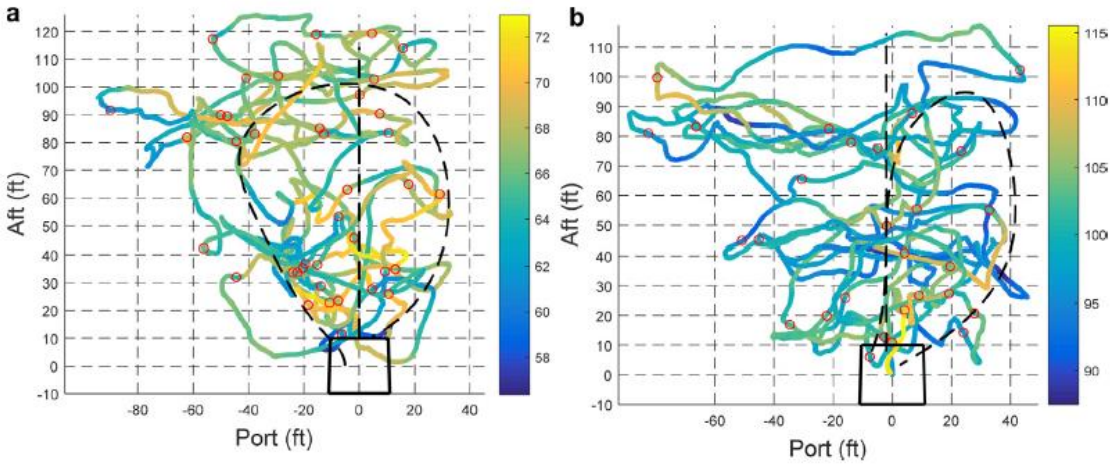

Figure 2.18: Ship airwake distribution (with airwake zones marked using black dashed lines) for: (a) test flight with beta angle of 0 °, (b) test flight with beta angle of 15° with skewness observed towards right [30].

2.3 Other Machine Learning Approaches:

Whereas, the previous study used only Back Propagation Neural Networks (BPNN) to model the helicopter's response to pilot inputs, to confirm the superiority of BPNNs in modeling helicopter dynamics, the performance of BPNNs was compared against other machine learning algorithms. This study presents three different machine learning technique:

1) BPNN,

2) Bayesian Mixture of Experts (BME), and

3) Adaptive Neuro-Fuzzy Inference System (ANFIS).

The three Machine Learning (ML) algorithms were selected for modelling the system since they represent the simplest of the three basic categories in ML algorithm. BPNNs use error minimization and represent algorithms using gradient descent methods for to fit complex non-linear models on data. BMEs use simpler models (linear experts) to model complex data pattern and probabilistically mix them using expectation maximization. Thus, BMEs represent a class of Bayesian learning algorithms. ANFIS networks are fuzzy inference systems which use gradient-descent-type algorithms to tune fuzzy membership functions. As a result, ASFIS networks possess capabilities of both BPNNs (as they use error minimization for parameter optimization) and BMEs (as they use simple models during defuzzification process). As these ML algorithms are the simplest of their kind, prediction results from these algorithms will be similar to other complex algorithms of these kinds.

Also, the telemetry system was upgraded with an aviation grade INS/IMU sensor to include helicopter attitude measurement in modeling the helicopter dynamics using machine learning algorithms. The system was tested on data collected in a wide range of wind conditions generated by modified YP676 naval training vessel in Chesapeake Bay area over a period of more than a year.

2.3.1 System Architecture

The proposed system consists of two independent instrumentation sub-systems called rover module and base module [28], [31]. These modules communicate with each other via a long range Wi-Fi network with an update rate of up to 150 Hz. The Wi-Fi router utilizes two types of antennas, one Omni-directional short-range rod antenna and another long

range direction Yagi antenna. Figure 2.19 shows hardware setup for the presented telemetry system.

To estimate ship airwake patterns, an RC helicopter retrofitted with the rover module was flown in the target areas. The rover module then sent the helicopter's dynamics data to the base module over Wi-Fi. A computer connected to the base module recorded and processed the data and displayed appropriate results/flight parameters on screen in the form of graphs and trajectories. More details on this hardware configuration are provided in Chapter 4 of this dissertation.

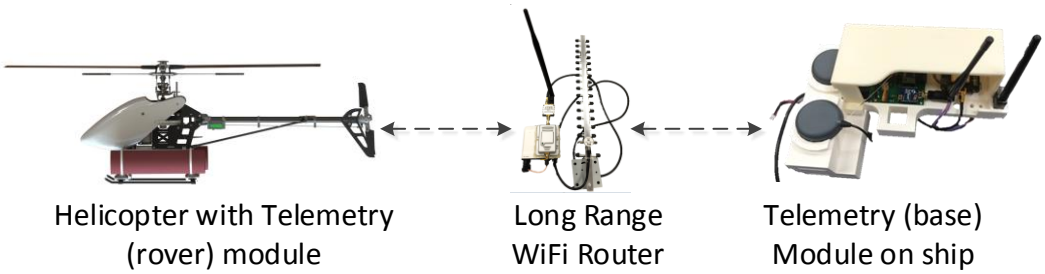

Figure 2.19: Telemetry System hardware setup[28]

During measurement, the proposed telemetry system is mounted on T-REX 600E PRO RC helicopter and flown in the lee (downwind) of the superstructure of the YP676 craft in a sweeping trajectory. The data received on the base computer processes and records the data in real-time. The relative position of the helicopter in the boat's frame of reference is obtained from position and heading estimates from the VN200 INS on both modules. During post processing of the data, the system allows the user to select and use one of three different machine learning algorithms to process the data. The selected algorithm filters away pilot input components from angular rate measurements of helicopter and estimates the airwake impact on the helicopter. The airwake intensity in the form of dynamics of helicopter arising from airwake is then plotted on helicopter trajectory relative to the ship.

The YP676 is equipped with anemometer array to help the craft master to maintain constant relative wind conditions. Figure 2.20A shows the telemetry system operating over the flight deck of the modified YP676 craft.

2.3.2 System Modeling

The presented telemetry system uses the helicopter's angular rates measured using a gyroscope to characterize ship airwake. Helicopter motion is primarily controlled with a swash plate mechanism through cyclic control input. During flight, other than the effects of airwake/turbulence, the main forces acting on the helicopter are rotor blade thrust, gravity, gyroscopic forces and air drag [31]. Figure 2.20B shows free body diagram of the helicopter where yellow arrows represent forces, green arrows velocities and blue arrows frame of reference. A forward motion (Fig. 2.20B) experiences a differential thrust (*F1* and *F2*) along the longitudinal axis is applied through cyclic control. This different thrust makes helicopter tilt forward[38].

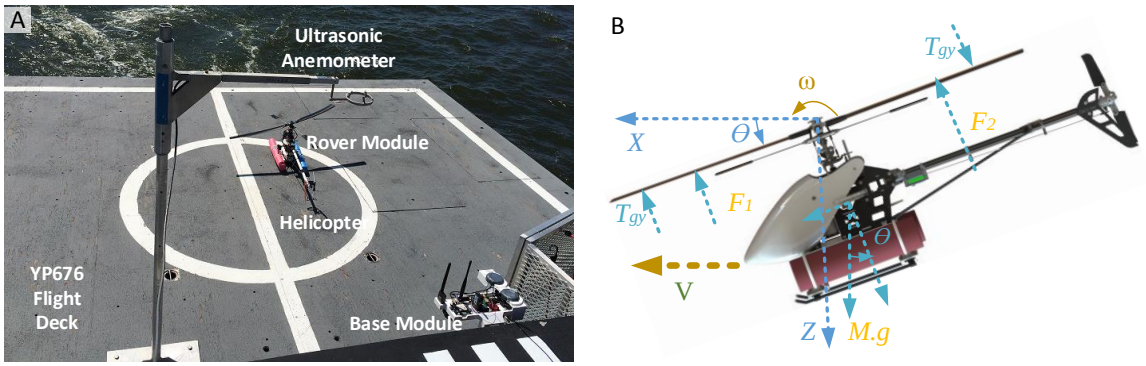

Figure 2.20: (A) Experimental Setup; (B) Free body diagram of helicopter [28].

Any tilting or vibration of the helicopter disturbs the rotating rotor blades and stabilization bar from their plane of rotation and generates a gyroscopic torque (T_{gy})

opposing the rotation of helicopter. While tilting forward, in addition to gyroscopic torque, helicopter experiences a pendulum like counter torque as the point of rotation (rotor hub) is higher than the center of mass of the helicopter. Due to high speed downwash from rotor, motion of helicopter faces significant viscous drag [37]. All these opposing torques make the angular velocity of the helicopter a non-linear function of pilot inputs and attitude. In this work, RC helicopter's non-linear response to pilot inputs has been modeled using three machine learning techniques BPNN, BME and ANFIS networks.

2.3.3 System Training

For training the system, the telemetry system was flown in a large enclosed hangar in Davison Air Field. The hanger provided an airwake free zone to collect the training data for the machine learning algorithms. Four indoor flights were conducted with T-REX 600E Pro helicopter to collect training data. For collection versatile dataset, the pilot was instructed to fly the helicopter in a variety of extreme maneuvers. To avoid ground effect disturbances [39] in the training data, the helicopter was flown at a significant height (at least 2 rotor diameters ~3m) from the floor. During these training flights, a variety of helicopter maneuvers were performed. A versatile dataset of pilot inputs along with helicopter attitude with angular rates was created during these indoor experiments. During these four indoor flights, a dataset of around 75,000 samples was collected. To ensure the prediction generalization of the system, only ~5,000 samples (around 6.25% of the total data) were used for training. The remaining data was used for testing the performance of the system.

For each of the three machine learning algorithms, three networks were trained to individually predict the three Cartesian components of helicopter's angular rates from pilot inputs and attitude information. Thus, each network was trained with a 6-dimensional input vector consisting of the 3 swash plate servo PWM signals, 1 tail rotor PWM signal and 2 attitude (pitch and roll) angles. The output vector was a one dimensional Cartesian component of helicopter's angular rates. To improve the prediction accuracy of the networks, the complete dataset of input and output vectors was normalized to zero mean and unit standard deviation before training.

2.3.3.1 BPNN Training

BPNN is a multilayer feed-forward network and uses error back propagation algorithm for training [32]–[35]. For prediction for pilot input component in helicopter's angular rates, 3 BPNNs each with 2 hidden layers were trained. The number of nodes in input and output layers were selected as 6 and 1 based on the dimensionality of the input and output vectors. The number of neurons in hidden layers were selected by trial and error. The number of neurons in both hidden layers were varied from 3 to 15. As weights of the BPNNs are selected randomly and the network converges at local optima in weight space, each network topology was trained 15 times. The network topology delivering the best prediction accuracy was retained. MATLAB's 'Neural Network Toolbox' was used for error back propagation training with the Levenberg–Marquardt algorithm [40], [41]. The "tansig" and "purelin" were used as activation functions for the hidden layers and the output layer respectively. Ten-fold cross validation method [36] was used to prevent

overtraining of the networks. Table 2.3 shows the final topologies for the three trained BPNNs.

Table 2.3: BPNN Network Topologies

Neural Network	Input Layer	Hidden Layer 1	Hidden layer 2	Output layer
Net1 (X axis)	6	5	5	1
Net2 (Y axis)	6	5	7	1
Net3 (Z axis)	6	4	8	1

2.3.3.2 Training BME

Bayesian Mixture of Experts (BME) is a type of directed graph network in which independent output of multiple subunits (Experts) are probabilistically combined into a single output [42]. Each expert consists of an observed continuous node and a hidden discrete node. The continuous hidden node (or output node) receives information from experts and linearly combines the estimated output value. MATLAB implementation of BME in 'Bayes Net Toolbox' [43] has been used in your system.

Fig. 2.21 shows the topology of the BME model used in the proposed system. As the dimensionality of the input data is 6, 6 experts have been used in this application. Increasing the number of states of the hidden discrete nodes improves the prediction accuracy for the extreme inputs (which are statistically rare), but at same time increases the computational load exponentially. Thus, with a balanced trade- off between accuracy and computational load, each hidden node has been assumed to have 3 states. For a given input to an expert, hidden node estimates the likelihood values of coefficients corresponding to

each state and probability of being in any particular state. The output node probabilistically combines the output of all the experts to give the final output.

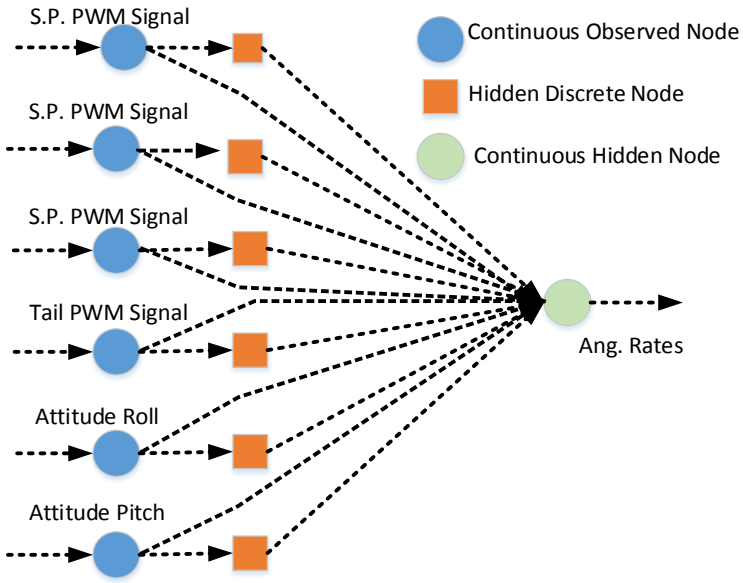

Figure 2.21: Topology of BME used in proposed telemetry system [28].

2.3.3.3 Training ANFIS networks

Adaptive Neuro Fuzzy Inference System (ANFIS) is a type of feed forward network capable of supervised learning [44]. In practice, ANFIS networks are same as Fuzzy Inference Systems (FIS) [45]. Although both BPNN and ANFIS networks have similar topology, there is a significant difference between the two: BPNN optimizes network weights for given activation functions to minimize prediction errors, whereas ANFIS optimizes the shape of fuzzy Membership Functions (MFs) to minimize the prediction errors.

ANFIS networks used in the presented telemetry system use a hybrid learning algorithm [44](a combination of the least-squares and back-propagation gradient-descent

methods) to optimize a Sugeno-type FIS. MATLAB implementation of ANFIS training in 'Fuzzy Logic Toolbox' has been used in the presented system, which cross-validates the models on a checking dataset to prevent overfitting of the training dataset. During the training phase, different types of MF shapes were tried on Sugeno-type FIS structure to be optimized, but 'Gaussian Bell' shaped input MFs and 'Linear' shaped output MFs delivered acceptable prediction results. Because of memory constraints, the number of MFs was limited to 2 although increasing the number could further improve the prediction

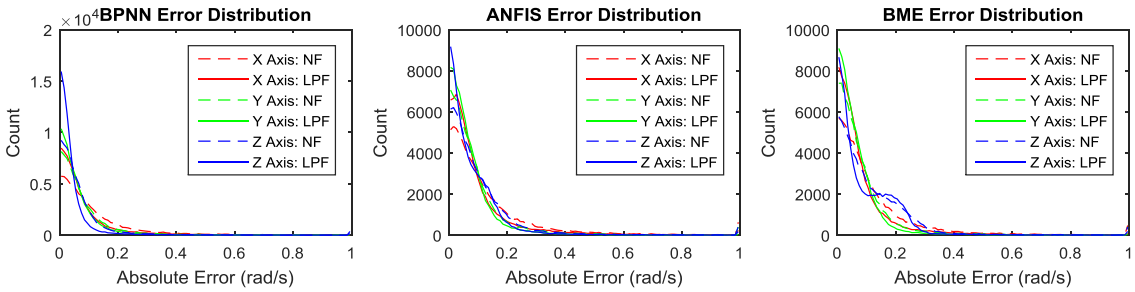

Figure 2.22: Prediction error distribution for all the three algorithms [28].

Three networks for each of the three network types (BPNN, ANFIS and BME) were trained separately to estimate the pilot input component in helicopter dynamics. Figure 2.22 shows histogram plots of absolute prediction error of the three networks while predicting the Cartesian components of helicopter's angular rates. To estimate these error distribution histograms unseen test data from remaining indoor flights (~70K samples). The figure shows 6 histogram plots from the three networks. The plot legend extension 'NF' stands for 'No Filter', and represents prediction error with respect the original data. The plot legend extension 'LPF' stands for 'Low Pass Filter', and represents prediction error with respect the low pass filtered data. The histogram plots in Fig. 2.22 suggest that the BPNN outperforms both BME and ANFIS by delivering the best fit on training data.

BME along with ANFIS, perform similar in modelling the pilot input components in helicopter's noise.

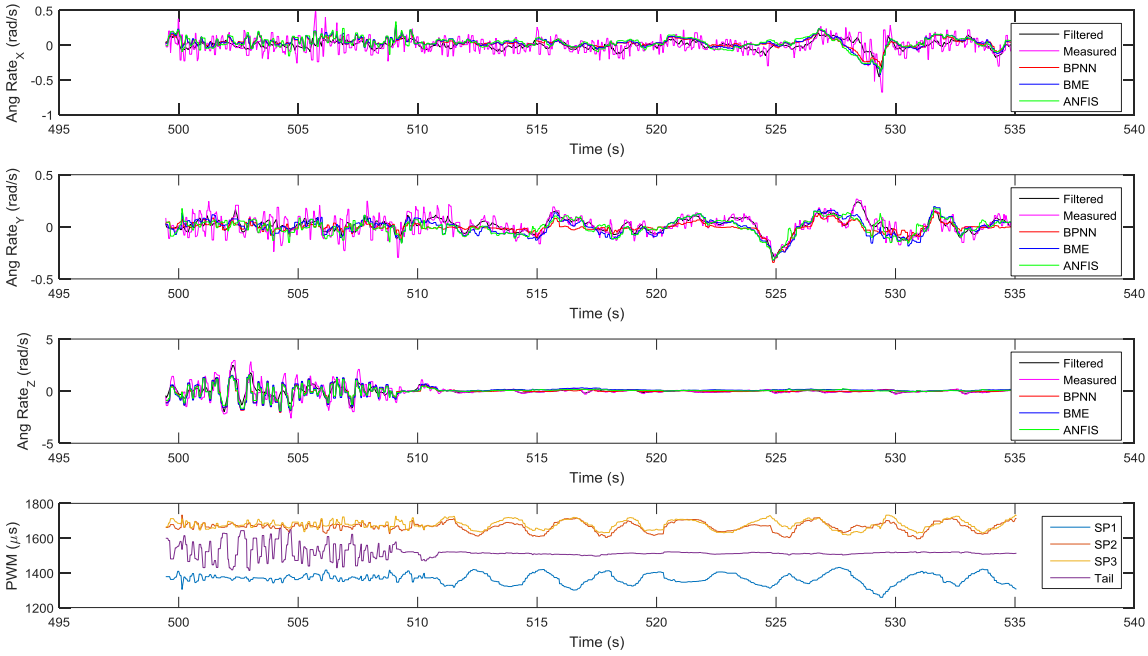

Figure 2.23: Prediction results from all the three machine learning algorithms [28]

Fig. 2.23 shows prediction results of angular rates (in rad/s) from all the three types of networks on a short section (35 s) of a test flight. While assessing the prediction results (Fig. 2.23), it was observed that both BME and ANFIS did not perform well on extreme pilot inputs like BPNN, but its performance exceed BPNN on medium/small pilot inputs and hence provided better generalization. This observation arises from two facts that BPNN uses error minimization during its parameter optimization, and both BME and ANFIS use simpler functions to model the pilot input data. Based on the findings from this study, BPNN was selected as the final machine learning algorithm for modeling helicopter dynamics and airwake analysis.

CHAPTER 3: INDOOR MOTION TRACKING AND WIND MAPPING

The previous chapter presented the use of machine learning algorithms to isolate ship airwake related dynamics by subtracting the pilot generated dynamics from the net measured dynamics of the RC Helicopter. However, for actual validation of the proposed approach, the model output needs be compared against known wind flow field. This chapter discusses of the development a novel indoor wind generation and mapping system to generate 'ground truth' wind data for the calibration the proposed telemetry system. The core of this system is a novel opto-inertial motion tracking device which is also the main focus of this chapter. This proposed motion tracking device has been used to locate both anemometer (for wind measurements) and RC helicopter in a same of reference.

3.1 3D Wind Mapping Methods:

As widely known, helicopter dynamics depend on local wind conditions relative to the helicopter's moving parts (Rotor blades, fuselage, empennage, etc.). Therefore, for the proper calibrations of the proposed telemetry systems, an accurate spatial distribution 3D wind flow field is critical. At the same time, the RC helicopter's motion/position also needs to be known with reliable accuracy. Most importantly, the wind flow field needs to be reliable and reproducible. This requires the calibration to be performed in an enclosed environment where the unpredictable atmospheric wind may be separated. Whereas existing tools like SoDARs, Wind LiDARs, and Doppler radars are more suited for

characterizing atmospheric wind conditions in open spaces, sensing tools like anemometers can be used for indoor wind measurements.

An anemometer can be moved to various locations, and with the help of some positioning system, the wind flow measurements can be combined with position estimates to generate 3D wind maps. The same positioning system can also be used to estimate the wind flow conditions around the helicopter by using the helicopter's position estimates with a pre-generated wind flow map.

3.2 Indoor Positioning Systems Review:

So as not to be limited to airwake estimations/wind mapping, 3D positioning and motion tracking has a vital role in various engineering disciplines involving motion analysis in industry and academia, and a significant area of research is developing low-cost, accurate tracking sensors. Certain engineering applications such as robotics, navigation, biomechanics and virtual reality often require real-time position tracking [46]–[50]. Depending on the application, the position tracking systems are selected based on measurement range, accuracy and update rate. Position tracking systems can be broadly categorized into two types: contact-based and contact-less. This review will limit the discussion to contact-less tracking system only.

Contact-less tracking systems often measure electromagnetic/acoustic modalities without making physical contact for tracking purposes. Based on the type of the modality used, major tracking systems constitute: Magnetic Tracking [51]–[53], Inertial Tracking [54], [55], Radio Signal Strength Indicator (RSSI) Tracking [56], [57] and Optical Tracking. The scope of this dissertation is limited to optical tracking.

Optical trackers work through triangulation and require direct line-of-sight from the camera to the measurement point. They are also capable of larger work envelopes. Optical tracking methods are categorized into two groups: marker-less and marker-based tracking systems.

3.2.1 Marker-less Camera-based Tracking

The simplest marker-less optical tracking is a calibrated monocular camera tracking. If the camera is rigidly mounted normal to the plane of motion, then the pixel coordinates of an object being tracked can be mapped to the actual 2D position in plane. Spatial optical tracking often requires multiple perspectives (like stereovision) of the tracked object. Stereovision requires simultaneous identification and tracking of an object in two (or more) images, which is computationally expensive. Spatial object position is obtained from the disparity in position of the object in planar images [58], [59]. Marker-less visual tracking systems have the potential to provide natural, non-contact methods to measure object position and orientation. Although powerful and accurate, a camera-based tracking system is computationally expensive, leading to a relatively low update rate.

3.2.2 Marker-based Tracking

Marker-based tracking systems [60]–[62] typically consist of surface markers and image sensors (e.g., the Vicon motion systems[63]). Specialized optical filters are often used to isolate markers from the background and significantly reduce computational load. These systems offer higher accuracy and higher update rates compared to the marker-less camera-based tracking systems. Such commercial tracking systems typically cost

thousands of dollars and require time-consuming calibration. Most significantly, these systems require cumbersome setup of multiple cameras which is very difficult to realize because of required absence of any mounting walls around the helicopter flight area.

Time multiplexed tracking systems such as Microsoft Kinect, MEMSEye and Lidar project their own marker patterns and use optical triangulation to obtain 3D location [64]. These sensors are less expensive and can achieve moderate to high update rates but at an expense of accuracy. Low cost tracking systems like Lumitrack [65] project static laser patterns and use the patterns to track relative motion. These sensors are adept at measuring relative velocity between the base frame and moving object with high update rates, but don't provide accurate position estimates. In a similar approach, Bokode [66] projects position information in the form of QR codes embedded on optical bokeh. The position information of 'Bokodes' is then used to estimate the position and orientation of the (SLR) camera receiver with respect to bokodes.

3.3 Proposed Indoor Motion Tracking System

To overcome these limitations, this dissertation present a novel active markers based indoor motion tracking device using linear optical sensor array (LOSA). This LOSA tracking system [67] offers high positional and attitude accuracy at high update rates. The proposed LOSA tracking system tracks an active marker (omnidirectional IR LED cube) at millimeter-level accuracy with very high update rate (~320 Hz). The proposed system combines inertial and optical tracking without relying on magnetometer data, which is susceptible to stray magnetic noise and provides more reliable position and attitude estimates even on high noise platform such as an RC helicopter. Experimental results

demonstrate millimeter-level accuracy in the tracking system's operational range. Furthermore, the system's total cost including components and fabrication is estimated to be low when manufactured in volume. Finally, the system is relatively small, lightweight and low powered, making it suitable for payload sensitive systems such as RC helicopters.

Use of line cameras in computer vision is not new. Researchers have been using linear cameras for computer vision for quite some time [68]–[70]. However this dissertation presents an application of a low cost LOSA in coordination with an IMU to obtain position and attitude estimates in the form a reliable spatial motion tracking device.

3.3.1 Tracking System Implementation

The key components of the presented tracking system are LOSA sensor modules and Active LED marker equipped with a 9-axis IMU and wireless connectivity. The tracking system locates the LED marker by using triangulation on a pinhole camera image of the marker on the photodiode array area (length). The system estimates triangulation disparity by finding the peak value positions of the signals in the sensor array while adjusting for diffraction effects. Thus, each pair of sensor modules facilitates 2D position tracking in the epipolar plane of the sensor pair. Utilizing multiple sensor pairs, the marker's spatial position may be extrapolated from multiple planar measurements. A computer then fuses the position estimates from stereovision and IMU data using EKF to extract more accurate position and attitude estimates.

3.3.1.1 LOSA Sensor Mechanical Details

The core of the proposed tracing system is the LOSA sensor modules with optical slots. The sensor comprises of 4 LOSA sensor modules each connected to the central chassis (white) through adjustable arms (Figure 3.1). The sensor module enclosure acts a camera obscura and the optical slots act as camera apertures (Figure 3.2). Each sensor module enclosure fits onto a 'sensor module arm'.

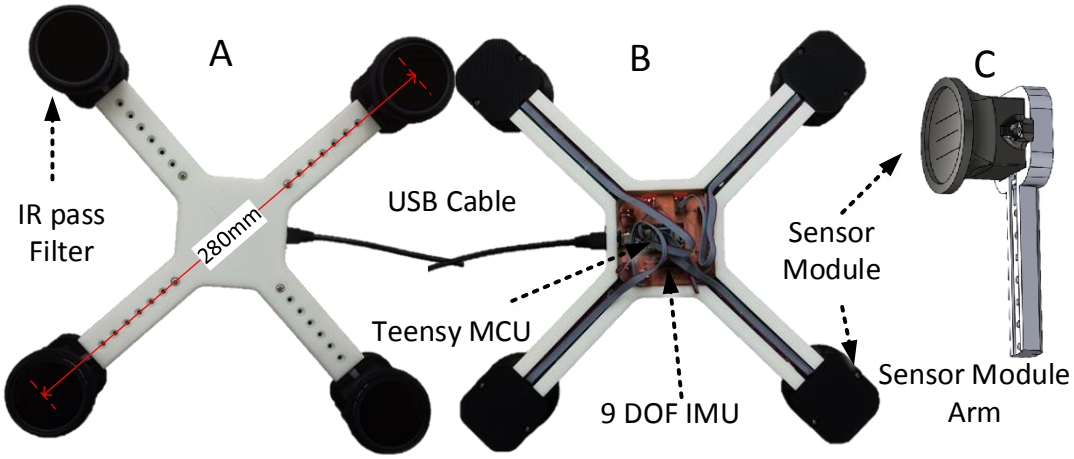

Figure 3.1: LOSA 3D tracking system: (A) Front View; (B) Rear View with cover removed; (C) CAD of sensor module arm [67].

The precise position of the sensors with respect to each other is ensured through the 3D printed (ABS plastic) chassis. In fully retracted condition, the stereoscopic baseline distance is 280 mm for each sensor module pair.

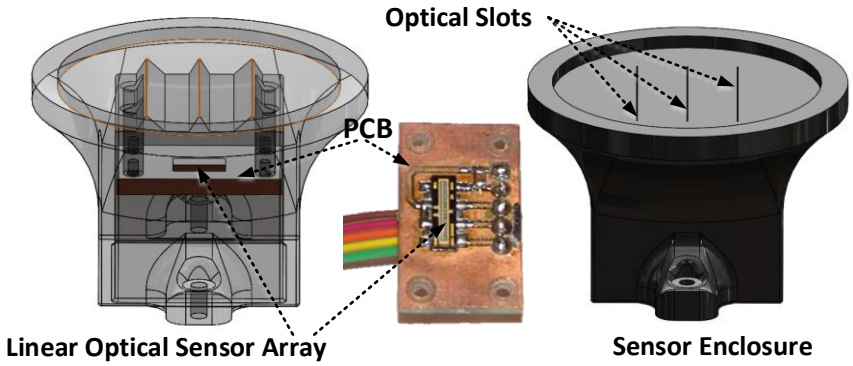

Figure 3.2: CAD model of the LOSA sensor assembly [67].

Furthermore, the guiding rail structure allows arm extension at 10 mm intervals, thus making the baseline adjustable to a maximum of 400mm for long range operations. To filter out noise due to ambient visible light, an IR-pass filter (850nm) was mounted on top of each sensor module.

3.3.1.2 Sensor Implementation

Each LOSA sensor module consists of a custom printed circuit board which carries the linear optical sensor array, a microcontroller, a cover box and visible light filter. Each module has a TSL1401CL 128-pixel linear array sensor manufactured by AMS AG. When two sensor modules are mounted and aligned with each other (Figure 3.1), this configuration enables planar sensing though triangulation. Compared to a 2D camera sensor, this setup greatly reduces total pixels to process (128 x 2 pixels vs 128 x 128 pixels) and thus dramatically increases the update rate. The optical sensor's photodiodes have a highly sensitive response to a broad spectrum of light and the peak responsivity wavelength of the photodiode is at around 800 nm, which is very close to the infrared LED wavelength used. An ARM Cortex-M4 based 96 MHz Teensy 3.2 board running a C program does all the computation and returns the position estimates at a user-selectable update rate.

The ARM microcontroller is programed to sample the four linear sensor arrays with analog-to-digital converters (ADCs), one ADC channel for each sensor array. With the high-speed sampling capability of the microcontroller's ADCs (1 Msps) the system just takes approximately 300 µs to read the data (512 data points) from the four sensors [71]. All sensors are sampled simultaneously and then read sequentially by the ADC. This also reduces the CPU time spent sampling and focuses on signal processing. The TSL1401R sensor consists of 128 photodiodes arranged in a linear array. Light energy impinging on

each photodiode generates photocurrent, which is integrated by the active integration circuitry associated with that pixel. By controlling the integration time, the exposure time of the sensor can be controlled to avoid sensor saturation (for short range) and signal amplification (large range). In addition to LOSAs, a 9-DOF IMU was connected to measure the dynamics of the tracking system. Limited by the UART serial speed and buffering issues, the sensor sent the IR data to the PC at an average update rate of ~115 Hz.

3.3.1.3 Pinhole Width and Sensor Positioning

Normally, the smaller the pinhole width, the sharper the image. But if the hole is too small, diffraction effects will occur and the image will become less clear due to the wave properties of light.

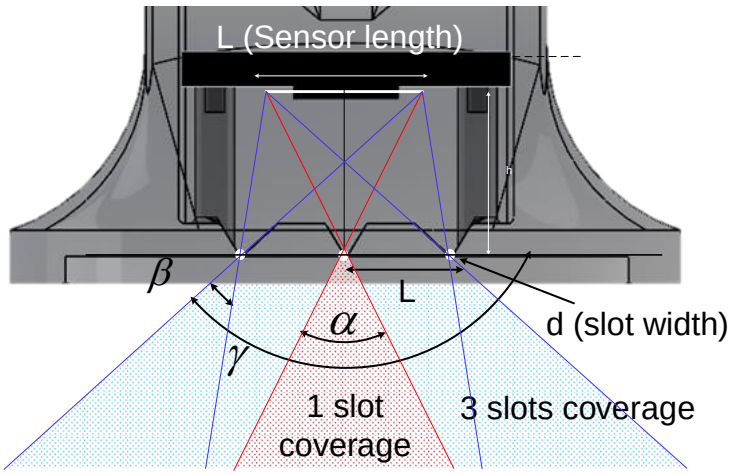

Figure 3.3: Field of view of a LOSA sensor module with three slots [67].

In addition, smooth slot edges and thin slot materials also reduce undesired diffraction. Petzval first found an easy method to calculate the optimal pinhole diameter/width [72]. The crispest image is obtained using a pinhole size determined by:

$$d = \sqrt{2h\lambda} \tag{3.1}$$

where d is pinhole diameter (slot width), h is focal length (distance from slot to image plane) and λ is the wavelength of light. Furthermore, it can be shown though trigonometry (Figure 3.3) that for a given slot width there exists a unique 'field of view' angle.

Due to limited field of view angle using a single slit, three optical slits were used in the sensor enclosure to increase the field of view. The distance between the adjacent slots was selected as same as the sensor length. This ensures that light passing thorough only one of the three slots creates significant image (intensity peak) on the sensor without creating any 'blind spots'. Given the IR source wavelength as λ=850 nm and sensor length L=8.0 mm the field of view angles (α, β and γ) are estimated as follows:

$$\alpha = 2\arctan\frac{L}{2h};\ \beta = \arctan\frac{1.5L}{h} - \frac{1}{2}\alpha;\ \gamma \approx \alpha + 2\beta \tag{3.2}$$

where, L is the distance between adjacent slits (same as sensor length) and h is the sensor height from slit plane. Table 3.1 shows the dependence of field-of-view angles and slot width to sensor height. To maximize field of view (γ) to 90° with slot width as limiting factor, the sensor height was chosen as 12mm.

Table 3.1: Relationship between sensor height and field of view

h(mm)	α (degree)	γ(degree)	d(mm)
4	90	143	0.08
8	53	112	0.11
12	**37**	**90**	**0.13**
15	24	77	0.16
25	18	51	0.20

3.3.1.4 Active LED Marker Implementation

The active marker is a battery powered IR LED light (850nm) source. It consists of four independent current controlled high power infrared LEDs mounted on the surface of a PCB tetrahedron, as shown in Figure 3.4. Each LED has a viewing angle of 110°, thus the tetrahedron structure enables the four LEDs to emit a signal in all directions. Each LED marker also hosts an InvenSense™ MPU9250® 9DOF IMU sensor. The marker is controlled by a marker control module equipped with ARM Cortex-M4 microcontroller (for onboard computation) and Xbee™ WiFi transceiver. The control module acquires the IMU data and integrates the angular rates to obtain attitude at an update rate of 450 Hz and finally sends the IMU and attitude data to the PC over a Wi-Fi network at an average update rate of 120 Hz. In return, it receives the LED peak values of IR intensities (received by the LOSA sensors) and position estimates from the PC.

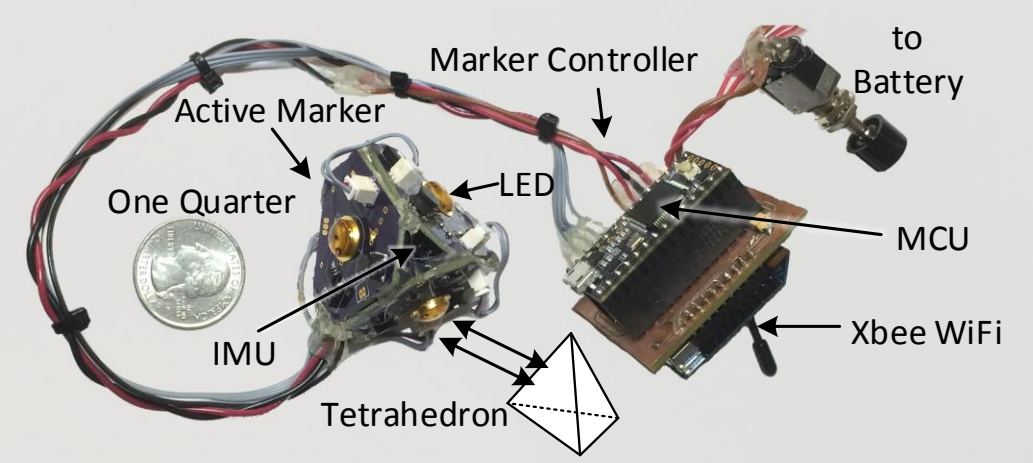

Figure 3.4: IR LED light source (Active Marker) with controller [67].

When powered ON, the active marker enters into 'calibration mode' for 5s. During calibration mode, the marker is kept stationary to estimate 'Line of Sight' (LoS) vector

(pointing towards the LOSA sensor in its frame of reference) and noise/bias in onboard gyroscope and accelerometer (explained in subsequent sections). After calibration period, the marker keeps track of the LoS vector (sensor direction) and the initial gravity vector by integrating rotation quaternion rates (obtained from IMU's angular rates after removing bias). The marker sends this tracked gravity and LoS vectors to the PC over Wi-Fi to attitude estimation. The marker uses the LoS vector for illuminating only that LED which faces the LOSA sensor the best. The marker computes vector dot product of the LoS vector with LED direction vectors and uses the result as expected LED intensities. Also, because of LED intensity feedback from the PC, the marker maintains the lowest LED intensity required to detect peaks reliably (20% of full scale value), further saving power. To prevent/minimize drifting issues in gyroscope data, the marker uses fresh readings from gyroscope to adjust gyroscope bias when the measured angular rates and accelerations are less than a preset threshold. Figure 3.5 shows the complete schematics of the proposed tracking system. The marker automatically switches to Calibration mode if the IR LOSA sensor loses IR intensities for more than 3s to correct gyroscope drifting issues.

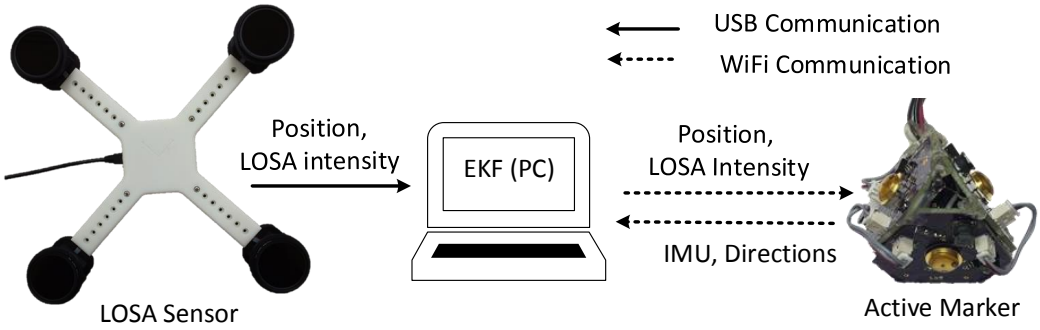

Figure 3.5: Schematics of the proposed tracking system.

3.3.1.5 Estimating Peak Values and Tracking Peaks

Since the spatial resolution of the LOSA sensor is just 128 pixels, the accurate subpixel peak estimation is extremely important. Figure 3.6(A) shows the raw data collected from one sensor module. It is observed that the peak width was always less than 7 pixels. Thus, a window of 7 pixels around the sampled peak position was used to estimate the analog peak position. To estimate the peak position linear interpolation was used in the peak region though a weighted least squares method. First, a window of ±3 pixel (total length, 7 pixel) around each signal maximum was isolated. Then, the approximate center position was estimated though a weighted mean of the indices of the pixels in the local maxima window where intensity values of correspond to the weights. This approximate center was then used to divide the pixels in the window into two groups (one on the left of the peak and another on the right). Then the weighted least squares method used to model the two groups of the points with two lines. The intersection of the two lines was taken as the peak position. Figure 3.6(B) shows peak estimation on one sample signal.

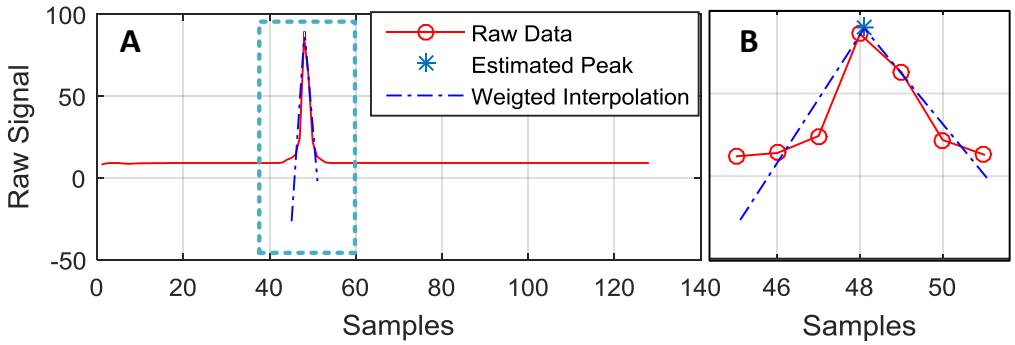

Figure 3.6: Peak Detection: (A) Raw data from one sensor module; (B) Estimated peak position on zoomed peak area.

Since the sensor module geometry ensures that light from only one slot results in a peak on the sensor, it is necessary to estimate which slot the light passed through. An algorithm was implemented to estimate and track the slot ID. It is assumed that all the peaks originate

from the central slots. The microcontroller in LOSA sensor keeps track of the location of all the detected peaks. Whenever a sudden the change is detected in peak location, 128 (length of sensor in pixels) is added or subtracted from the peak positions depending on the direction of motion of the peak. This process virtually adds extra length to the optical sensor strip and hence increases the spatial range of the sensor. These peak locations are then used to estimate actual position of the active marker (LEDs) with respect to the tracking system.

3.3.2 Data Fusion using EKF for 3D Position and Attitude Tracking

The proposed tracking system measures position and orientation with the help of LOSA sensor. Since the active marker is equipped with 9-axis IMU, inertial data from the marker can be used to supplement the optical sensing data to improve position and attitude estimates. The proposed system uses Extended Kalman Filter (EKF) which is a standard approach for state estimation problems involving nonlinear systems [73], [74].

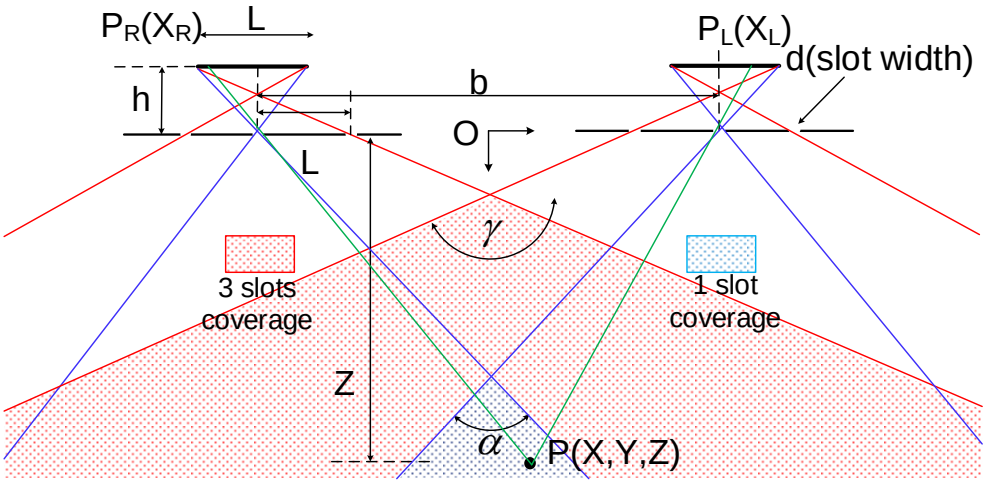

Figure 3.7: LOSA sensor pair geometry for triangulation [67].

3.3.2.1 Position Measurement

Position estimates of the tracker are obtained through planer stereovision. Given a pair of aligned sensors (Fig. 3.7), the planar (x-z plane) position of the light source may be calculated using stereo triangulation as follows.

$$\frac{x_L}{h} = \frac{X - b/2}{Z}, \quad \frac{x_R}{h} = \frac{X + b/2}{Z}. \tag{3.3}$$

After solving equation (3.3) for X and Z, we get:

$$X = b\frac{x_L + x_R}{2(x_L - x_R)}, \quad Z = b\frac{h}{x_L - x_R}. \tag{3.4}$$

The position shifting between two linear sensors is called the disparity *d*. From eqn. 3.4, depth information (*Z*) is uniquely determined by disparity and is inversely proportional to *d*. Therefore, measuring object position is reduced to the problem of finding photographic mapping of the object location on each sensor (and) with respect to optic center of on each sensor. The optic centers of each of the four LOSA modules were estimated using a simple calibration experiment. Since the baseline is variable while the sensor's spatial resolution is limited (128 pixels), the baseline effectively defines the operational range of the system (Equation 3.4). As the distance between the marker and the sensor increases the disparity decreases and approaches the noise level. This defines the upper limit of the sensing range. Increasing the baseline adds 'offset' in stereo disparity (Fig. 3.7) and hence raises the upper limit of the sensing range. The lower limit of the sensing range also rises with increase in baseline due to decrease in common coverage region (shaded region in Fig. 3.7). The rate of increase is greater in the upper limit than that of the lower, thus increasing the baseline increases the active range of the sensor. A similar calculation can be performed to find a

(Y, Z) pair to obtain 3D position estimates. These position estimates are also differentiated with respect to time to obtain 3D velocity estimates.

3.3.2.1 Attitude Estimation

Since the IMU magnetometer is susceptible to stray magnetic fields, it cannot be used for attitude estimation. To estimate the attitude of the marker with respect to the sensor, two non-parallel vectors viz. LoS and Gravity are used. During the calibration mode, the marker, which is kept stationary, measures acceleration to get the gravity vector. To estimate the LoS vector, the marker lights the LEDs (one LED at a time) in a fixed pattern and receives corresponding LED intensities from the LOSA sensors over Wi-Fi. Since the direction vectors for each LED is known in the marker's frame of reference (due to the tetrahedron shape), the LoS vector of the sensor is estimated by taking the weighted average of the LED's direction vectors. The weights of the weighted average are obtained by the IR intensities received by LOSAs during the calibration phase.

Since the LOSA cannot differentiate between simultaneous light from different LEDs, it is not possible to estimate the LoS in real-time. Therefore, the system relies on integration of angular rates for the estimation of attitude. The integration errors in attitude estimates were corrected with the help of position updates. The position and attitude estimates are linked with each other through velocity updates, as the net acceleration includes attitude information in the form of rotation matrix. The LoS vector and the gravity vector are two vectors which are known in both frames of reference (as shown in Fig. 3.8). These pairs of vector can be used to obtain attitude of the marker with respect to the sensor.

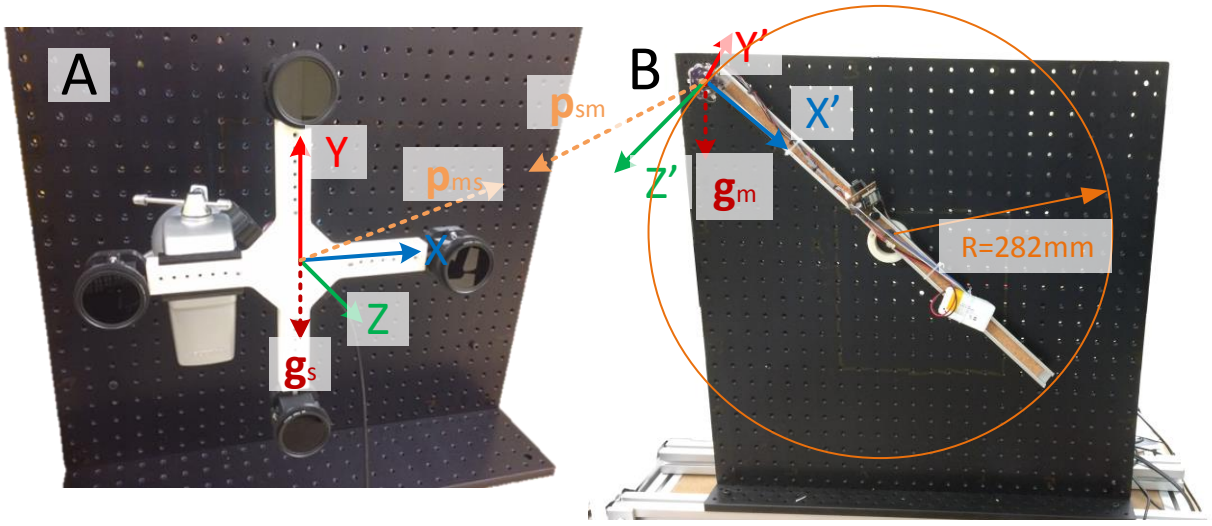

Figure 3.8: Experimental Setup with coordinate frames (mounting plates are parallel and face each other) (A) tracking system; (B) Active LED marker [67].

$$\begin{aligned} \boldsymbol{g}_m &= \boldsymbol{R}_s^m \boldsymbol{g}_s; \quad \boldsymbol{g}_s = \begin{bmatrix} 0 & -g & 0 \end{bmatrix}^T, \\ \hat{\boldsymbol{r}}_{sm} &= -\boldsymbol{R}_s^m \hat{\boldsymbol{r}}_{ms}; \quad \boldsymbol{r}_{ms} = \begin{bmatrix} r_x & r_y & r_z \end{bmatrix}^T, \hat{\boldsymbol{r}}_{ms} = \boldsymbol{r}_{ms} / \left\| \boldsymbol{r}_{ms} \right\| \end{aligned} \tag{3.5}$$

Where, $\boldsymbol{g}$ is gravity vector, $\boldsymbol{R}_s^m$ is the rotation matrix to transform coordinates from sensor to marker's frame of reference, $\hat{\boldsymbol{r}}_{ms}$ represent the direction vector $\boldsymbol{r}_{ms}$ is the position estimate of the marker. The subscripts *s* and *m* denote sensor and marker frame of reference respectively. $\boldsymbol{R}_s^m$ can also be written in terms of unit quaternion vector $\boldsymbol{Q} = [q_0 \quad q_1 \quad q_2 \quad q_3]^T$ as shown in eqn. (3.6).

$$\boldsymbol{R}_s^m(\boldsymbol{Q}) = \begin{bmatrix} 1-2(q_1^2+q_2^2) & 2(q_0q_1+q_3q_2) & 2(q_0q_2-q_3q_1) \\ 2(q_0q_1-q_3q_2) & 1-2(q_0^2+q_2^2) & 2(q_1q_2+q_3q_0) \\ 2(q_0q_2+q_3q_1) & 2(q_1q_2+q_3q_0) & 1-2(q_0^2+q_1^2) \end{bmatrix} \tag{3.6}$$

where, $\boldsymbol{Q}$ represent the rotation (attitude) of the marker with respect to the sensor's frame of reference. Since $\hat{\boldsymbol{r}}_{ms}$ and $\boldsymbol{g}_m$ are by known from the measurements taken during calibration mode of the markers, the rotation matrix $\boldsymbol{R}_s^m$ can be obtained by solving eqn.

(3.5). This rotation matrix can be used to calculate $\boldsymbol{Q}$ and subsequently Euler angles to represent attitude in 'human readable' format. This rotation quaternion $\boldsymbol{Q}$ is updated by integrating angular rates on microcontroller to obtain attitude of the marker in real-time.

3.3.2.2 System Modeling

As mentioned above, EKF was used to fuse IMU and optical tracking data to obtain position and attitude estimates of the active marker with respect to LOSA sensor. Initial position and attitude of the active tracker were obtained from LOSA sensor at system initialization. In addition to these position and attitude estimates, the marker's real-time angular rates and linear acceleration are used to further improve tracking accuracy with the help of EKF. The system has been modelled in a similar way as proposed by [74].

The state vector for the EKF composed of position, velocity and rotation (unit) quaternion estimates of the marker with respect to the sensor's frame of reference. To fuse attitude information with linear position/velocity information, linear acceleration measurement from the marker's IMU was used. The acceleration measured by the IMU on the marker consists of three components viz. gravity, rotational acceleration and linear acceleration.

$$\overrightarrow{\boldsymbol{acc}}^{s} = \boldsymbol{R}_{m}^{s}(\boldsymbol{Q}) \begin{bmatrix} a_{X'}^{m} - \omega_{Y'}^{m} V_{Z'}^{m} + \omega_{Z'}^{m} V_{Y'}^{m} \\ a_{Y'}^{m} + \omega_{X'}^{m} V_{Z'}^{m} - \omega_{Z'}^{m} V_{X'}^{m} \\ a_{Z'}^{m} - \omega_{X'}^{m} V_{Y'}^{m} + \omega_{Z'}^{m} V_{Y'}^{m} \end{bmatrix} - \begin{bmatrix} 0 \\ -g \\ 0 \end{bmatrix} \tag{3.7}$$

Here $\overrightarrow{\boldsymbol{acc}}^{s}$ represent the linear acceleration vector experienced by the marker in tracker's frame of reference whereas $a_{X',Y',Z'}^{m}$ and $\omega_{X',Y',Z'}^{m}$ represent the IMU readings (accelerometer and gyroscope respectively) for the marker in marker's frame of reference. The state

estimates were updated by integrating measurements and previous state estimates as follows:

$$\begin{bmatrix} \vec{\boldsymbol{p}}_{k+1}^{s} \\ \vec{\boldsymbol{v}}_{k+1}^{s} \\ \boldsymbol{Q}_{k+1} \end{bmatrix} = \begin{bmatrix} \vec{\boldsymbol{p}}_{k}^{s} + \vec{\boldsymbol{v}}_{k}^{s}.\delta t \\ \vec{\boldsymbol{v}}_{k}^{s} + \boldsymbol{R}_{m}^{s}\left(\vec{\boldsymbol{a}}_{k}^{m} - \boldsymbol{R}_{s}^{m}\boldsymbol{g}_{s} - \vec{\boldsymbol{\omega}}_{k}^{m} \times \boldsymbol{R}_{s}^{m}\vec{\boldsymbol{v}}_{k}^{s}\right).\delta t \\ \boldsymbol{Q}_{k} + \dot{\boldsymbol{Q}}_{k}(\boldsymbol{Q}_{k}, \vec{\boldsymbol{\omega}}_{k}^{s}).\delta t \end{bmatrix}. \tag{3.8}$$

The quaternion rate was obtained from measured angular rates as follows [75]:

$$\dot{\boldsymbol{Q}}(\boldsymbol{Q}, \vec{\boldsymbol{\omega}}) = 0.5\begin{bmatrix} q_0 & q_3 & -q_2 & q_1 \\ q_1 & q_2 & q_3 & -q_0 \\ q_2 & -q_1 & q_0 & q_3 \\ q_3 & -q_0 & -q_1 & -q_2 \end{bmatrix}\begin{bmatrix} 0 \\ \omega_x \\ \omega_y \\ \omega_z \end{bmatrix}. \tag{3.9}$$

As, only linear velocity and position are the only observable system variables, following observation model was used.

$$\begin{bmatrix} \vec{\boldsymbol{p}} \\ \vec{\boldsymbol{v}} \end{bmatrix} = \begin{bmatrix} \boldsymbol{I}_3 & 0 & 0 \\ 0 & \boldsymbol{I}_3 & 0 \end{bmatrix}\begin{bmatrix} \vec{\boldsymbol{p}}_{k}^{s} \\ \vec{\boldsymbol{v}}_{k}^{s} \\ \boldsymbol{Q}_{k}^{s} \end{bmatrix} \tag{3.10}$$

where $\boldsymbol{I}_3$ represents an identity matrix of size 3.

3.3.2.3 EKF Implementation

As the Cortex M4 microprocessor is not powerful enough to run EKF in real time, EKF was implemented on PC using NI LabVIEW® (Figure 3.9). In general, EKF can be used to solve for any non-linear stochastic process of form:

$$\left.\begin{aligned} \boldsymbol{x}_k &= f\left(\boldsymbol{x}_{k-1}, \boldsymbol{u}_k\right) + \boldsymbol{w}_k \\ \boldsymbol{y}_k &= h\left(\boldsymbol{x}_k\right) + \boldsymbol{v}_k \end{aligned}\right\} \quad \boldsymbol{w}_k \in N\left(\vec{\boldsymbol{0}}, \boldsymbol{Q}_k\right), \boldsymbol{v}_k \in N\left(\vec{\boldsymbol{0}}, \boldsymbol{R}_k\right) \tag{3.11}$$

where $\boldsymbol{x}_k$ is the state vector, $\boldsymbol{u}_k$ is the control input vector and $\boldsymbol{w}_k$ and $\boldsymbol{v}_k$ are the process and measurement noise vectors, respectively. The noise vectors $\boldsymbol{w}_k$ and $\boldsymbol{v}_k$ are assumed to follow multivariate Gaussian distribution with $\boldsymbol{Q}_k$ and $\boldsymbol{R}_k$ as covariance matrices. The state and measurement models (eqn. 3.11) are linearized making use of Jacobian Matrices $\boldsymbol{F}$ and $\boldsymbol{H}$.

$$\boldsymbol{F}_k = \left.\frac{\partial f}{\partial \boldsymbol{x}}\right|_{\boldsymbol{x}=\hat{\boldsymbol{x}}_k,\boldsymbol{u}_k}, \boldsymbol{H}_k = \left.\frac{\partial h}{\partial \boldsymbol{x}}\right|_{\boldsymbol{x}=\hat{\boldsymbol{x}}_k} \tag{3.12}$$

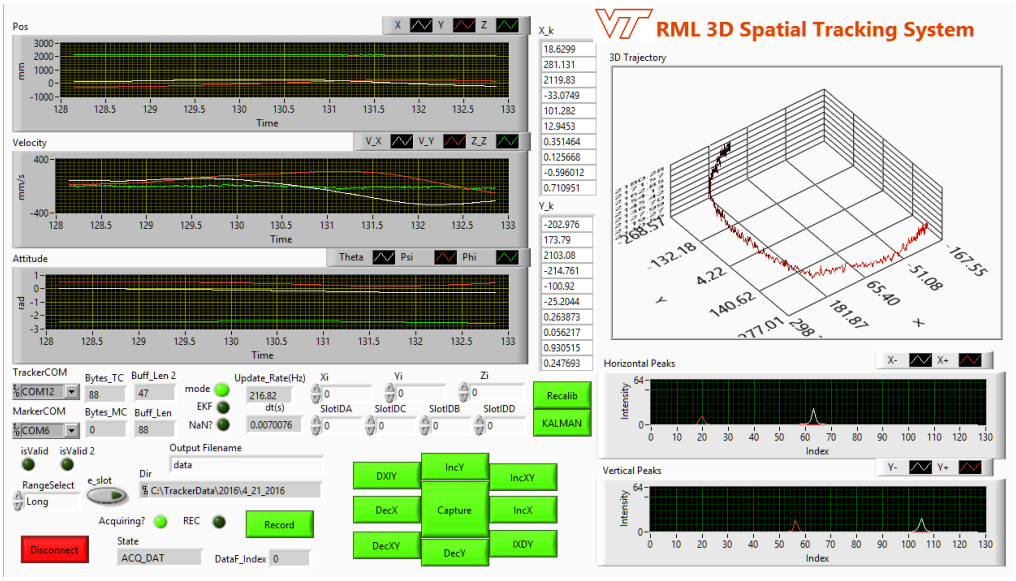

Figure 3.9: LabVIEW GUI for the LOSA tracking system [67].

During 'prediction' stage of EKF, state estimates ($\hat{\boldsymbol{x}}$) and covariance matrix for state estimates ($\boldsymbol{P}$) are predicted as follows:

$$\begin{aligned} \hat{\boldsymbol{x}}_{k|k-1} &= f\left(\boldsymbol{x}_{k-1|k-1}, \boldsymbol{u}_k\right) \\ \boldsymbol{P}_{k|k-1} &= \boldsymbol{F}_k \boldsymbol{P}_{k-1|k-1} \boldsymbol{F}_k^{\,T} + \boldsymbol{Q}_k \end{aligned} . \tag{3.13}$$

After prediction stage, these estimates are corrected on the basis of measurements during 'update' stage of EKF as follows:

$$
\begin{aligned}
\tilde{\boldsymbol{y}} &= \boldsymbol{y}_k - h\left(\hat{\boldsymbol{x}}_{k|k-1}\right) \\
\boldsymbol{S}_k &= \boldsymbol{H}_k \boldsymbol{P}_{k|k-1} \boldsymbol{H}_k{}^T + \boldsymbol{R}_k \\
\boldsymbol{K}_k &= \boldsymbol{P}_{k|k-1} \boldsymbol{H}_k{}^T \boldsymbol{S}_k{}^{-1} \\
\hat{\boldsymbol{x}}_{k|k} &= \hat{\boldsymbol{x}}_{k|k-1} + \boldsymbol{K}_k \tilde{\boldsymbol{y}} \\
\boldsymbol{P}_{k|k} &= \left(\boldsymbol{I} - \boldsymbol{K}_k \boldsymbol{H}_k\right) \boldsymbol{P}_{k|k-1}
\end{aligned}
\tag{3.14}
$$

where $\tilde{\boldsymbol{y}}$, $\boldsymbol{S}_k$, $\boldsymbol{K}_k$ and $\boldsymbol{I}$ represent measurement residuals, residual covariance matrix, Kalman gain and identity matrix respectively.

3.3.3 Tracking System Evaluation

To acquire, process and record tracking data, a LabVIEW™ based GUI was created (Fig. 3.9). The GUI running on a notebook powered by Intel core i7™ processor was able to deliver state estimates at an update rate of more than 310Hz. The GUI also plotted the 3D trajectory of the marker at an update rate of 20Hz. Figure 3.8 shows the experimental setup. For evaluating the positional accuracy of the sensor, the tracking system (sensor) was mounted rigidly on a mechanical breadboard (mounted on a guiding rail). The active marker was connected to a rod hinged on another mechanical breadboard (parallel to the tracking system plane) mounted on the same guiding rail. This setup constrained the motion of the marker on a circle in a plane parallel to the sensor plane. The maker was moved on circular trajectory of radius 282mm from distances varying from 2m to 5.5m and positions estimates were recorded. Since the position and radius of the circular trajectory is known from measurements (with accuracy ±10mm and ±1mm respectively), the measured position estimates were compared with the expected circular trajectory. To assess the positional accuracy of the tracking system, the system was tested indoors at different distances in extended range mode (400mm baseline). The extended range mode was

deliberately selected because long range indoor tracking is more critical in most applications.

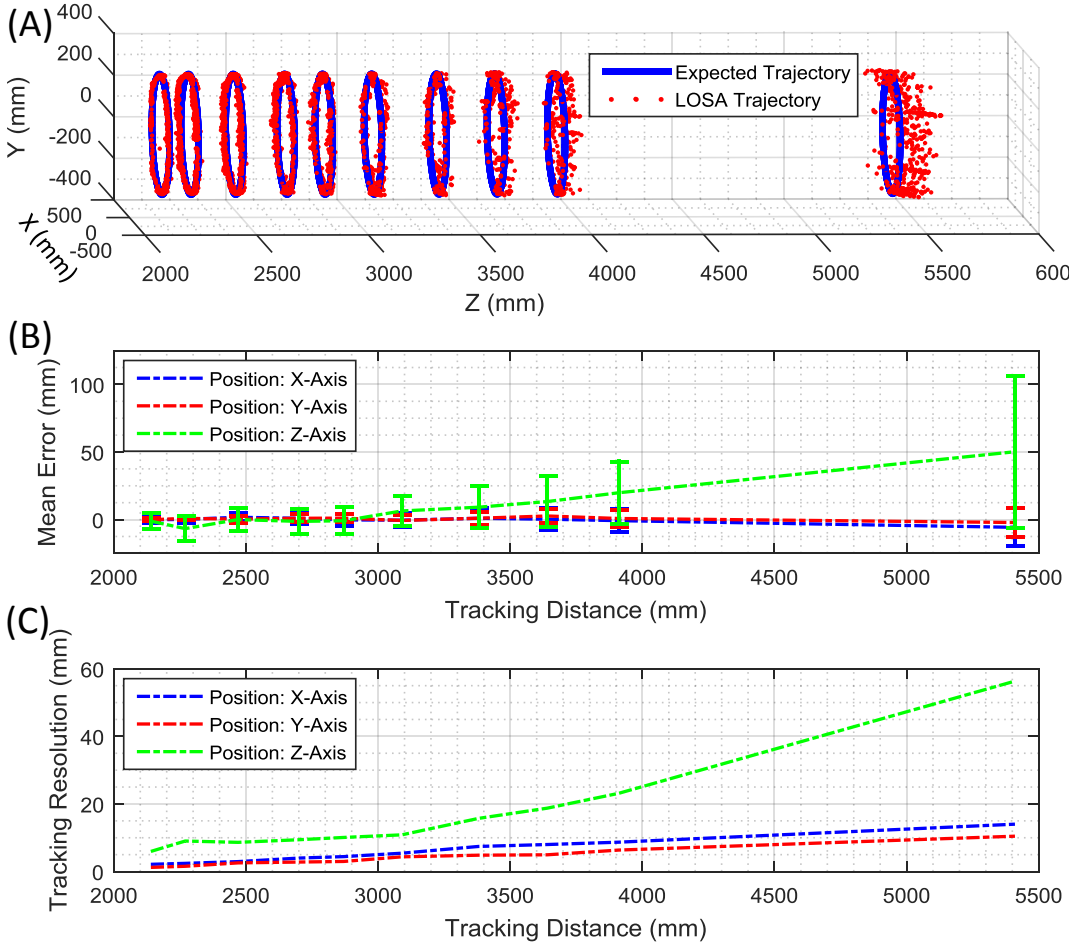

Figure 3.10: Positional accuracy and resolution of the LOSA sensor at different operating ranges [67]: (A) Position Estimates; (B) Sensor Positioning Error; (C) Sensor Tracking Resolution

Positional resolution is essentially determined by the 'signal to noise ratio' (SNR) of the sensor data. Since the signal (stereovision disparity) decreases with distance, and the sensor noise remains constant, the SNR decreases with distance and so does the resolution. The sensor resolution was defined as 'one standard deviation' (1σ) in the sensor reading. Fig. 3.10 shows position estimates for the marker when rotated with the rod as shown in experimental setup and compares measured position estimates from sensor with expected

trajectory. It also shows measured positional error in the form of mean and standard deviation for the same trajectories. It also shows the sensor resolution at different operating ranges.

It was observed that the mean error (accuracy) in position estimates varied from 1.18mm to 50.56mm with tracking distance varying from 2.1m to 5.4m, respectively. EKF implementation proved to be effective in removing noise and improving position estimates. Figure 3.11 compares EKF position estimates and raw position measurements with the expected values.

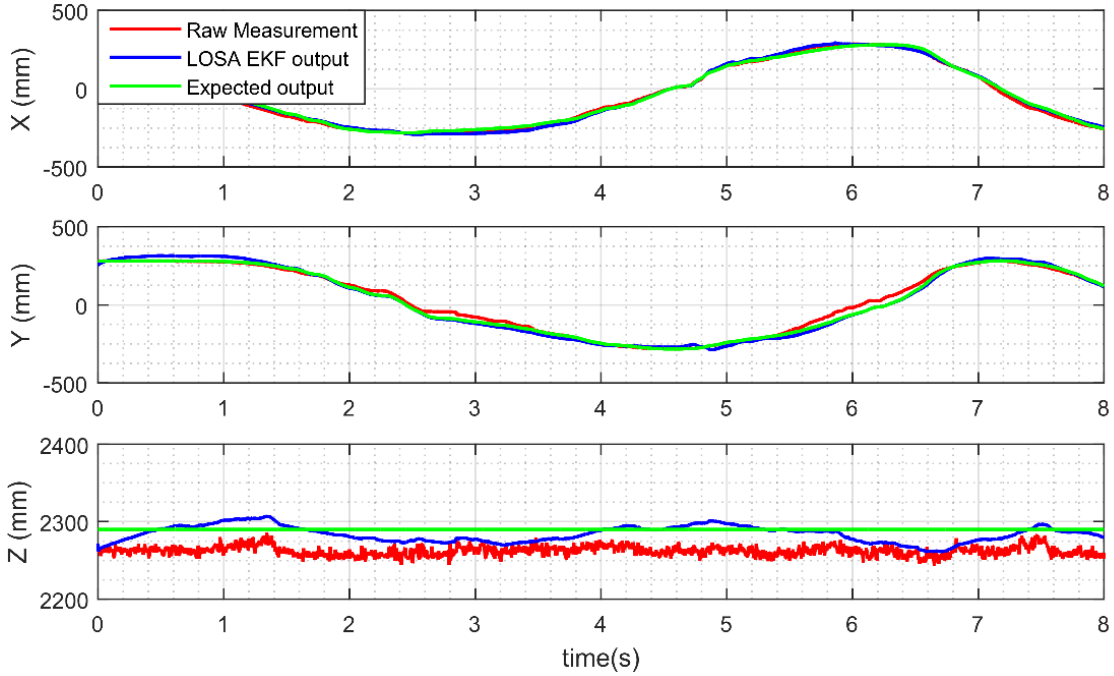

Figure 3.11: Comparison of EKF output with raw positional estimates [67].

To assess the accuracy of the orientation estimates from the proposed sensor, Euler angles extracted in post-processing from the proposed sensor were compared with commercially available VN200 INS/AHRS sensor[76]. For this experiment, the Active marker was rigidly attached to VN200 sensor to align measurement axes, and the assembly was rotated (±90°) along the three axes with respect to initial orientation. Figure 3.12 shows

yaw, pitch and roll estimates from proposed LOSA sensor and VN200. Attitude estimates from the prosed sensor closely matched with those from VN200 sensor.

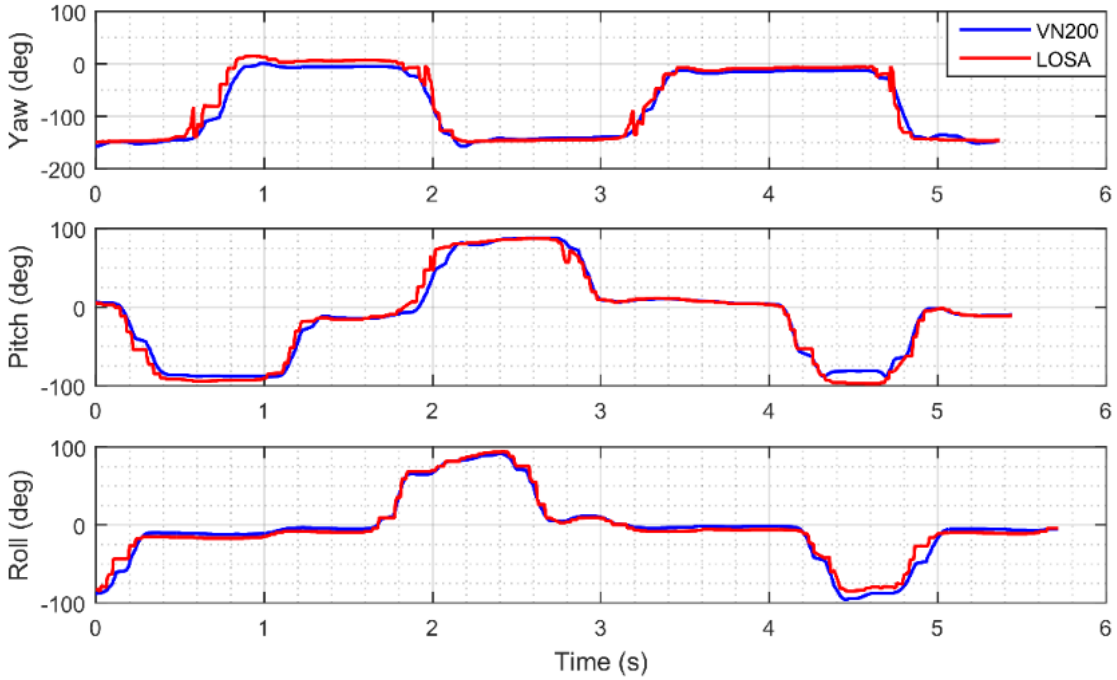

Figure 3.12: Dynamic orientation measurement with VN200 INS and proposed LOSA tracking system [67].

The power consumption of the four sensors (and IMU) and the controller are about 32 mA (3mA ×4 +20mA) and 20 mA at 5 V separately, or around 260 mW. The tracking system was powered though USB connection. Power consumption by the active marker is greatly reduced through optimization of the LED brightness. The marker automatically adjusts LED intensities to light up only one LED (facing the tracker) and maintains a minimum intensity required to detect peaks reliably in sensor. The active marker consumes about 145mA and 260mA current at 7.4V during indoor operations at 2m and 5m range respectively. For outdoor operations this power can be raised up to 500mA.

3.4 Wind Map Generation

The presented motion tracking system can be combined with an ultrasonic anemometer to map wind flow field. To generate artificial turbulent wind conditions similar to the ship airwake, a setup of two 24-inch diameter fans placed opposite to each other was implemented (Fig. 3.13A).

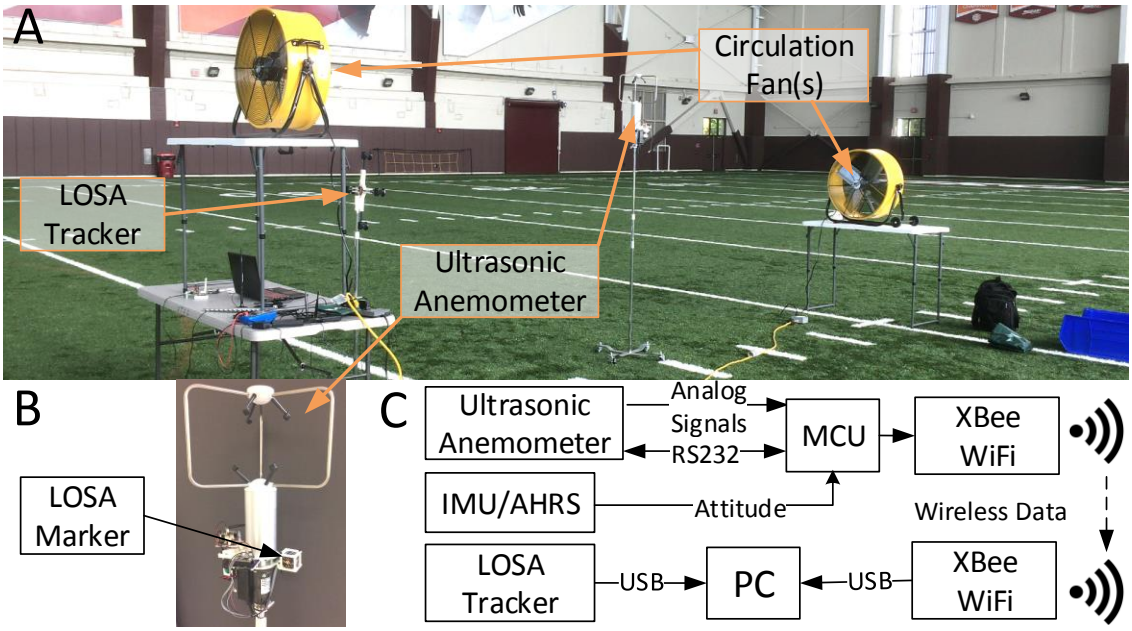

Figure 3.13: (A) Wind mapping setup [77]; (B) Ultrasonic anemometer; (C) Electrical schematics.

The system used a Young® 81000 3-axis ultrasonic anemometer mounted on a pole (with caster wheeled base) as the primary sensor [78]. The anemometer was interfaced with using an ARM® Cortex M4 microcontroller through analog inputs. The micro controller also hosted a 9-axis IMU with AHRS implementation. The attitude-corrected wind flow measurements were sent to a PC for recording over a Wi-Fi network. The anemometer was also retrofitted with a LOSA marker for tracking the motion of the anemometer with respect to the already stationary LOSA tracker (Fig. 3.13B, 3.13C). The active marker for

the LOSA tracker was rigidly mounted on the anemometer and the motion parameters like position, velocity, and attitude were measured along with wind velocity in real-time. The attitude measurements were used to rotate the measured wind vectors from the sensor's frame of reference to the tracker's frame of reference. Furthermore, the velocity measurements obtained from the tracker were subtracted from the wind measurements to compensate for any motion in the anemometer readings.

To obtain the wind flow map, the anemometer was placed at discrete locations on dense serpentine trajectories at different heights, and the compensated wind velocities were recorded with 3D position vectors in the global (fan) frame of reference. At each location, the wind flow was recorded for at least 20s at an update rate of 100 Hz. For each location, both mean flow and turbulent component of the wind flow were computed using this recorded data.

As mentioned before, the helicopter dynamics are significantly affected by the external wind flow pattern generated by the cruising vessel. As it is not possible to measure wind velocity at every point in space around the helicopter, the wind flow is approximated using a parametrized model based on a finite number of measurements. As shown in equation (12) the localized wind flow in the rotor hub's frame of reference is assumed to be composed two components: steady-state/mean (with subscript *S*) and turbulent (with subscript *T*) and modelled as a Gaussian process. The (mean) steady-state flow component, being predictable, is modeled using 12 parameters linear model whereas the turbulent component, being stochastic in nature, has been modelled as a random variable with Gaussian distribution:

$$\begin{bmatrix} u_x \\ u_y \\ u_z \end{bmatrix}_{wh} = \left\{ \begin{bmatrix} a_x & b_x & c_x \\ a_y & b_y & c_y \\ a_z & b_z & c_z \end{bmatrix} \begin{bmatrix} x \\ y \\ z \end{bmatrix} + \begin{bmatrix} d_x \\ d_y \\ d_z \end{bmatrix} \right\}_S + \begin{bmatrix} u_x \\ u_y \\ u_z \end{bmatrix}_T . \quad (3.15)$$

Here, u_{wh} is the wind velocity vector at a position vector $[x, y, z]^T$ with respect to the rotor hub in helicopter's frame of reference and $s\psi$ and $c\psi$ represent sine and cosines of the rotor position angle ψ respectively.

To obtain the steady-state wind flow, for each location of the data recorded, a 12 parameter linear model (eqn. 3.15) was fitted on the wind measurements within a volume of 1.3 m × 1.3 m × 0.6 m (equivalent to helicopter's size) using the least square method. In the model (12), the vector $[d_x, d_y, d_z]^T$ represents the mean steady-state flow vector in the volume. The steady state mean wind flow parameters were then interpolated to a 3D grid of 5 cm size using bilinear interpolation to generate a 3D wind map for the experiment.

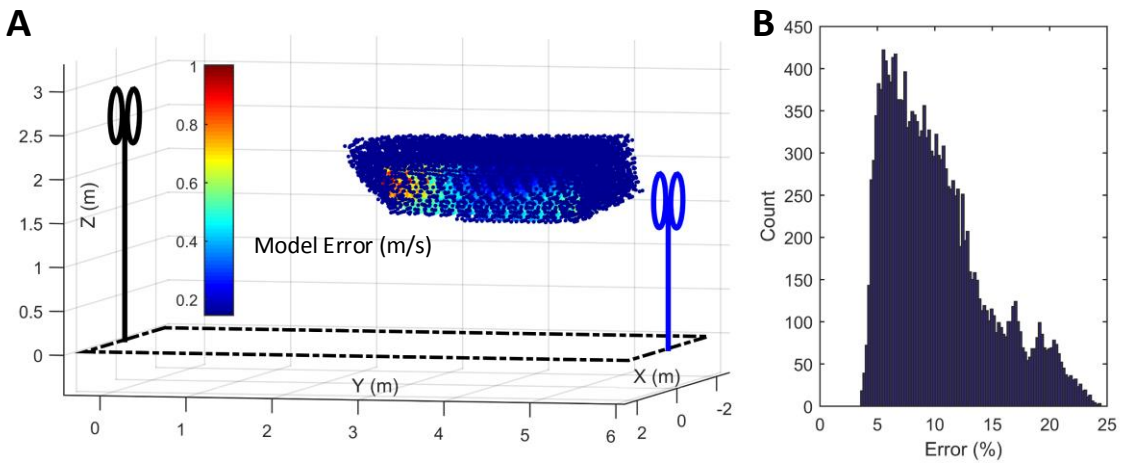

Figure 3.14: Validation of steady state wind model: (A) Spatial distribution of modeling error; (B) Histogram distribution of model error as a percentage of input wind.

To assess the accuracy of this model (eqn. 3.15) the interpolated steady-state flow parameters were compared against the interpolated measured flow. Figure 3.14A shows the spatial distribution of the error in modeling the measured wind flow with respect to the

measured flow. As shown in the histogram (Fig. 3.14B) of the model deviations, represented as a percentage of the wind flow of 7.24 m/s at the source (circulation fans), most of the modeling error falls in 3-11% error bracket. High error zones are visible on the corner of the modeled volume is due to the boundary effects of the interpolation process.

The turbulent component of the wind map was characterized by the standard deviation of the wind measurements after removing the steady-state component. The turbulence intensity was computed as the norm of the standard deviations of the 3-axis wind velocity measurements after subtracting the steady-state component (from the linear model) within the sample volume of 1.3 m × 1.3 m × 0.6 m. Similar to the steady-state flow, the turbulence map was generated by interpolating the turbulence intensity at a 3D grid of 5 cm.

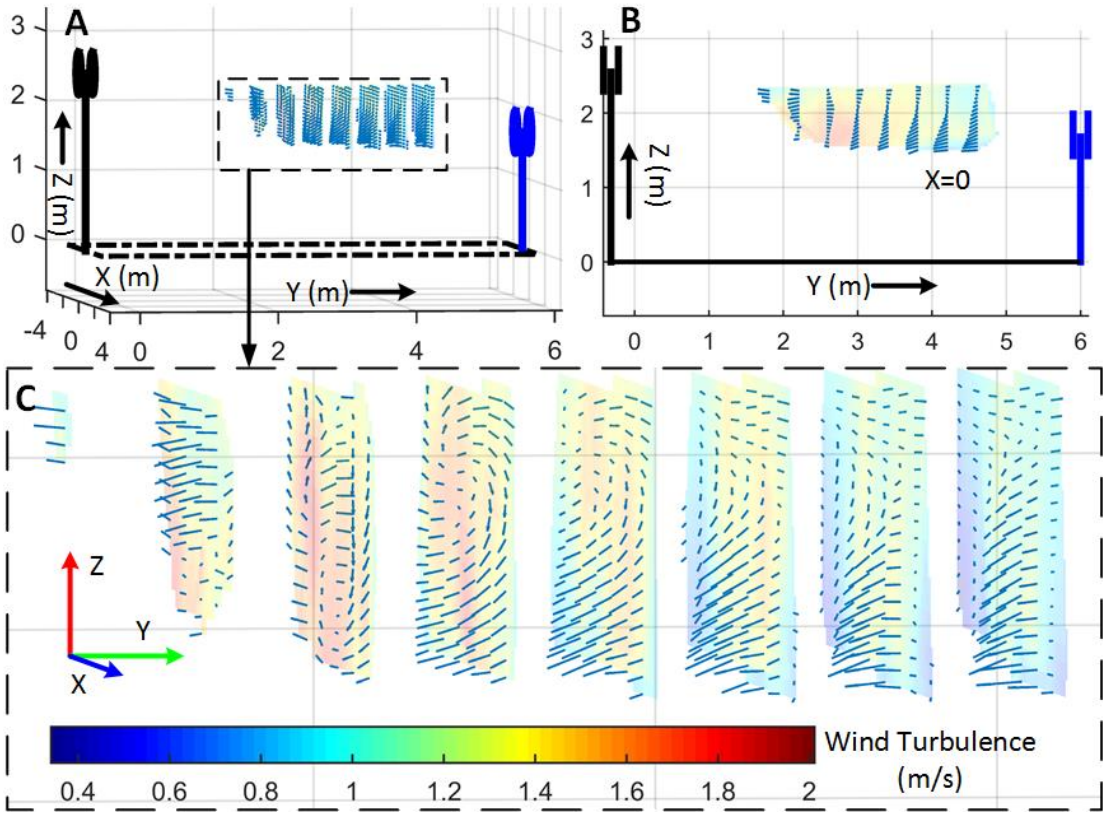

Figure 3.15: Indoor wind flow map: (A) 3D steady-state wind flow with turbulence map; (B) Sectional view of the 3D flow field at plane X=0; (C) Zoomed-in flow field.

Fig. 3.15 shows the final wind flow map generated by the experimental fans setup (Fig. 3.13). Here, the arrow field represents 3D mean wind flow field and color represent the wind turbulence content of wind flow in the form of standard deviation of the local wind speed. This spatial wind data was used for the calibration and testing of the various models presented in this dissertation for the estimation wind conditions from helicopter dynamics.

CHAPTER 4: WIND ESTIMATION FROM RC HELICOPTER USING CALIBRATED NEURAL NETS

This study presents the detailed mechatronic design and analysis of a wireless sensing platform developed for the experimental mapping and validation of the airwake generated by cruising naval vessels. The proposed telemetry approach models the dynamic response of the helicopter to pilot inputs under artificially created wind conditions and then uses neural network based models to estimate the airwake distribution. The telemetry system uses a wireless sensor network comprising of sensors like an Inertial Measurement Unit (IMU), optical trackers, and GPS sensors to measure the dynamics of the flying RC helicopter. The system was trained and calibrated in a climate controlled indoor environment with artificially created wind conditions. This chapter focuses on both hardware and software aspects of the latest iteration of the proposed telemetry system. Similar to the previous studies, the presented telemetry system was also tested outdoors with a modified YP676 naval training vessel in the Chesapeake Bay area, under a wide range of wind conditions and the results were compared against CFD simulations

In contrast to the previous studies [11], [28]–[30], this chapter presents a calibration strategy for the sensor system through experimental flight testing in a controlled wind setup. This chapter of the dissertation focuses on the design and analysis of a wireless telemetry system intended to simultaneously measure helicopter dynamics, location and pilot inputs at a high update rate. This chapter also presents a novel mechatronics platform to generate and map reproducible wind flow conditions in an open indoor environment to calibrate aerodynamics of a flying RC helicopter. It also offers an extended analysis of the

interaction of ship airwake with a flying RC helicopter using localized wind flow models. This study also presents an analytical analysis to identify factors affecting a helicopter dynamics and use these parameters with an Artificial Neural Networks-Particle Swarm Optimization (ANN-PSO) based machine learning approach to model dynamics of an RC helicopter. Also, this analysis demonstrates linear mixing of pilot components and local wind components in the aerodynamics of the helicopter, and then uses the same property to extract and map wind turbulence.

The main benefit of this approach is its non-contact long-range mobility, which does not alter the airwake readings due to physical linkages coupled with ship motion or the formation wakes arising from mechanical linkages (as in the case of wind tunnels). At the same time, pilot input compensation features of the system ensure unbiased ship airwake measurements. The system's capability to extract ship airwake is tested in an indoor calibration experiment where the helicopter was flown in artificially created wind turbulence. In addition, this study also models the effect of turbulence from uncertainty in angular acceleration, which delivers better correlation with the wind turbulence pattern. This chapter also presents the outdoor testing performance of the system with an YP676 naval patrol craft and compares against results obtained from CFD analysis in previous studies.

4.1 Interaction between Helicopter and Ship Airwake

As is widely known, helicopter control is realized through thrust vectoring by using a swash plate mechanism [37]. The swash plate couples the main rotor rotation and rotor pitch control, thus making the blade pitch angle a function of the rotor position.

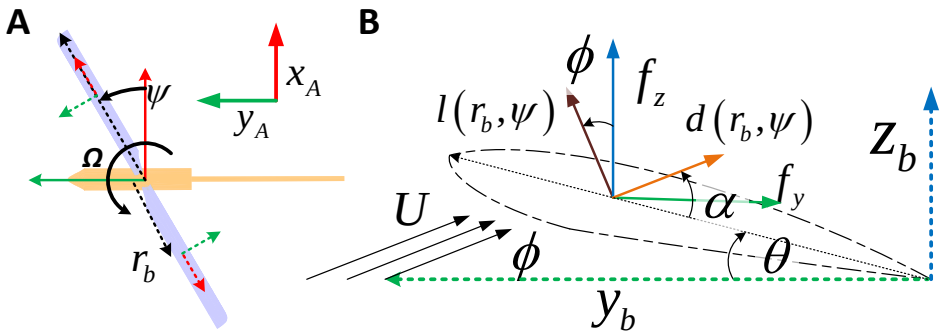

Figure 4.1: (A) Frame of reference assignment for the helicopter's fuselage and rotor blades; (B) Aerodynamic loads on an airfoil section of rotor blade [79].

Fig. 4.1 shows the frame of reference assigned to the helicopter's fuselage along with the lift and drag generated by an airfoil section of a rotor blade. The lift and drag experienced on an airfoil section of a rotor blade is dependent on the angle of attack of the relative wind, which in turn depends on wind conditions, pilot inputs, and the helicopter's motion. To make the role of wind conditions on the helicopter dynamics apparent, a single blade coordinate system has been followed. Equation (4.1) shows lift (l) and drag (d) generated by an airfoil section [37].

$$l(\psi) = \tfrac{1}{2}\rho U^2 c a_0 \left(\theta(\psi) + \phi\right); \quad d(\psi) = \tfrac{1}{2}\rho U^2 c \left(\delta_0 + \delta_2 C_T^2\right). \tag{4.1}$$

Here, U and ϕ are the speed and inclination of the wind relative to the airfoil in the plane of rotation, ρ is the density of air, θ is the pitch angle of the rotor blade element, c is the chord length of rotor blade, ψ is the instantaneous rotor position. In addition to these, a_0 represents the aerodynamic lift curve slope for the blade, C_T represents the thrust coefficient and the coefficients δ_0 and δ_2 represent the constant and variable aerodynamic drag coefficients. As shown in equation (4.1), the pitch angle of the rotor blade depends on the pilot inputs (and rotor position) and the angle of attack (θ-ϕ) of the rotor blade airfoils

depends on both pilot inputs and local wind conditions. Due to the high rotor speeds, ϕ has small values (close to zero). As a result, the vertical thrust generated by the airfoil section can be approximated to the generated lift-off force as follows:

$$f_z(\psi) = l(\psi)\cos(\phi) + d(\psi)\sin(\phi) \approx l(\psi). \tag{4.2}$$

4.1.1 Pilot Inputs

The rotor hub of the helicopter controls the pitch angle of the rotor blades by making use of a swash plate mechanism. The pilot's inputs for the rotor hub are composed of three elements viz. Collective (θ_0), Roll Cyclic (θ_c) and Pitch Cyclic (θ_s). The collective input results in an offset in the rotor pitch angles and is responsible for the overall hovering thrust generated by the helicopter. The cyclic input on the other hand makes the rotor pitch change cyclically with the rotor position and hence is responsible for thrust vectoring (tilting) and other desired maneuvering. In simplified form, the rotor pitch angle can be represented as follows in terms of collective and cyclic inputs and rotor position:

$$\theta(\psi) = \theta_0 + \theta_c \cos(\psi) + \theta_s \sin(\psi). \tag{4.3}$$

4.1.2 Aerodynamic Loading and Helicopter Dynamics

To estimate the aerodynamic loading on the main rotor blades, it can be assumed that the blades are composed of infinitesimally thin airfoil sections of chord length *c* and thickness dr_b (Fig. 4.1B). Wind vector experienced by any thin airfoil section depends on three parameters: rotor speed, fuselage rotation (rate), and local wind conditions (comprising of both rotor induced wakes and external wind turbulence). Because of near hover operation,

the effect of relative wind due to translational motion can be ignored. At any point in time, the relative wind velocity vector experienced by a rotor blade due to its motion alone can be expressed in terms of rotor speed and angular rates as follows:

$$u_{bh}(r_b,\psi) = \left[-r_b\Omega \mathrm{s}\psi \quad r_b\Omega \mathrm{c}\psi \quad -qr_b\,\mathrm{c}\psi + pr_b\,\mathrm{s}\psi\right]^T. \tag{4.4}$$

where, u_{bh} is the wind velocity vector relative to the helicopter blade (airfoil) element at a radial distance of r_b and angular location ψ in the helicopter's frame of reference (while rotating at speed Ω) and $\{p, q, r\}$ constitute the three angular rates of the helicopter fuselage. Additionally, the effect of yaw rate r is ignored here as $r<<\Omega$. By subtracting u_{bh} from external wind conditions, and pre-multiplying with the rotation matrix corresponding to the rotor position, the net wind experienced by the helicopter blade in element in the blade's frame of reference can be written as follows:

$$u_{wb}(r_b,\psi) = \begin{bmatrix} u_x \\ u_y \\ u_z \end{bmatrix}_{wb} = R_b^h \left(\begin{bmatrix} u_x \\ u_y \\ u_z \end{bmatrix}_{wh} + \begin{bmatrix} 0 \\ 0 \\ v \end{bmatrix}_{ih} - \begin{bmatrix} u_x \\ u_y \\ u_z \end{bmatrix}_{bh} \right) \tag{4.5}$$

where, u_{wb} is the net wind velocity vector relative to the helicopter blade (airfoil) element in the blade's frame of reference, R_b^h is the rotation matrix arising from rotor position ψ to convert wind estimates relative to blade elements from rotor hub to blade's frame of reference. The quantity $[u_x,u_y,u_z]^T_{wh}$ in equation (4.5) represents the external wind vector (spatially varying) in helicopter's frame of reference and v is helicopter induced rotor inflow (in helicopter's frame of reference) which depends on helicopter's mode of operation. For near hover conditions, the rotor inflow can assumed to be uniform over the rotor disk area [37].

Since the radial component of the wind does not contribute towards the thrust generation, only the $\{u_y,u_z\}_{wb}$ components contributed towards the blade aerodynamics. The aerodynamic loads generated by the rotor blade depend on the wind's 'angle of attack' of the relative with respect to the blade comprising of blade pitch angle θ, wind incidence angle ϕ. So, by substituting equation (4.5) in (4.1) and (4.2), the differential lift *dl* generated by an element can be expressed as follows:

$$dl(r_b,\psi) = \tfrac{1}{2}\rho\left(r_b\Omega\right)^2 ca_0\left(\theta+\phi\right)dr_b; \left| \begin{array}{c} \phi\left(r_b,\psi\right) = \tan^{-1}\left(u_z/u_y\right) \approx u_z/u_y \\ \left\{u_y,u_z\right\} = \left\{u_y,u_z\right\}_{wb} \end{array} \right. . \qquad (4.6)$$

These aerodynamic loads, when integrated over the length of the rotor blades, result in a net force and moment on helicopter. The proposed telemetry system focuses on the rotational effects of wind turbulence on the helicopter and thus only the moments $\{L,M,N\}$ acting on the helicopter are studied. Rigid body equations of rotational motion for a helicopter are given by the Newton-Euler equations shown below (4.7).

$$\begin{array}{l} I_{xx}\dot{p} = qr\left(I_{yy}-I_{zz}\right)+\left(L_{mr}+L_g\right) \\ I_{yy}\dot{q} = rp\left(I_{zz}-I_{xx}\right)+\left(M_{mr}+M_g\right) \\ I_{zz}\dot{r} = pq\left(I_{xx}-I_{yy}\right)+\left(-N_{mr}+N_{tr}\right) \end{array} . \qquad (4.7)$$

Here, $\{I_{xx},I_{yy},I_{zz}\}$ are the three moments of inertia of the helicopter respectively around *X* (right fin), *Y* (nose) and *Z* (up) axis. The subscripts *mr*, *tr* and *g* in the moment terms represent 'main rotor', 'tail rotor' and 'gravity', respectively. It is worth noting that the effect of the non-diagonal component (predominately I_{xz}) of the inertia has been neglected here as the values range from 7-30 times smaller than the diagonal entries.

The differential lift generated by the pilot controlled rotor pitch and wind flow pattern are the main and most prominent reason behind the helicopter's rotational dynamics. The

differential lift (4.6), when multiplied with radial distance from the rotor, can be integrated over the rotor length and position to obtain the net moment generated by one rotor blade (T) and should be multiplied by the number of blades (N_b) to obtain net rotor moment. The Pitch and Roll moment [37] from the main rotor can be obtained as follows.

$$L_{mr} = {N_b}/{2\pi} \int_{\psi=0}^{2\pi} T(\psi)\sin\psi d\psi;\ M_{mr} = {-N_b}/{2\pi} \int_{\psi=0}^{2\pi} T(\psi)\cos\psi d\psi;$$
$$T(\psi) = {1}/{2} C_A \rho \Omega^2 c \int_{r_b=0}^{R} r_b^3 \left(\theta(\psi) + \phi(\psi, r_b)\right) dr_b \quad . \qquad (4.8)$$

Here, the main rotor's yaw moment is ignored primarily because the pitch and roll moments are the more critical quantities from a naval safety perspective. In addition to this, the heading control system of the RC helicopter compensates for any aerodynamic disturbances along yaw axis through tail rotor.

In the moment equations of the helicopter (4.7, 4.8), other than the moments due to the gravity (L_g and M_g), all the moments depend on pilot inputs and wind conditions. The orientation of the helicopter along the pitch and roll axes create a 'pendulum type' restoring torque (4.9) which depends on the pitch and roll attitude angles of the helicopter.

$$L_{\mathrm{g}} = -rM_H g\sin(\theta); \quad M_{\mathrm{g}} = -rM_H g\sin(\phi). \qquad (4.9)$$

Here, r is the location of the center of mass with respect to the rotor hub. Figure 4.2 shows the general impact of aerodynamic thrust and attitude on angular rates changes (moment) of the helicopter. In addition, g is acceleration due to gravity and m_{A} is the mass of the helicopter.

The angular accelerations (4.7) of the helicopter can be written in terms of gravity and aerodynamic moments, which are non-linear functions of previous angular rates, air conditions, pilot inputs and helicopter attitude as follows:

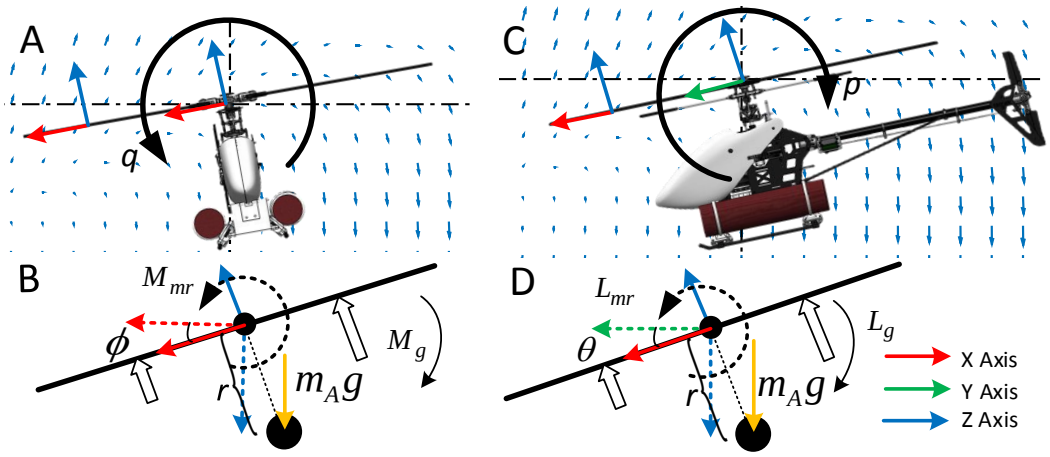

Figure 4.2: Factors affecting helicopter dynamics (angular rates) [79].

$$\begin{aligned} \dot{p}_t &= f\left(p_{t-1}, q_{t-1}, r_{t-1}, \mathrm{L_g}\left(\theta\right), \mathrm{L_{mr}}\left(\boldsymbol{P}, \boldsymbol{W}\right)\right) \\ \dot{q}_t &= g\left(p_{t-1}, q_{t-1}, r_{t-1}, M_{\mathrm{g}}\left(\phi\right), M_{\mathrm{mr}}\left(\boldsymbol{P}, \boldsymbol{W}\right)\right) \end{aligned}. \tag{4.10}$$

Here, **P** and **W** correspond to the set of pilot servo actuator inputs and wind model parameters respectively. The nonlinear functions *f*, *g* and the main rotor moment estimates, being too complicated to be solved analytically, are determined experimentally using machine learning algorithms. It is worth noting that the dynamics arising from the rotor blade flapping have been ignored in this analysis. The rotor blade flapping manifests itself as high-frequency fluctuations in the helicopter's angular acceleration measurement. It may be removed by applying a suitable low pass filter to the IMU reading. In addition, the net aerodynamic load on the rotor blades is an arithmetic sum of the components viz. pilot inputs and wind conditions. Since the pilot inputs, helicopter attitude, and previous angular rates can be measured and their aerodynamic loads can be modeled, any deviation in measured angular acceleration from the estimated values is essentially the result of wind disturbances and can be correlated to ship airwake. Ship airwake turbulence is the most predominant source of deviations.

4.2 Telemetry System Hardware

The proposed telemetry system comprises of two independent instrumentation sub-systems called the rover module and the base module. Figure 4.3 shows the prototypes of both modules.

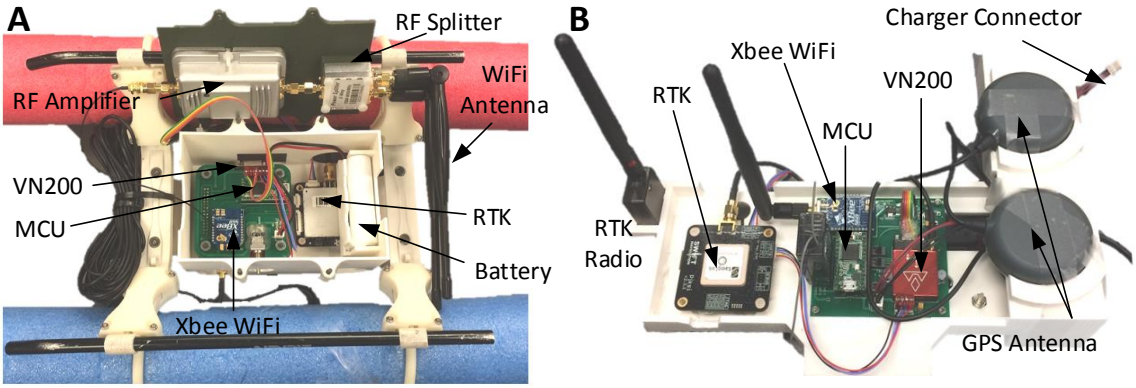

Figure 4.3: Telemetry System hardware setup: (A) Rover Module (Bottom view with cover removed); (B) Base module (Rearview without cover) [79].

These modules communicate to each other via a 3.5 Mbps long-range Wi-Fi network with an update rate of up to 150 Hz (~5 times the rotor speed). The Wi-Fi router uses two types of antennas, one an omnidirectional short-range rod antenna and the other a long-range directional Yagi antenna. In tandem, both antennas provide a long-range network coverage without any data loss. To estimate the ship airwake patterns, an RC helicopter retrofitted with the rover module is flown in the target area. The rover module then sends the helicopter's dynamics data to the base module over the Wi-Fi network. A computer connected to the base module records and processes the data then displays appropriate results/flight parameters on screen in the form of graphs and trajectories. Both modules in the proposed wireless telemetry system use aviation grade INS/IMU sensors to measure the position and dynamics of the helicopter and boat at a high rate (up to 800Hz).

4.2.1 Rover Module

The rover module is a battery powered instrumentation board that reads data from a VN200 INS development board (under the green interface board in Fig. 4.3A) and Piksi RTK, and sends the positioning data via XBee Wi-Fi module. The central processing unit of the rover module is an ARM Cortex M4 microcontroller that offers three UART serial ports. Figure 4.4A shows the electrical schematics of the rover module. One serial port is being used to connect the RTK to the system, while the second one is used to interface the Wi-Fi module. The third serial port is left unused for future upgrades. The rover module acquires helicopter flight parameters like position, attitude, speed, angular rates, and acceleration IMU packets with an update rate of 150 Hz from VN200 over SPI serial link.

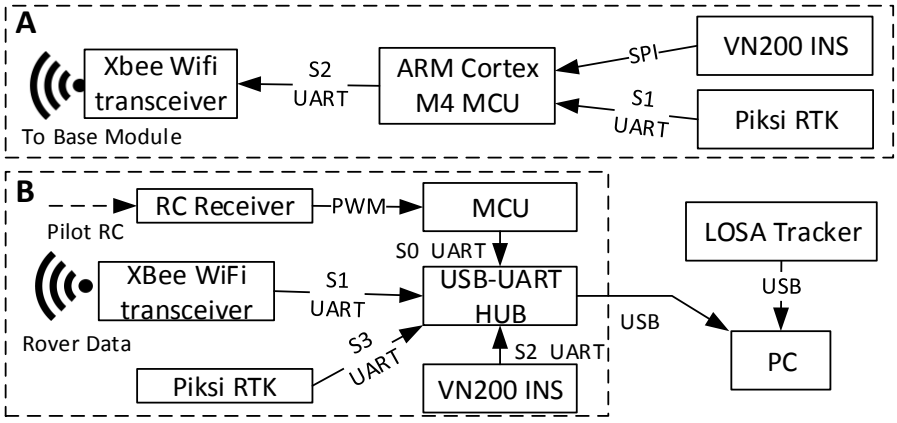

Figure 4.4: Electrical Schematics of: (A) Rover Module, and (B) Base Module [79].

The XBee modules with an omni-directional antenna had limited transmission/reception capability in open areas, the telemetry and thus required a custom RF communication system. Since the omnidirectional rod antennas have a cylindrical radiation pattern, two perpendicular 2.4 GHz rod antennas are used on the rover module to achieve transmission in all directions (Fig. 4.3A). To further improve the communication

range and network reliability, a 2W 2.4 GHz RF amplifier was used with the XBee Wi-Fi transceivers.

4.2.2 Base Module

The base module is an instrumentation board that receives pilot inputs (from a radio controller) and data from the rover module. Figure 4.3B shows the assembly of the base module on a 3D printed mount, which helps it fit rigidly on the ship during experiments. The core of this module is a USB to a quad-UART hub that connects up to four serial devices to a computer via USB port. An ARM Cortex M4 MCU board reads five channels of PWM inputs from an RC receiver and sends the pilot inputs to the PC via one of the serial ports on the hub.

Data from the rover module is received by the XBee Wi-Fi wirelessly and directly sent to the PC via serial port. Similarly, INS data from the VN200 sensor is sent to the PC via Serial port (S2). The fourth serial port (S3) is used (via a 4 pin connector) to interface the Piksi RTK to the system. The RTK system on the base module works in ‘base mode’ and sends the RTK correction data to the RTK on the rover module through a radio link. The baseline solution for the relative position is estimated on the RTK in the rover module and sent to the base module over the Wi-Fi link. Figure 4.4B shows the electrical schematics of the ship base module.

During measurement, the proposed telemetry system is mounted on a T-REX 600E PRO RC helicopter and flown in the lee of the superstructure of YP676 in a sweeping trajectory. The data is received on the base computer connected to the base modules using a custom-made GUI software in NI® LabVIEW™. The GUI allows the user to acquire and

record data in real-time without running into buffering issues due to its highly optimized serial virtual COM port and carefully programmed multi-threaded data handling capabilities. The GUI interfaces with the COM ports emulated by the base module and LOSA tracker [67] (a custom-made patent pending motion tracking device) to synchronize the data according to the associated time-stamps and store the data in text files for post processing. The relative position of the helicopter in the boat's frame of reference is obtained from the position and heading estimates from LOSA tracker/VN200 INS (on both modules).

4.3 System Training

As discussed in section 4.2, the helicopter's moment measurements (angular acceleration) can be split into three components viz. a gravity component, the cross product of the inertia component, and the main rotor component (comprising of effects of local wind conditions and pilot inputs). Although the ship airwake has both rotational and translational impacts (in all three axes) on helicopters, pitch and roll tilting are the most critical effects from a naval safety perspective. This research thus focuses on modeling the pitch and roll dynamics of the RC helicopter to extract wind turbulence conditions. Data for training the system to learn the helicopter's dynamics as a function of pilot inputs and state variables was collected by flying the instrumented helicopter in large indoor facilities. The helicopter was flown at an altitude of more than two rotor diameters (~2.5 m, to eliminate any rotor-ground effect) to perform a variety of high dynamics maneuvers and oscillatory tilting motion (at varying frequency) to create a versatile database of pilot input combinations and corresponding angular acceleration measurements.

4.3.1 Feed Forward Network

The proposed system uses a feedforward neural network to model the dynamics of the helicopter in absence of external disturbance (ship airwake). Neural networks are interconnected directed graphs (Fig. 4.5) comprising of cascaded MISO nodes known as neurons [80].

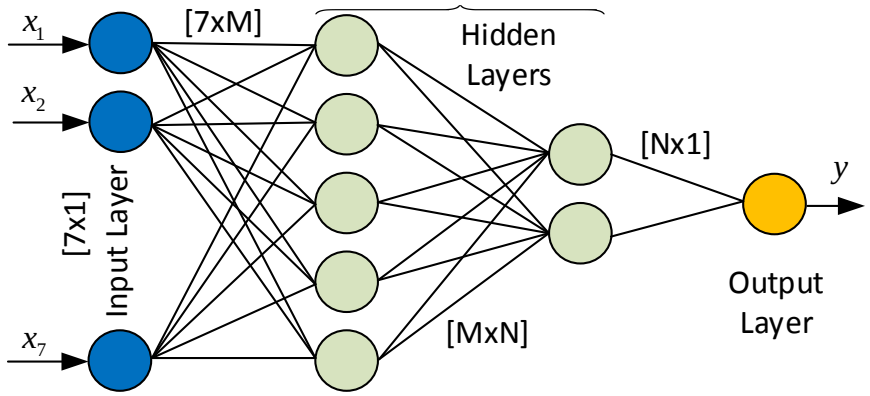

Figure 4.5: Proposed Network Topology [79].

The proposed network used a '*hyperbolic tangent*' sigmoid function and a '*purelin*' linear transfer function as objective functions for the neurons in hidden layer and output layer respectively. As shown in equation (4.10), the helicopter's angular acceleration measurements depend on seven inputs viz. three channels of angular rate readings, tilting angle (roll/pitch) and three swash plate pilot inputs. Thus, the input layer for the network consisted of 7 neurons. In addition, two separate hidden-layered feedforward networks were used for modeling the helicopter's angular acceleration along pitch and roll axis, the output layer consisted of a single neuron. For a network (Fig. 4.5) with $\{M, N\}$ being the

number of neurons in the hidden layers, the total number of variables to be optimized is ($7\times M+M\times N+N\times 1$) weights and ($M+N+1$) biases.

4.3.2 Particle Swarm Optimization

Backpropagation neural networks rely on gradient descent methods for training, which can converge at local error minima in training weight space. To overcome this limitation, the proposed system uses a particle swarm optimization (PSO) [81], [82] technique with 10-fold cross validation for training the neural network. PSO is a non-gradient stochastic sampling based optimization technique mimicking swarm intelligence of bird flocks with mathematical models.

PSO is typically used for global optimization in multidimensional search space where traditional neural networks are susceptible to converging at local extrema. Each particle involved in PSO is defined by a multidimensional vector in the search space with random initialization. In addition to this, all the particles retain a memory of their individual best performance and the global best performance (among all particles) over that course of training. With each iteration, the particles are evaluated according to their applications and the individual and global best particles are updated. In a swarm with X_{ib} and X_{gb} being individual particle's best performance and the global best particle respectively, the particle velocities (V) and position (X) for any particle are updated as follows:

$$X_N = X_{N-1} + V_N \Big| \quad V_N = mV_{N-1} + C_1 r_1 (X_{ib} - X_{N-1}) + C_2 r_2 (X_{gb} - X_{N-1}). \qquad (4.11)$$

Here, m (*0.2*) is the inertia coefficient, C_1, C_2 (*0.1, 0.2,* respectively) are exploitation coefficients and r_1, r_2 are exploration coefficient (random numbers generated between *0* and *1*). This process continues until the global best particle settles at the optimum position.

4.3.3 Training Neural Networks using PSO

The offline network training was done using custom-made MATLAB scripts, which not only performed data preprocessing, but also emulated neural network models by extracting weights and biases from individual particles in the swarm. To train the neural networks using PSO, a swarm of 5000 particles was randomly initialized, with the dimensionality of each particle decided by the topology of the network under consideration. The networks were trained multiple times (with different topology each time) with the number of neurons varied between 6 and 3 in both hidden layers. It was found that the networks with hidden layer topologies of $\{5, 2\}$ and $\{4, 3\}$ for roll and pitch acceleration prediction outperformed all other network topologies. All the particles in the swarm were initialized using random weights/biases. To keep the biases within the reach of the randomly assigned particles, the input vectors to the network models were normalized to zero mean and unit standard deviation. The global and individually best-performing particles were updated on the basis root mean squared error on the training data.

As mentioned before, 10-fold cross-validation was used for retrieving the optimum network during the training process. Ten percent of the training data was used for cross-validation and the network was said to be trained when the change in prediction error was less than (0.01 rad/s^2) and the prediction error on cross-validation data is lesser than or equal to that on training data. The network was trained on 30,800 training samples (~30% data) and tested on separate 73100 samples (~70% data). Figure 4.6 shows the progression of the training progress.

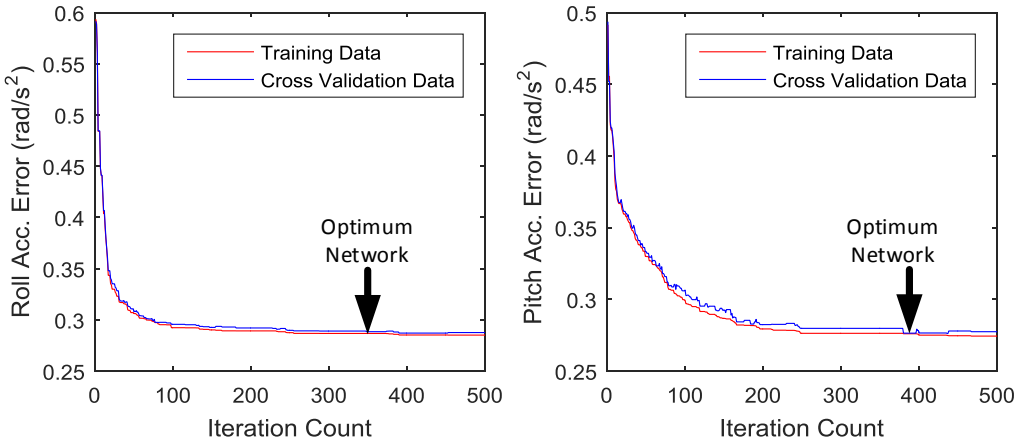

Figure 4.6: Mean Absolute Error v/s Iteration count for PSO-NN [79].

The mean absolute prediction error on the testing data set was found to be 0.2868 rad/s^2 and 0.2441 rad/s^2 for the roll pitch acceleration prediction network respectively.

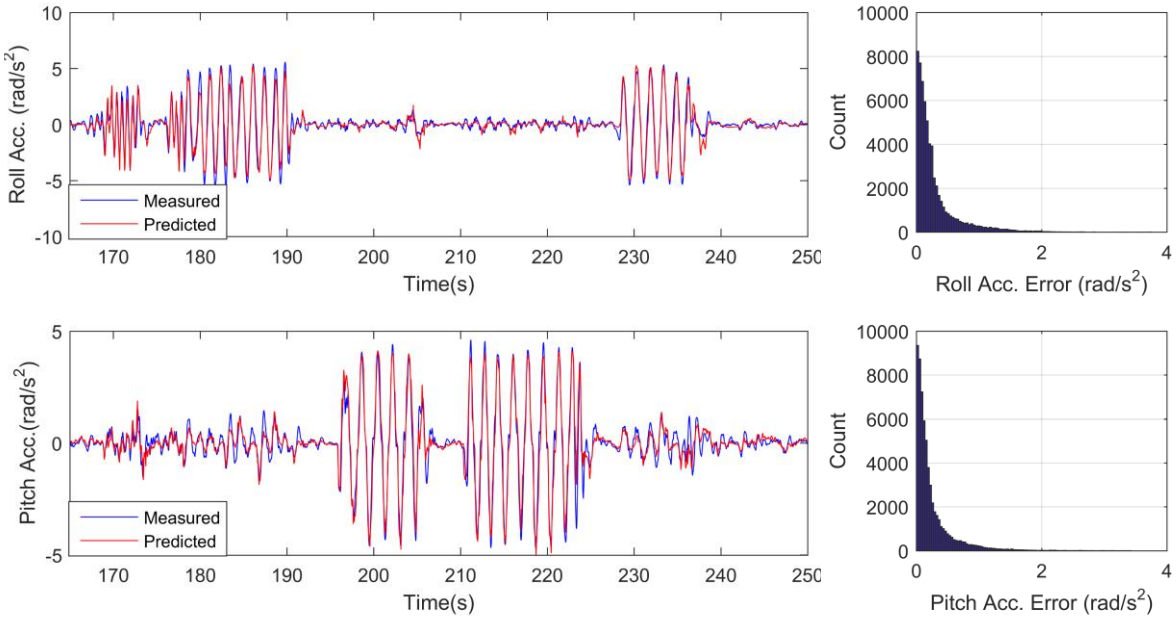

Figure 4.7: PSO-NN prediction results for pitch and roll accelerations and prediction error distribution [79].

Fig. 4.7 shows the angular acceleration prediction error on a sample test fight for the both networks. Fig. 4.7 also presents the prediction error distribution for the two networks in the form of histogram plots.

4.4 RC Helicopter as an Airwake Sensor

This section presents an assessment of the RC helicopter as a sensor to quantify ship airwake. As described in equations (4.8) and (4.10), the local wind conditions directly affect helicopter dynamics. Wind turbulence, which is stochastic in nature, results in stochastic dynamics of the helicopter. Thus, similar to the turbulence intensity, the effects of wind turbulence on the helicopter are obtained from the standard deviation of the angular acceleration residuals obtained from the trained PSO-NNs.

4.4.1 System Calibration

To determine correlation between the helicopter's dynamics and wind turbulence, another indoor experiment was performed where the proposed system was flown in the region with the airflow modeled. During the calibration experiment, the helicopter was gently maneuvered between the two wind circulation fans as shown in Fig. 3.13. The LOSA motion tracker [67] was retrofitted onto the helicopter's fuselage for tracking the position and attitude of the helicopter. Since the same tracker was used for the wind mapping experiment, the helicopter motion and wind conditions were measured in the same frame of reference and hence can be compared directly.

The angular acceleration estimates along the pitch and roll axes were converted from the helicopter's frame of reference to the tracker's (wind) frame of reference using attitude estimates obtained from the tracker. Then, for all the points on the helicopter trajectory, the norm of the local standard deviation of angular acceleration residuals (within a sample volume of 1.3 m×1.3 m×0.6 m) was computed. The local standard deviations of angular

acceleration residuals were then interpolated over the test volume at a 3D grid of 5cm and compared to the turbulence map. Figure 4.8 shows the spatial distribution of the angular acceleration residual deviation (subfigure A) and wind turbulence (subfigure B), in the form of 3D slice plots on planes X=0 m, Y=2.8 m and Z=1.8 m.

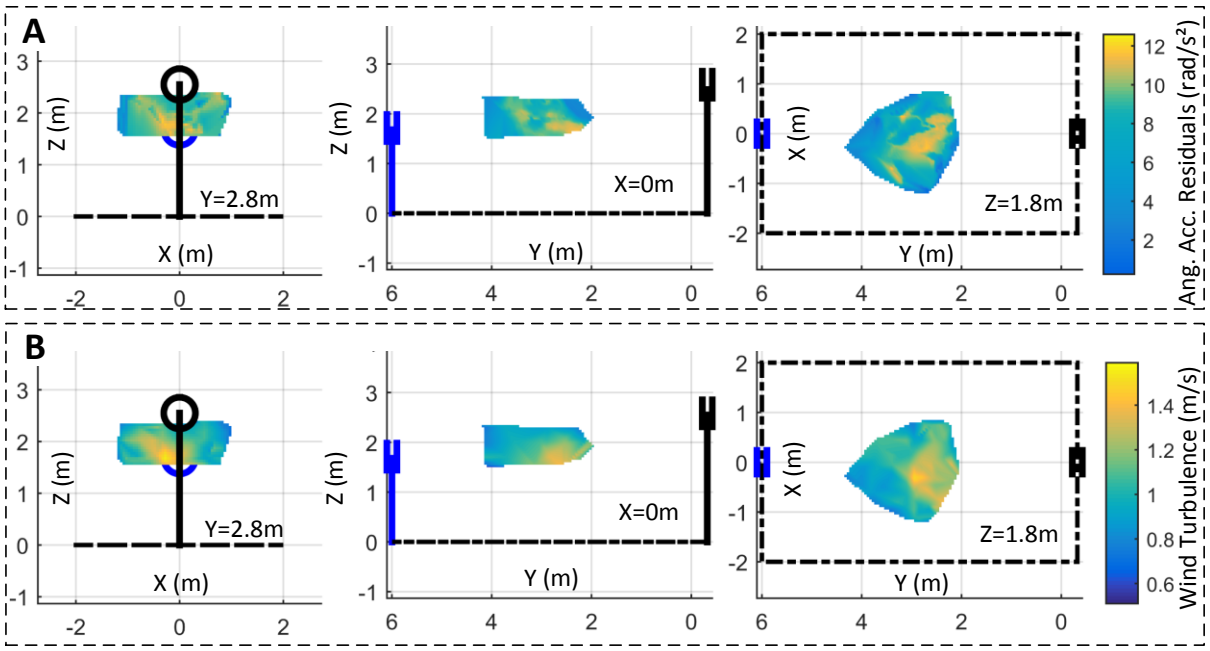

Figure 4.8: Helicopter response to wind turbulence, (A) Local (standard) deviation of the angular acceleration residuals; (B) Wind turbulence map [79].

For further analysis, the quantities from the two spatial distributions (shown in Fig. 4.8), were plotted and compared with each other (Fig. 4.9). Despite a high level of noise in the data, a positive correlation is clearly visible in the two quantities. As shown in equation (4.8), the moment exerted by the airwake is proportional to the instantaneous wind conditions (turbulence). Hence, after assuming a linear relationship, the scaling factor coefficient between the angular acceleration residuals and wind turbulence was estimated using linear curve fitting. Due to the high levels of noise, RANSAC [83] optimization was used to fit a linear relationship between the two quantities.

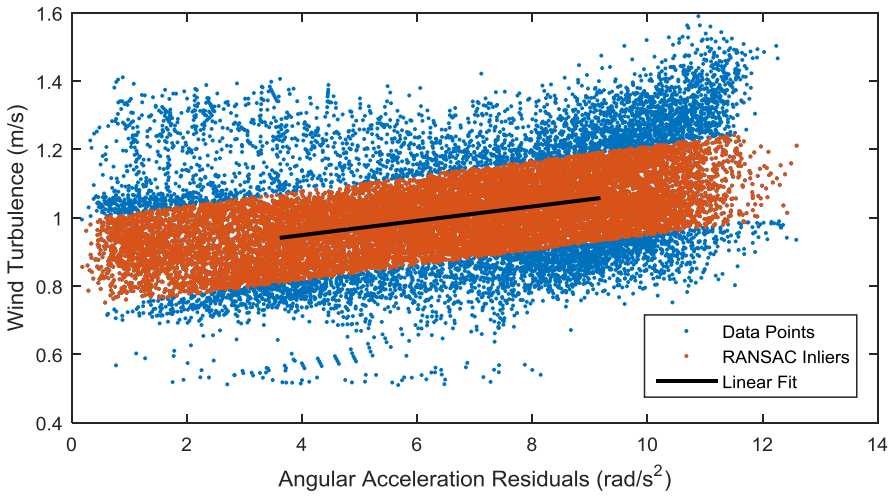

Figure 4.9: Calibration of angular acceleration residuals for estimation of wind turbulence [79].

Figure 4.9 shows the RANSAC inliers (in brown) and the linear fit line overlaid on the data points. The linear scaling coefficient for the angular acceleration residuals was obtained from the slope of the linear fit and was estimated to be 0.021 m·s/rad and an offset of 0.83m/s . The offset arising from the linear model for the wind turbulence measurements is primarily result of sampling in a finite volume due to the sensing range limitation of the motion tracking device. As this research focuses on estimations of relative distribution of the ship airwake, the linear offset has been ignored while estimating wind turbulence from angular acceleration residuals in outdoor experiments.

4.4.2 Frequency Response

RC helicopters, similar to any electromechanical system, have mass-inertia properties which make them act like a low pass filter in terms of responding to input excitations (airwake or pilot inputs). As shown in equation (4.8), both airwake condition and pilot inputs equally contribute towards the helicopter dynamics. Therefore, helicopter's

frequency response to ship airwake is expected to be similar to its response to the cyclic input. As it is challenging to generate variable wake frequencies from the indoor wind generation setup, the pilot-input frequency sweep data (recorded during network training experiment) was used for the frequency response analysis. MATLAB's '*tfestimate'* function was used for estimating the frequency response of the helicopter's angular acceleration (measured from the IMU) to cyclic swashplate pilot inputs in the Roll and the Pitch axes. As shown in Fig. 4.10, the system (T-Rex600E RC helicopter) behaves like a bandpass filter ~ (0Hz-2Hz) along both axes. The system's response for low frequency can be attributed to the fact that the helicopter tends to drift rather than tilt under low-frequency excitations.

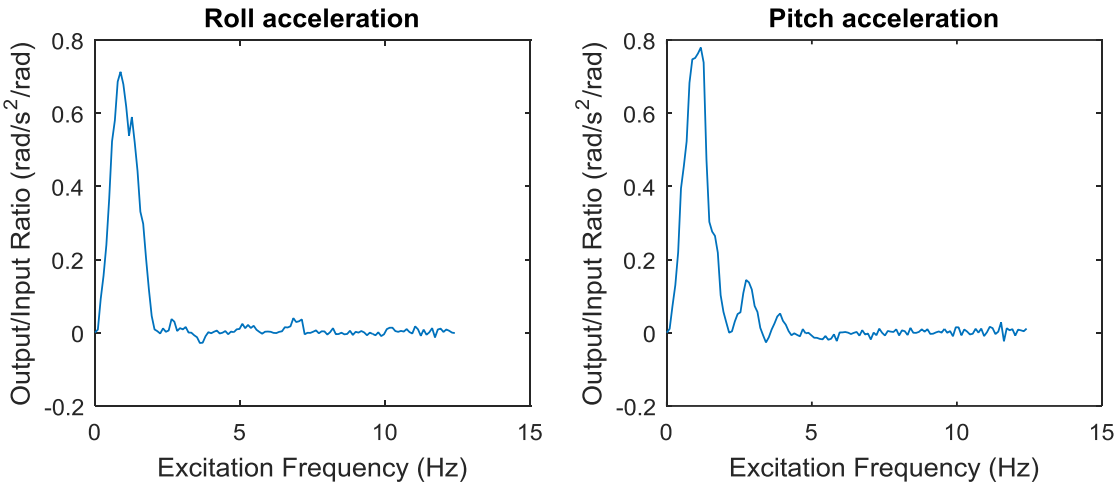

Figure 4.10: Frequency response of the helicopter's angular acceleration to cyclic (swash plate) rotor input.

4.4.3 Accuracy Assessment

As discussed in section 4.4.1, a linear model was used for the sensor calibrations. However, the applicability of the model needs to be assessed. The linear model was fitted to the standard deviation of the neural network residuals for the test dataset (with external

wind flow) to estimate the wind map. The predicted wind map was compared against the measured wind map (computed from indoor experiment). The **mean and standard deviation** of the measurement error were estimated to be **0.0318 m/s** and **0.0925 m/s**, respectively.

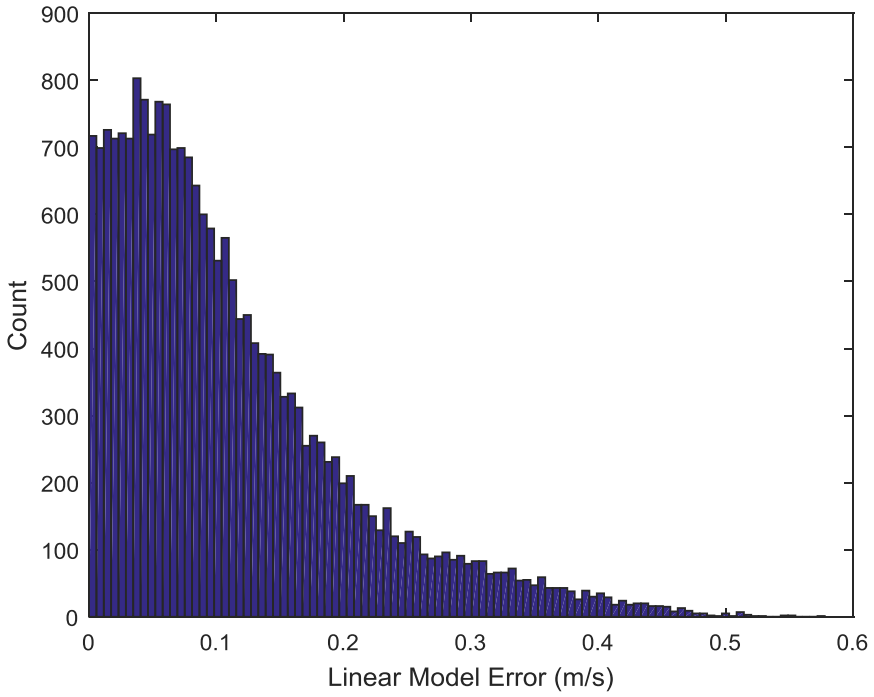

Figure 4.11: Proposed system's wind turbulence measurement error distribution.

Furthermore, Figure 4.11 shows the histogram of measurement error on the test dataset. The following reasons may be attributed to the lower sensor sensitivity:

- Interpolation errors in indoor wind map due to comparatively sparse sampling
- The limited field of view of the LOSA motion tracker introduces errors near the interpolation bounds, and
- Recirculation of rotor wakes and interaction with rotor inflow.

More details on these limitations and possible solutions are presented in *Chapter 6* of this dissertation under '*System Limitations and Future Work'* section.

4.5 Interaction between RC Helicopter and Ship Airwake

The airwake intensity derived from the dynamics of the RC helicopter arising from its interaction with airwake is then plotted on a trajectory of the helicopter relative to the ship. The YP676 is equipped with an anemometer array to help the craft master to maintain constant relative wind conditions. Figure 4.12 shows the telemetry system operating over the flight deck of a modified YP676 craft.

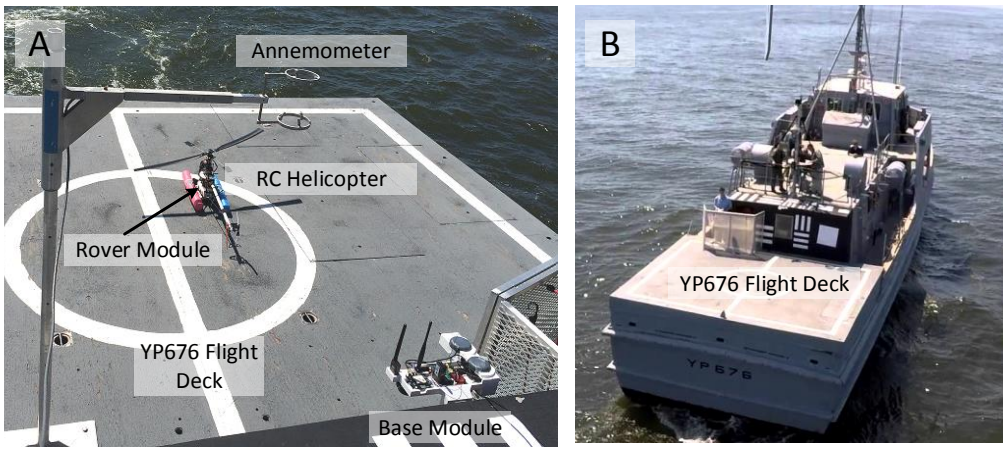

Figure 4.12: Outdoor testing: (A) Telemetry system operating from YP676 flight deck; (B) YP676 as seen from the RC helicopter [79] .

To map the ship airwake generated by YP676 naval training vessel, an RC helicopter with the proposed instrumentation system was flown in the lee of the vessel at near constant altitude during flight ops conducted in the Chesapeake Bay. During experiments, the craft-master (of the YP676) maintained a fixed relative wind speed of 6 knots (~3 m/s) with the help of vertically mounted acoustic anemometer array in the bow of the ship. The heading wind was maintained within a tolerance limit of ±1 knots and the wind heading direction was maintained within ± 5˚ tolerance limit. The experiments were conducted between sea

state 1 and 3; and the ship's pitch and roll never exceeded ± 3˚ to eliminate any chance of distortion in airwake patterns due to fluctuations in the ship attitude.

4.5.1 Airwake Flow Conditions

As presented by Brownell et al. in [19], [21], the YP676 craft experiencing a heading wind of 7 knots (3.6 m/s), generates a wake field of Reynold Number (*Re*) ~7.8×10^6. Based on the wind tunnel studies conducted on YP676 model in [21], the residence time for the recirculation zone was estimated to be approximately 1.5 s. This residence time falls within the frequency range that affects the RC helicopter the most. The *Re* estimates can be further used to estimate the approximate value of the *Strouhal Number* (*Sr*) for the flow field by assuming the ship shape to be equivalent to a cylinder as shown in [84]. With *Sr* ~ 0.25-0.26 the approximate value for the predominant *vortex shedding frequency* turns out to be *0.544 Hz* (for a characteristic length of 1.5 m, hanger height and wind speed over deck of 3.2 m/s).

CFD simulations were performed at USNA's advanced computing facility in Annapolis using Cobalt™ (a commercial parallel processing CFD software) on an unstructured tetrahedral grid of nearly 20 million tetrahedrons [3], [12], [20]. The CFD simulation study used Monotone Integrated Large Eddy Simulation (MILES), a laminar, time accurate flow model, to simulate 30 s of wind flow field generated by an YP676 model against a head wind of 7 knots (3.6 m/s). The study characterizes the ship airwake as reduction in steady-state flow content computed as the norm of the time-averaged wind velocity vectors in the simulated flow field. In contrast to the CFD analysis, the proposed system treats the norm

of the standard deviation of the wind velocity vector (obtained from residuals of helicopter acceleration) as the ship airwake (turbulence) intensity.

4.5.2 System Performance

To assess the system performance, the wind turbulence intensity was estimated from the localized standard deviation angular rate residuals and plotted on the trajectory of the RC helicopter relative to the ship, then compared against CFD results for qualitative comparison and analysis.

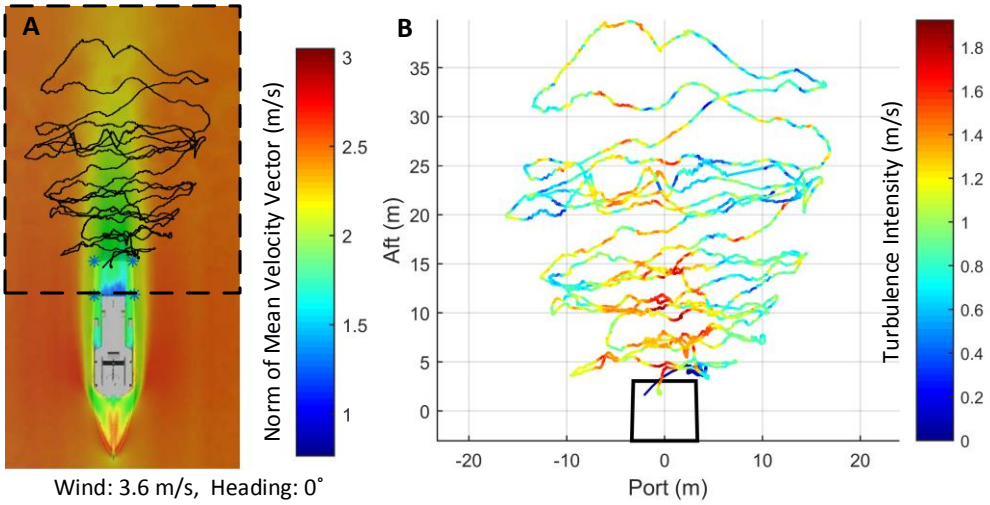

Figure 4.13: Ship airwake distribution: (A) CFD model simulation results with experimental trajectory overlaid; (B) Experimentally determined turbulence distribution [79].

Figure 4.13A shows simulated airwake pattern obtained in one of the previous studies [3] where the color represents the turbulence intensity represented as the norm of time averaged wind velocity vectors. The red color represents pure steady-state flow whereas the blue color represents the turbulent nature of the flow field. Figure 4.13B shows the experimentally derived ship airwake pattern on a helicopter trajectory determined from the calibrated local standard deviation of the angular acceleration residuals.

Although, the output from the proposed system and the CFD study represent different quantities, both physical quantities vary spatially with the change in local wind turbulence in an inverse manner. Due to inaccessibility to the raw CFD data, the turbulence intensity computations, as defined in the presented study, cannot be computed for point-to-point comparison with the experimental data. However, a qualitative comparison is still possible. Assuming equidistribution of kinetic energy throughout the simulated volume, the regions with higher turbulence are expected to have relatively lower values for the norm of the mean flow velocity vectors. Similarly, the regions with lower turbulence are expected to have higher values for the norm of the mean flow velocity vectors (closer to the input head wind speed). For further analysis of the airwake patterns, the experimentally obtained turbulence distribution was interpolated (using nearest neighbor interpolation followed by low pass filtering) over the area enclosed within the helicopter trajectory to generate a ship airwake map.

Figure 4.14 shows a comparison between the ship airwake patterns obtained from the CFD analysis and the proposed method. Figure 4.14A shows a cropped section of a simulated airwake pattern (presented in Fig. 4.13A) to compare against the experimentally obtained airwake map (Fig.4.14B). A high airwake zone is visible between 5 m and 10 m in the aft of the test vessel. In addition, both maps show decay in airwake intensity with distance from the flight deck of the vessel. As described previously, contrasting definitions of wind turbulence in both studies yield different metrics, displaying an inverse relationship, yet with the same units of wind speed.

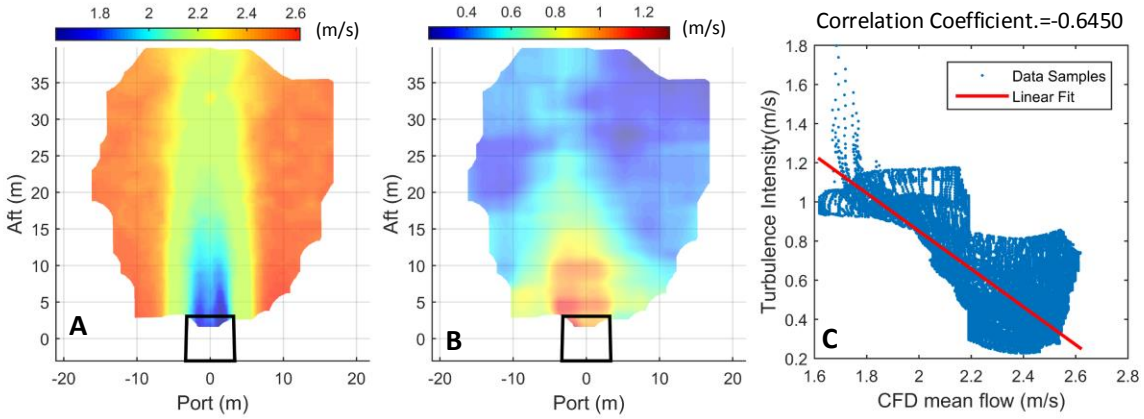

Figure 4.14: Turbulence map comparison: (A) CFD mean flow simulation results; (B) Experimental ship airwake map; (C) Turbulence cross-correlation [77].

The system currently relies on the rotational impact of wind turbulence on the RC helicopter to characterize airwake. By including the RC helicopter's linear drift in the system model, the steady-state flow component of the wind pattern can also be estimated using the proposed system. In addition, neural networks represent a black-box type modelling technique of a system that is susceptible to error if the input data differ too much from the training dataset. An analytical dynamic modelling (of the helicopter) based framework is under active development, which will use all measured helicopter states (including linear motion) to provide a better characterization of the ship airwake.

4.6 Direct Estimation of Wind conditions using Neural Network

Airwake aerodynamically affects RC helicopters the same way they would affect full-scale helicopters. Therefore, this study explored the applicability of neural networks in the direct estimation of local wind vorticities from helicopter dynamics [77]. Whereas previous work was focused on modelling RC helicopter's response to pilot inputs in absence of wind turbulence, this study models the same in a controlled wind environment.

4.6.1 Modeling Background

Helicopters are rotary wing aircraft, which use thrust vectoring for attitude control and maneuvering. The pilot inputs received by the RC helicopter's main rotor consist of three components: roll cyclic, pitch cyclic, and collective. The roll and pitch cyclic inputs result in a differential rotor pitch angle, which helps the helicopter to tilt and maneuver by creating differential thrust along the pitch and roll axes. Modelling the helicopter as a 3D rigid body, the Newton-Euler equations for the rotational motion of the helicopter can be represented by equation (4.7). The main rotor moment is primarily composed of two components: pilot inputs and wind conditions [37], [79]. If the helicopter's main rotor blade is assumed to be composed of infinitesimally thin airfoil elements (of thickness dr_b), then the differential liftoff (dl) generated by each element can be computed as follows:

$$\begin{aligned} dl(\psi) &= \tfrac{1}{2}\rho U^2 C_A c\left(\theta_b(\psi) - \eta\right) dr_b \\ \theta_b(\psi) &= \theta_0 + \theta_1\cos(\psi) + \theta_2\sin(\psi); \quad \eta = \tan^{-1}\frac{U_n}{U_t} \end{aligned} \tag{4.12}$$

where U_n and U_t are the normal and tangential components of the wind (U) relative to the moving rotor blade air foil in the rotor plane. From equation (4.12), it is clear that the thrust generated by the rotor blades depends on both the wind direction (η) and pilot inputs (θ_b).

Because of mechanical constraints in the swash plate, it is straightforward to model the rotor pitch angle; however modelling the wind angle is very difficult due to unpredictable wind flow in turbulent environments. The wind angle relative to the rotor blades is thus extracted from steady state flow conditions. The steady state external wind flow is modelled using a 12-parameter linear model as shown in equation (3.15) in Chapter 3. If the rotor blade airfoil section under consideration is at a radial distance r_b from the rotor hub assembly, then the wind relative to the airfoil due to its motion is $[0\ \Omega r_b\ 0]^{\mathrm{T}}$ and using this information, it is possible to estimate the wind relative to the blade. Here, effects of rotor flapping are ignored and it is assumed that the main rotor blades rotate in a fixed plane with respect to the helicopter's fuselage.

$$\begin{bmatrix} u_x \\ u_y \\ u_z \end{bmatrix}_{wb} = R_b^h \left(\begin{bmatrix} u_x \\ u_y \\ u_z \end{bmatrix}_{wh} - \begin{bmatrix} 0 \\ 0 \\ v \end{bmatrix}_{ih} - \begin{bmatrix} u_x \\ u_y \\ u_z \end{bmatrix}_{bh} \right); \begin{bmatrix} u_x \\ u_y \\ u_z \end{bmatrix}_{bh} = \begin{bmatrix} 0 \\ \Omega r_b \\ 0 \end{bmatrix} \tag{4.13}$$

By using equations (3.15) and (4.13), the wind inclination angle can be computed as follows:

$$\eta \approx \frac{d_z + a_z r_b \,\mathrm{c}\psi + b_z r_b \,\mathrm{s}\psi - v_{ih}}{-\Omega r_b + \mathrm{c}\psi\left(d_y + a_y r_b \,\mathrm{c}\psi + b_y r_b \,\mathrm{s}\psi\right) - \mathrm{s}\psi\left(d_x + a_x r_b \,\mathrm{c}\psi + b_x r_b \,\mathrm{s}\psi\right)} \tag{4.14}$$

where, v_{ih} is the induced rotor inflow, which is assumed to be constant for near-hover flight conditions. As the rotor speed term in the denominator is much larger than the remaining terms, the wind inclination angle (η) is proportional to a_z and b_z. The coefficients a_z and b_z

of the wind model represent vorticity in pitch and roll axis, respectively in the rotor plane. With η being proportional to rotor blade liftoff as shown in equation (4.14), it is also proportional to the main rotor moment along the roll and pitch axis as shown in equation (4.12) [79].

4.6.2 System Training and Results

As shown in the previous section, the wind conditions affect the helicopter's dynamic response to pilot input. Therefore, if the helicopter's dynamic model with state variables is known, it is possible to extract wind conditions from the helicopter's dynamics measurements. Similar to previous studies, this study also uses Back Propagation Neural Networks (BPNN) [80] to find the mapping between the helicopter dynamics variables and wind condition. As suggested in c (4.7), angular acceleration measurements of the helicopter depend on pilot inputs, wind conditions, angular rate measurement, and tilting angles (roll and pitch). Thus, the proposed system uses two BNNNs to predict wind vorticity (Roll/Pitch) from eight-dimensional input vectors consisting of three swash plate pilot inputs, three channel angular rates, the measured angular acceleration (Roll/Pitch) and the tilting angle (Roll/Pitch). For training and testing of the networks, the wind vorticity of the steady state flow field was obtained by fitting the data on the linear model shown in equation (3.15). The estimated wind vorticities in the inertial (LOSA tracker's) frame of reference were converted into the helicopter's frame of reference based on attitude estimates obtained from the LOSA tracker and fed to the neural network.

To model the helicopter's nonlinear dynamics, two 2-hidden layered BPNNs were trained. The BP Neural network topology was selected through trial and error. The system

was trained with the number of neurons in the hidden layers varied from 4 to 15. It was observed that the neural networks with hidden layer topology {8, 6} and {10, 5} deliver the best prediction accuracy. To prevent overtraining of the system, 10-fold cross validation [36] was used with the back propagation training algorithm. The networks were trained using around 7,100 data samples and tested on around 15,000 samples.

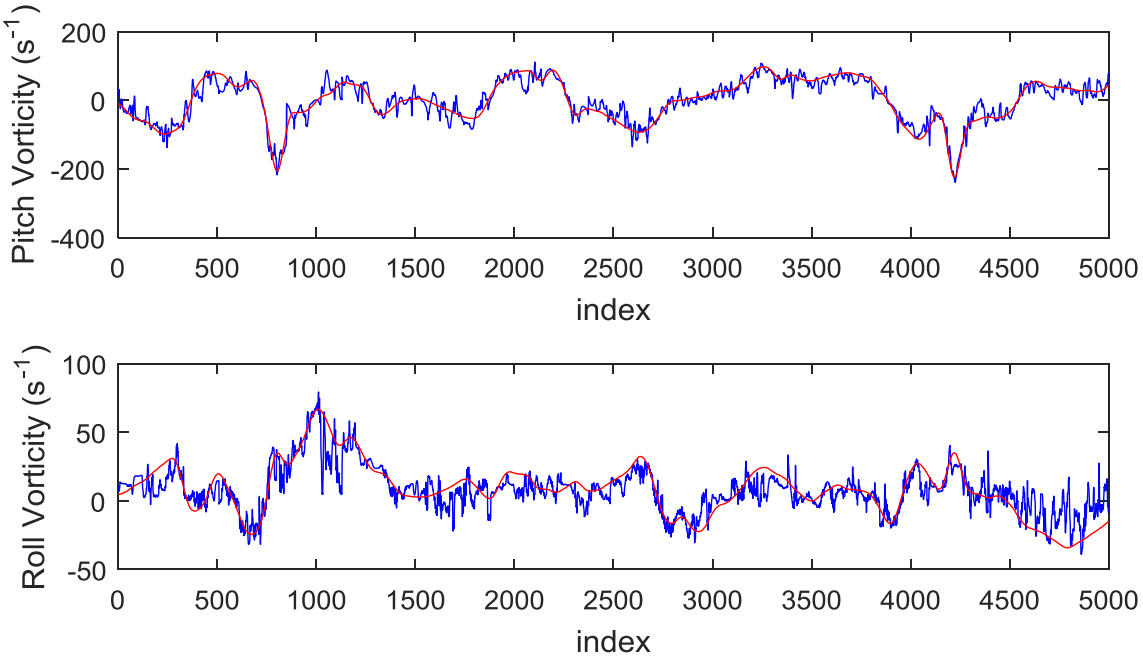

Figure 4.15: Neural Network prediction results (blue) with measured estimates (red) for wind vorticity [77].

Figure 4.15 shows the prediction results for the two neural networks predicting ambient wind vorticity on a subset of the test database. Figure 4.16 shows the histogram plot from the distribution of the absolute prediction error in wind vorticities.

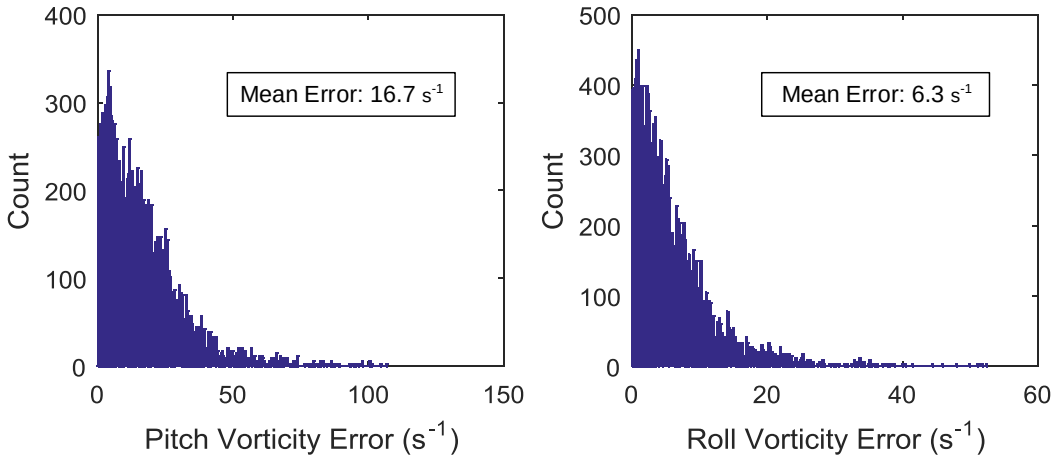

Figure 4.16: Neural Network output error distribution [77].

The trained networks were also tested by comparing the generated wind vorticity patterns against the measured steady state vorticity. Figure 4.17 shows qualitative comparison between the predicted vorticity pattern and the measured vorticity pattern in the form of 3D slice plots. High correlation is visible in wind vorticity distribution in the Z-Y plane (right column).

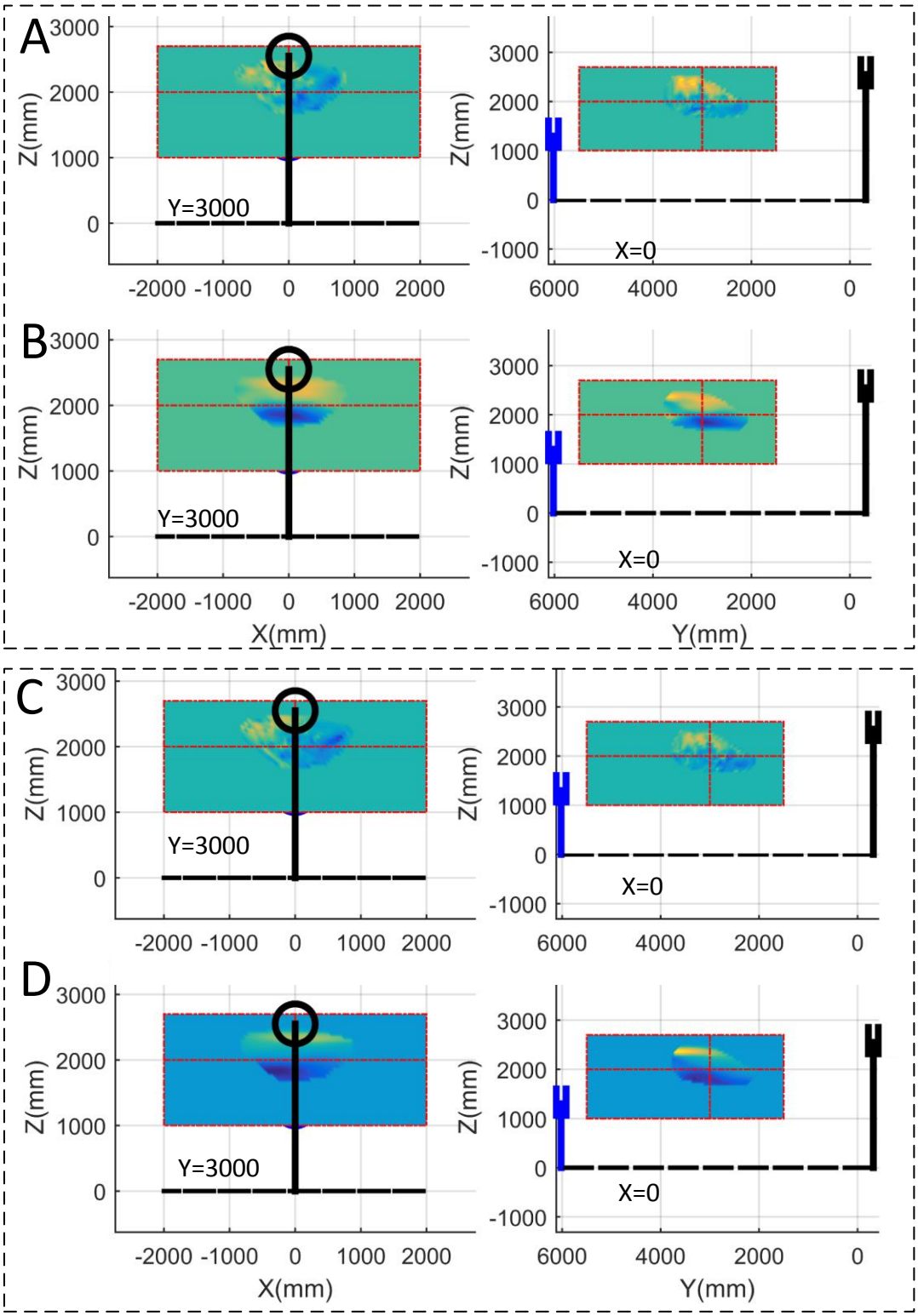

Figure 4.17: Wind vorticity patterns: (A) Predicted Vorticity along X axis; (B) Measured Vorticity along X axis; (C) Predicted Vorticity along Y axis; (D) Measured Vorticity along Y axis [77].

CHAPTER 5: WIND ESTIMATION USING RC HELCIOPTER AERODYNAMICS MODEL

This chapter investigates the applicability of an RC helicopter as a sensing platform for measuring local wind conditions. A sensing based non-linear helicopter model has been proposed in this chapter, which models the local wind conditions in addition to capturing essential helicopter state estimates such as fuselage dynamics, rotor inflow, blade flapping and lead lagging. Controlled turbulent wind conditions were artificially generated in an indoor facility then locally modeled using linear models. The critical aerodynamic parameters for the model were extracted using indoor calibration flights. A sensor fusion-based instrumentation system was developed to track helicopter dynamics and retrieve wind model parameters through anomalies in the helicopter dynamics estimates, using active particle filters. After collecting data from separate indoor experiments generated by flying the helicopter in still-air environments, the helicopter's dynamic model parameters were validated and optimized using Particle Swarm Optimization. This chapter presents a comparison between the estimated wind flow map and the experimentally measured wind flow pattern.

Machine learning is inherently a 'black box' type modeling technique where the reliability of the output depends on the diversity of the training data and complexity of the network topology (model). To overcome this limitation, this chapter presents a novel fully defined non-linear dynamic model-based approach to analyze the interaction of the helicopter with ship airwake. In contrast to existing helicopter dynamics studies, which use popular spatially invariant Control Equivalent Turbulence Input (CETI) model [85] for

characterizing wind turbulence, the presented approach analytically estimates the aerodynamics of the RC helicopter in varying wind conditions (represented using localized wind flow models). A Particle Swarm Optimization (PSO) based model calibration strategy for the proposed system is also presented in this dissertation through experimental flight testing. The system's capability to extract ship airwake is tested in an indoor calibration experiment where the helicopter was flown in artificially created wind turbulence.

5.1 Helicopter Dynamics and Airwake

5.1.1 Nonlinear Helicopter Flight Dynamics Model

As is widely known, helicopter dynamics are governed by aerodynamic loads that depend on both pilot control inputs and local wind flow. To estimate the local wind flow, it is necessary to model helicopter dynamics accurately. The test RC helicopter being lightweight permits the use of a simplified non-linear model for its dynamics assuming that the rotor blades and fuselage are rigid bodies. The proposed instrumentation system uses a nonlinear model to separate pilot induced dynamics from airwake dynamics. The helicopter model incorporates the critical components of a conventional helicopter such as a 2-blade articulated rotor, fuselage and tail rotor. To simplify the modelling process, linear incompressible aerodynamics along with helicopter symmetry, a constant helicopter mass/inertia matrix and rigid blades were assumed. Additionally, Pitt–Peters linear static inflow model [86], based on axial flow momentum theory, was used to model helicopter-induced wind inflow and extract out external wind conditions from the net wind experienced by the helicopter. Also, because for near-hover/slow descent mode of

operation, it has been assumed that the rotor wakes do not recirculate and affect the rotor inflow.

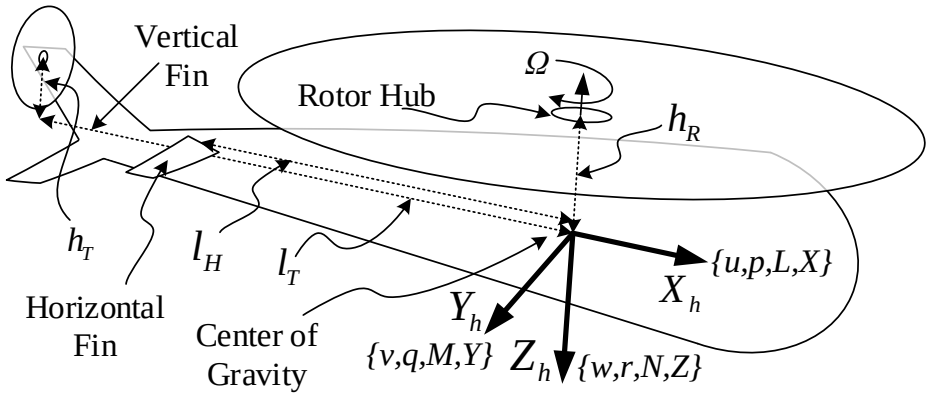

Figure 5.1: Coordinate system for the proposed helicopter model [87].

Fig. 5.1 shows the frame of reference assignment on the helicopter for the purpose dynamic modelling. The helicopter's non-linear dynamics can be written as (5.1) where $\boldsymbol{x}$ is the dynamics state vector, $\boldsymbol{w}$ is the local wind condition parameters and $\boldsymbol{u}$ is the pilot input vector.

$$
\begin{aligned}
&f(\boldsymbol{x}, \dot{\boldsymbol{x}}, \boldsymbol{w}, \boldsymbol{u}) = 0 \;\big|\; \{\boldsymbol{x} \in \mathbb{R}^{30},\ \boldsymbol{w} \in \mathbb{R}^{6}, \boldsymbol{u} \in \mathbb{R}^{4}\}; \text{where} \\
&\boldsymbol{x} = \left[\boldsymbol{B}\ \boldsymbol{F}\ \boldsymbol{L}\ \boldsymbol{I}\ \boldsymbol{P}\right]^{\mathrm{T}},\ \boldsymbol{u} = \left[\delta_0\ \delta_c\ \delta_s\ \delta_T\right]^{\mathrm{T}},\ \boldsymbol{w} = \left[v_x\ v_y\ v_z\ \omega_x\ \omega_y\ \omega_z\right]^{\mathrm{T}} \\
&\boldsymbol{B} = \left[u\ v\ w\ \theta\ \varphi\ \psi\ p\ q\ r\right]^{T},\ \boldsymbol{F} = \left[\beta_0\ \dot{\beta}_0\ \beta_c\ \dot{\beta}_c\ \beta_s\ \dot{\beta}_s\right]^{\mathrm{T}}, \\
&\boldsymbol{L} = \left[\zeta_0\ \dot{\zeta}_0\ \zeta_c\ \dot{\zeta}_c\ \zeta_s\ \dot{\zeta}_s\right]^{\mathrm{T}},\ \boldsymbol{I} = \left[\lambda_0\ \lambda_c\ \chi\right]^{\mathrm{T}},\ \boldsymbol{P} = \left[\theta_0\ \theta_c\ \dot{\theta}_c\ \theta_s\ \dot{\theta}_s\ \theta_T\right]^{\mathrm{T}}.
\end{aligned}
\tag{5.1}
$$

where, $\boldsymbol{B}$ represents the set of the helicopter body (fuselage) states consisting of translational velocity $\boldsymbol{v}_{\mathrm{H}}$ (u, v, w), roll-pitch-yaw attitude angle states (θ, φ, ψ) relative to the inertial North-East-Down frame of reference and angular rates $\boldsymbol{\omega}_{\mathrm{H}}$ along the roll- pitch-yaw axes (p, q, r). The sets $\boldsymbol{F}$, $\boldsymbol{L}$, $\boldsymbol{S}$, $\boldsymbol{I}$ and $\boldsymbol{P}$ represent dynamic states involving flapping angles, rotor Lead-Lag angles, stabilizer (flybar) see-saw flapping angles, static rotor

inflow field [86] and rotor blades pitch angles, respectively. The subscripts '*0*', '*c*', and '*s*' represent collective and two cyclic components of the various quantities when represented in multi-blade coordinate system [13], [37]. The pilot input $\boldsymbol{u}$ consists of collective (δ_0), two cyclic (δ_c, δ_s) and tail rotor (δ_T) as commanded blade pitch angles [88].

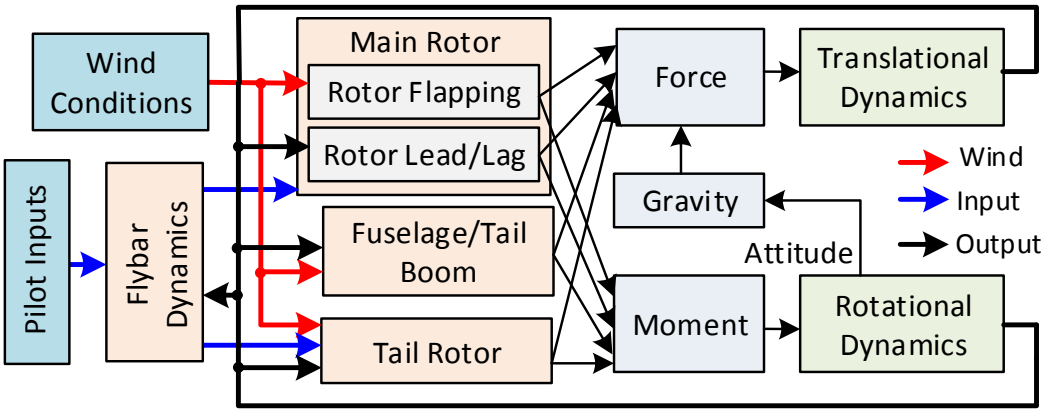

Figure 5.2: Helicopter dynamics models and subsystems [87].

Helicopters, being highly complex, feature nonlinear dynamics obtained from multiple interdependent subsystems. Figure 5.2 shows different constituent subsystems of the proposed helicopter dynamics model. Each subsystem is explained in subsequent sections. The fuselage of an RC helicopter, being small and lightweight, can be treated as a single rigid body to which the general rules of rigid body dynamics apply. Equation (5.2) shows the interdependence of fuselage states and the role of net external forces $\{X, Y, Z\}$ and moments $\{L, M, N\}$ acting along the helicopter's orthogonal axes (Fig. 5.1). Here, M_H, g and $I_{\{xx,yy,zz,xz\}}$ represent the mass of the helicopter, acceleration due to gravity and the components of the Inertia matrix of the helicopter, respectively.

$$\begin{array}{l|l} \dot{u} = a_x - g\sin\theta & a_x = -\left(wq - vr\right) + X / M_H \\ \dot{v} = a_y + g\cos\theta\sin\varphi & a_y = -\left(ur - wp\right) + Y / M_H \\ \dot{w} = a_z - g\cos\theta\cos\varphi & a_z = -\left(vp - uq\right) + Z / M_H \end{array}$$

$$\begin{array}{l|l} I_{xx}\dot{p} = qr(I_{yy} - I_{zz}) + I_{xz}(\dot{r} + pq) + L & \dot{\varphi} = p + (q\sin\varphi + r\cos\varphi)\tan\theta \\ I_{yy}\dot{q} = rp(I_{zz} - I_{xx}) + I_{xz}(r^2 - p^2) + M & \dot{\theta} = q\cos\varphi - r\sin\varphi \\ I_{zz}\dot{r} = pq(I_{xx} - I_{yy}) + I_{xz}(\dot{p} - qr) + N & \dot{\psi} = (q\sin\varphi + r\cos\varphi)\sec\theta \end{array} \quad . \tag{5.2}$$

This study models instantaneous local wind flow $\boldsymbol{w}_r$ at any general point location $\boldsymbol{r}$ relative to the main rotor hub in the helicopter's frame of reference using a 6-parameter linear model as shown below [77], [79]:

$$\boldsymbol{w}_r = \boldsymbol{\omega} \times \boldsymbol{r} + \boldsymbol{v} \quad \Big| \quad \boldsymbol{\omega} = \begin{bmatrix} \omega_x & \omega_y & \omega_z \end{bmatrix}^{\mathrm{T}}, \boldsymbol{v} = \begin{bmatrix} v_x & v_y & v_z \end{bmatrix}^{\mathrm{T}}. \tag{5.3}$$

where, × represent vector cross product, and $\boldsymbol{\omega}$ and $\boldsymbol{v}$ represent sets (vectors) of the wind vorticities and mean flow along the three axes of the helicopter's frame of reference. Helicopters generate control forces and moments through collective interaction of wind with its various body parts. The net helicopter forces and moments can be categorized on the basis of the part involved in the interaction with the wind:

$$\begin{aligned} \boldsymbol{F} &= \boldsymbol{F}_{mr} + \boldsymbol{F}_T + \boldsymbol{F}_f + \boldsymbol{F}_e = [X \quad Y \quad Z]^{\mathrm{T}} \\ \boldsymbol{M} &= \boldsymbol{M}_{mr} + \boldsymbol{M}_T + \boldsymbol{M}_f + \boldsymbol{M}_e = [L \quad M \quad N]^{\mathrm{T}} \end{aligned}. \tag{5.4}$$

where, $\boldsymbol{F}$ and $\boldsymbol{M}$ represent force and moment vectors and the subscripts *mr, tr, f* and *e* represent 'main rotor', 'tail rotor', 'fuselage' and 'empennage', respectively. In the process of estimation of the forces and moments, both local speed and direction play a significant role.

5.1.2 Main Rotor Dynamics

Out of all the control components, the effect of external wind conditions is most prominent in the main rotor dynamics. Aerodynamic loading generated by the main rotor depends on the tangential (in plane) and perpendicular (normal to rotor plane) components of the relative wind flow. This consists of components arising from both helicopter motions (including rotor inflow) and external wind flow (in absence of the helicopter). The internally generated perpendicular ($\bar{U}_{PH}$) and tangential ($\bar{U}_{TH}$) components of the wind flow relative to the moving rotor blades at a radial distance $\bar{r}_b$ (from rotor hub and normalized by rotor radius *R*) on azimuth position ψ_b can be represented as follows:

$$\begin{bmatrix} \bar{U}_{PH} \\ \bar{U}_{TH} \end{bmatrix} = \begin{bmatrix} -\lambda_0 - R\bar{r}_b\beta' + R\bar{r}_b p\sin\psi_b + (R\bar{r}_b q - \lambda_c)\cos\psi_b \\ R\bar{r}_b\Omega + R\bar{r}_b\zeta' \end{bmatrix} \frac{1}{R\Omega} \ . \tag{5.5}$$

Here, β' and ζ' are the partial derivatives of the rotor flapping angle β and lead lag angle ζ respectively, relative to the rotor azimuth position ψ_b and $\{\lambda_0, \lambda_c\}$ represent parameters of the linear static inflow model. Here, the effect of the yaw rate (r) of the helicopter has been ignored in the $\bar{U}_{TH}$ term as $r << \Omega$.

$$\begin{bmatrix} \bar{U}_{PW} \\ \bar{U}_{TW} \end{bmatrix} = \begin{bmatrix} -v_z - R\bar{r}_b\omega_y\cos\psi_b - R\bar{r}_b\omega_x\sin\psi_b \\ -v_y\cos\psi_b + v_x\sin\psi_b - R\bar{r}_b\omega_z \end{bmatrix} \frac{1}{R\Omega}. \tag{5.6}$$

The perpendicular ($\bar{U}_{PW}$) and tangential ($\bar{U}_{TW}$) components of the external wind flow relative to the rotor hub at a radial distance $\bar{r}_b$ and azimuth position ψ_b can be estimated using the linear wind model shown in equation (5.3). The net forces and moments exerted by the main rotor on the helicopter fuselage can be obtained by the integration of aerodynamic lift and drag forces along the blade length.

The lift and drag forces depend on the angle of attack of the net wind relative to the rotating blade. Equation (5.7) shows the normalized differential lift (F_L) and drag (F_D) forces as function of relative wind and main rotor pitch angle (θ_b). Here, δ, C_T and a_0 represent the aerodynamic drag coefficient, rotor thrust coefficient and lift curve slope for the main rotor blade, respectively. The aerodynamic coefficients were obtained using NACA0012 airfoil model [89].

$$\begin{aligned} & F_L = \bar{U}_T^2\theta_b + \bar{U}_T\bar{U}_P \quad \text{and} \quad F_D = \bar{U}_P^2 + \bar{U}_T\bar{U}_P\theta_b - \delta\bar{U}_T^2 / a_0 \\ & \text{where,} \bar{U}_T = \bar{U}_{TH} + \bar{U}_{TW},\ \bar{U}_P = \bar{U}_{PH} + \bar{U}_{PW} \text{ and } \delta = \delta_0 + \delta_2 C_T^2 \\ & \Rightarrow \begin{cases} F_L \approx (\bar{U}_{TH}^2 + 2\bar{U}_{TH}\bar{U}_{TW})\theta_b + \bar{U}_{TH}\bar{U}_{PH} + \bar{U}_{TH}\bar{U}_{PW} + \bar{U}_{PH}\bar{U}_{TW} \\ F_D \approx (\bar{U}_{TH}\bar{U}_{PH} + \bar{U}_{TH}\bar{U}_{PW} + \bar{U}_{PH}\bar{U}_{TW})\theta_b - \delta(\bar{U}_{TH}^2 + 2\bar{U}_{TH}\bar{U}_{TW}) / a_0 \end{cases}. \end{aligned} \tag{5.7}$$

5.1.2.1 Rotor Flapping

The vertical component of the spatially varying lift and drag forces acting on the rotor blades results in out of the plane flapping while rotating about the rotor hub. For simplified computations, the flapping has been modelled using center-spring equivalent model [13], [37] with the solution limited to first order harmonics in the multi-blade coordinate system. The flapping parameters {β_0, β_c, β_s} can be estimated by solving the blade flapping dynamics equation (5.8), with aerodynamic damping and non-uniform static rotor inflow conditions after higher order harmonics are ignored.

$$\begin{aligned} & \beta'' + \lambda_\beta^2\beta = 2\left(\bar{p}\cos\psi_b - \bar{q}\sin\psi_b\right) + \frac{\gamma}{2}\int_{\bar{r}_b=0}^{1}\left(F_L\bar{r}_b\right)d\bar{r}_b; \\ & \lambda_\beta^2 = 1 + K_\beta / \left(I_\beta\Omega^2\right); \gamma = \rho c a_0 R^4 / I_\beta; \bar{p} = p/\Omega; \bar{q} = q/\Omega \end{aligned} \tag{5.8}$$

where, γ is the lock number of the helicopter (ratio of aerodynamic to inertia forces acting on a rotor blade), ρ is the air density, I_β and K_β are the moment of inertia and equivalent spring stiffness constant of the rotor blades (determined experimentally), and λ_β is the

flapping frequency ratio. The flapping parameters obtained from (5.7) are a function of both helicopter states and the local wind condition parameters ***w***.

5.1.2.2 Rotor Lead-Lag

The in-plane lead-lag motion of the rotor blades occurs due to cyclic variations in the drag force acting on the rotor blades. Thus, similar to flapping, the rotor lag can also be modelled using center-spring equivalent model. The lead-lag parameters $\{\zeta_0, \zeta_c, \zeta_s\}$ can be estimated by solving the in-plane dynamics of the main rotor blades as shown in equation (5.9):

$$\zeta'' + \lambda_\zeta^2 \zeta = -\frac{1}{2}\gamma \int_{\bar{r}_b=0}^{1} \left(F_D \bar{r}_b\right) d\bar{r}_b; \quad \lambda_\zeta^2 = \frac{3}{2}\left(\frac{e_\zeta}{1-e_\zeta}\right) \tag{5.9}$$

where λ_ζ is the lead-lag frequency ratio and e_ζ is the normalized lag hinge offset. Aerodynamic damping arises from the presence of ζ' term in equation (5.5). Due to relatively low values of the flapping angles and flapping derivatives, the Coriolis coupling between the flap and lag motion has been ignored here.

5.1.2.3 Main Rotor Forces and Moments

The differential forces acting on the rotor blades can be integrated to estimate the net main rotor forces ($\boldsymbol{F}_{mr}$) acting on the helicopter's rotor hub as shown in (5.10):

$$\boldsymbol{F}_{mr} = \frac{\gamma I_\beta \Omega^2}{2R} \sum_{i=1}^{N_b} \begin{bmatrix} F_D \, \mathrm{s}\psi_{bi} + \beta_i F_L \, \mathrm{c}\psi_{bi} \\ F_D \, \mathrm{c}\psi_{bi} - \beta_i F_L \, \mathrm{s}\psi_{bi} \\ F_L \end{bmatrix}; \begin{cases} F_L = -\int_{\bar{r}_b=0}^{1} U_L d\bar{r}_b \\ F_D = -\int_{\bar{r}_b=0}^{1} U_D d\bar{r}_b \end{cases} \tag{5.10}$$

where *s* and *c* represent trigonometric sine and cosine functions, subscript *i* represents quantities corresponding to the i_{th} main rotor blade and N_b represents the number of the

blades in the rotor. Similar to the process of the flap and lag estimation, the integrals F_L and F_D are simplified by ignoring the third and higher order harmonics. The main rotor moments ($\boldsymbol{M}_{mr}$) can be obtained from center-spring equivalent flapping and lag estimates and main rotor forces as show below [37]:

$$\boldsymbol{M}_{mr} = -\frac{N_b}{2}\left[K_\beta\beta_s \;\; K_\beta\beta_c \;\; K_\zeta\zeta\right]^{\mathrm{T}} + \left[0 \; 0 \; -h_R\right]^{\mathrm{T}} \times \boldsymbol{F}_{mr}. \tag{5.11}$$

where h_R is the location of the rotor hub in the helicopter's frame of reference and $\times$ represents 3D vector cross product.

5.1.3 Tail Rotor Dynamics

The tail rotor blades of an RC helicopter, being smaller than the main rotor blades, do not produce sufficient thrust to generate significant modes in the blades or induce inflow. In such conditions, the external wind flow can be assumed uniform over the tail rotor disk area. Equation (5.12) shows the expression of the force $\boldsymbol{F}_T$ and moment $\boldsymbol{M}_T$ produced by the tail rotor (located at position $\boldsymbol{r}_T$) in the helicopter's frame of reference. Here, subscript T indicates quantitates related to the tail rotor and the variables ρ, R_T, Ω_T, c_T and a_{0T} represent the air density, rotor length, rotor speed, rotor blade chord length and lift curve slope, respectively.

$$\begin{aligned} &\boldsymbol{F}_T = \left[0 \;\; -Y_T \;\; 0\right]^{\mathrm{T}}, Y_T = \frac{\rho c_T a_{0T} R_T^3 \Omega_T^2 N_b}{2}\left(\frac{\theta_T}{3} + \frac{\left(\boldsymbol{v}_{T1}^2 + \boldsymbol{v}_{T3}^2\right)\theta_T}{2\Omega_T^2 R_T^2} + \frac{\boldsymbol{v}_{T2}}{2\Omega_T R_T}\right) \\ &\boldsymbol{M}_T = \boldsymbol{r}_T \times \boldsymbol{F}_T \\ &\begin{cases} \boldsymbol{v}_T = (\boldsymbol{\omega} - \boldsymbol{\omega}_H) \times \boldsymbol{r}_T + \boldsymbol{v} - \boldsymbol{v}_H \\ \boldsymbol{r}_T = \left[-l_T \;\; 0 \;\; -h_T\right]^{\mathrm{T}}, \Omega_T = N_T\Omega \end{cases}. \end{aligned} \tag{5.12}$$

5.1.4 Fuselage/Empennage Dynamics

The fuselage of the helicopter primarily contributes to the helicopter dynamics in the form of aerodynamic drag forces. The drag forces can be computed by modelling the shape of the helicopter fuselage as a tri-axial ellipsoid (Fig. 5.3). In a study conducted by J.A. DeMoss [90], aerodynamics drag coefficients of an ellipsoidal body were experimentally measured. As the helicopter's shape closely resembles an ellipsoid, the drag coefficients of the ellipsoid can be used for the helicopter's fuselage computation. The drag force ($\boldsymbol{F}_f$) experienced by the fuselage can be estimated as follows, where the terms C_X, C_Y and C_Z represent equivalent drag coefficients for winds flowing in the 3 axes of the helicopter.

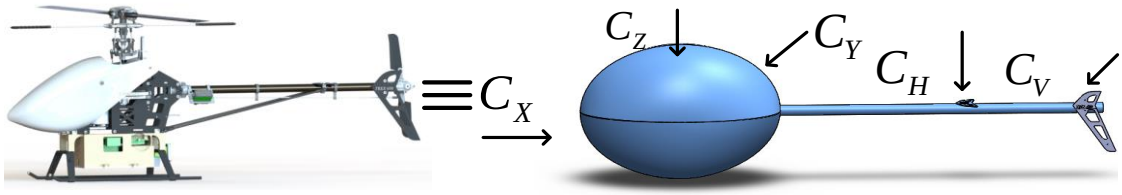

Figure 5.3: Helicopter's equivalent shape and aerodynamic drag surfaces [87].

$$\boldsymbol{F}_f = \frac{\rho}{6}\begin{bmatrix} C_X\left(u+v_x\right)^2 \\ C_Y\left(v+v_y\right)^2 \\ C_Z\left(w+v_z-v_d\right)^2 \end{bmatrix};\begin{cases} C_X = C_{DL}L_x^2 + C_{DF}F_x + C_{DW}W_x \\ C_Y = C_{DL}L_y^2 + C_{DF}F_y + C_{DW}W_y \\ C_Z = C_{DL}L_z^2 + C_{DF}F_z + C_{DW}W_z \\ v_d = \lambda_0 + \sqrt{T/(2\rho A_d)} \end{cases}. \tag{5.13}$$

Here, the terms C_{DL}, C_{DF} and C_{DW} represent drag coefficients for and corresponding to the ellipsoid length (L), face cross-section area (F) and wetting area (W) relative to the incident wind gust. As the shape of the helicopter is symmetric about the center, the moments arising from the unbalanced fuselage drag ($\boldsymbol{M}_f$) can be ignored.

In addition to the fuselage, the empennage (vertical and horizontal stabilizer fins) also result in significant drag forces on the helicopter (Fig. 5.3). The RC helicopter used in the presented study has one horizontal fin on the tail boom and one vertical fin besides the tail rotor. The net force and moments acting on the helicopter due to the drag forces on the stabilizer fins are computed as follows

$$\boldsymbol{F}_e = \frac{\rho}{2}\begin{bmatrix} 0 \\ C_{VF}(v + v_y - rl_T + \sqrt{F_T/(2\rho A_{dt})})^2 \\ C_{HF}(\lambda_0 + \sqrt{T/(2\rho A_d)} + w + v_z + ql_H)^2 \end{bmatrix} \qquad \boldsymbol{M}_e = \begin{bmatrix} 0 & F_{e3}l_H & -F_{e2}l_T \end{bmatrix}^T \tag{5.14}$$

where, C_{HF} and C_{VW} represent the vane drag coefficients for the horizontal and the vertical fins, respectively, (obtained using CFD studies done in Comsol™ software package) and A_{dT} represents the tail rotor disk area of the helicopter.

5.1.5 Stabilizer/Flybar Dynamics

RC helicopters are often equipped with a flybar assembly to improve the stability of the UAV. Flybar dynamics are necessary for modeling the helicopter's dynamics, as the actual cyclic main rotor pitch angles depend on the seesaw flapping angle of the flybar. Adapting the stabilizing bar model presented in [88], the main rotor blade pitch angles can be estimated as shown in equation (5.15)

$$\begin{bmatrix} \ddot{\theta}_c \\ \ddot{\theta}_s \end{bmatrix} + \boldsymbol{A}_{\dot{\theta}}\Omega\begin{bmatrix} \dot{\theta}_c \\ \dot{\theta}_s \end{bmatrix} + \boldsymbol{A}_{\theta}\Omega^2\begin{bmatrix} \theta_c \\ \theta_s \end{bmatrix} = \boldsymbol{B}_{\omega_H}\Omega^2\begin{bmatrix} \bar{p} \\ \bar{q} \end{bmatrix} + \boldsymbol{B}_{\delta}\Omega^2\begin{bmatrix} \delta_c \\ \delta_s \end{bmatrix} + \boldsymbol{B}_{\lambda}\Omega^2\begin{bmatrix} (\mu_z - \lambda_0) & \lambda_c & \lambda_s \end{bmatrix}^T$$

$$\text{where,} \quad \left\{ \boldsymbol{B}_{\lambda} = \frac{\gamma_f}{8c_2}\begin{bmatrix} 2\eta_2\mu & 0 & -1 \\ 0 & 1 & 0 \end{bmatrix}, \boldsymbol{A}_{\dot{\theta}} = \frac{1}{8}\begin{bmatrix} \gamma_f & 16 \\ -16 & \gamma_f \end{bmatrix}, \boldsymbol{A}_{\theta} = \frac{\gamma_f}{8}\begin{bmatrix} 0 & 1-\frac{1}{2}\eta_2\mu^2 \\ -1-\frac{1}{2}\eta_2\mu^2 & 0 \end{bmatrix}, \right. \tag{5.15}$$

$$\left. \boldsymbol{B}_{\omega_H} = \frac{1}{c_2}\begin{bmatrix} \gamma_f & -16 \\ -16 & \gamma_f \end{bmatrix} \text{ and } \boldsymbol{B}_{\delta} = \frac{\gamma_f}{8c_2}\begin{bmatrix} 0 & ((1+c_1)+\frac{1}{2}(3+c_1)\eta_2\mu^2) \\ -((1+c_1)+\frac{1}{2}(1-c_1)\eta_2\mu^2) & 0 \end{bmatrix} \right\}.$$

The terms Ω, μ, μ_z, and λ represent rotor speed, forward advance ratio, axial advance ratio and main rotor inflow, respectively. The independent variables γ_f, η_2, c_1 and c_2 represent flybar blade lock number, thrust scaling factor and fractional contribution of the swashplate and flybar tilting in main rotor blade pitch angles, respectively. The rotor blade pitch angles obtained through solving equation (5.15) can be fed into the helicopter forces/moment model as shown in equations (5.2) and (5.4) to estimate the pilot induced dynamics.

5.2 Telemetry System and Experimental Setup

The telemetry system hardware comprises of two independent instrumentation sub-systems called the rover module (retrofitted on an Align™ T-Rex 600E RC helicopter) and the base module [28], [77], [79]. Figure 5.4 shows the hardware setup of the proposed telemetry system.

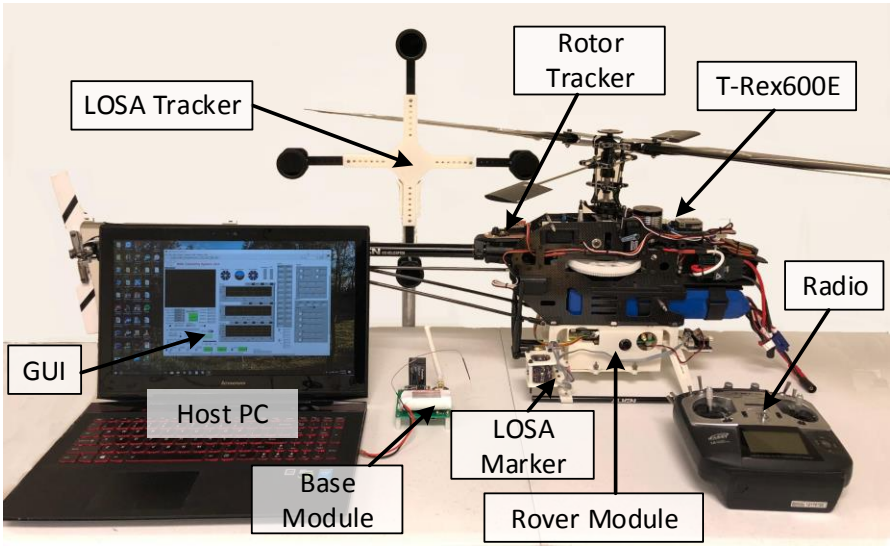

Figure 5.4: Hardware Setup for the presented study [87].

The instrumentation modules communicate with each other over a long-range Wi-Fi network with a data update rate of up to 150 Hz (~5 times the rotor speed). The proposed

telemetry system is supplemented by a custom made LOSA motion tracking system [67] (patent pending) for obtaining (mm level) accurate position and attitude estimates relative to the wind source at an update rate of >300 Hz. A host computer connected to the base module and the LOSA tracking system, acquires, processes and records the telemetry data and displays appropriate results/flight parameters on the screen in the form of graphs and trajectories using a custom-made LabVIEW™ GUI software.

Figure 5.5 shows the electrical schematic diagram of both the rover and base modules. Both modules are battery powered instrumentation board and includes common sensors such as VN200 INS and Piksi™ RTK with wireless communication capability through XBee™ Wi-Fi transceiver modules.

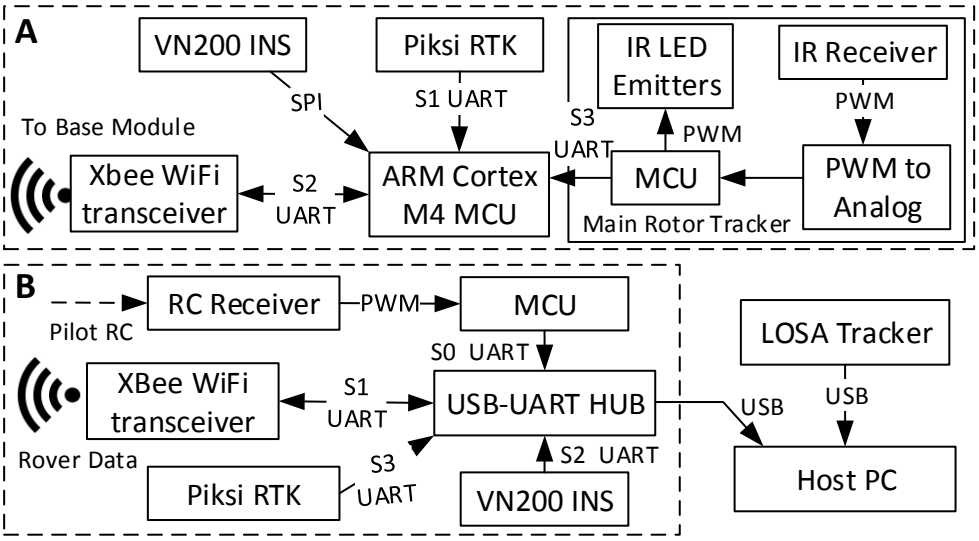

Figure 5.5: Electrical Schematics of (A) Rover Module; (B) Base Module [87].

The base module is equipped with an RC receiver (similar to one used for controlling the helicopter) to record the pilot inputs sent to pilots. The rover modules, in contrast, includes a rotor tracking subsystem to measure the main rotor speed during flying. The main rotor tracker (attached to the fuselage of the helicopter) beams high frequency IR

light pulses upwards (at the moving rotor blades) and detects IR reflections from the rotor blades using TSMP6000 IR sensor module [91]. The subsystem then measures the time interval between the two consecutive reflections to estimate the rotor speed. The rover module also measures the PWM commands from the heading stabilization system to the helicopter's tail actuator, and relays them to the base module along with the rest of the telemetry data.

The experimental setup as shown in Figure 5.6, primarily comprises of two large opposing (24-inch diameter) wind circulation fans (with adjustable speeds), separated at a fixed distance and at different heights and a T-Rex600E RC helicopter with rover module and LOSA tracker retrofitted on it. The host PC receives and records the time stamped helicopter dynamics, position estimates and pilot input data from the rover module, LOSA tracking system and the base module respectively for post processing.

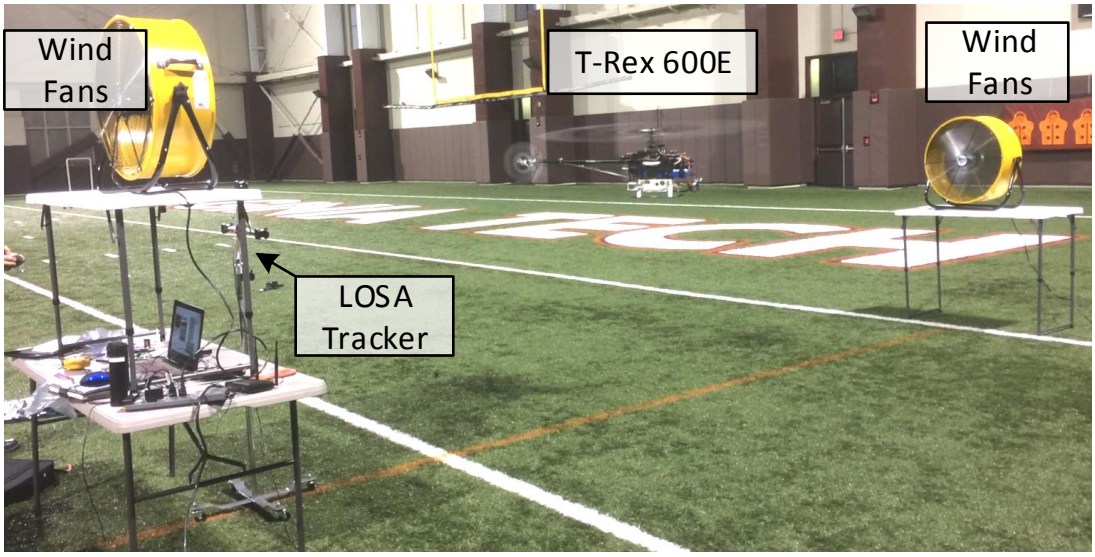

Figure 5.6: Experimental setup for the presented study [87].

5.3 Model Parameters Optimization

The dynamic model of the RC helicopter described in equations (5.1), (5.2) and (5.4) depends on nearly 37 different parameters in addition to the wind conditions and pilot inputs. These model parameters (as shown in Table 5.1) were obtained from different sources with different accuracy/confidence levels. In order to obtain an accurate dynamics model, the system model parameters were optimized using dynamics data collected during flying the instrumented helicopter in a large indoor facility (Fig. 5.6) with the wind circulation fans switched off. To collect the calibration data, the helicopter was flown at an altitude of more than two rotor diameters (~2.5 m, to eliminate any rotor-ground effect) to perform a variety of high dynamics maneuvers and oscillatory tilting motions (at varying frequency) to create a versatile database of pilot input combinations, along with other state variables and the corresponding angular/translational acceleration.

The proposed system uses Particle Swarm Optimization (PSO) for optimizing the model parameters. PSO is essentially a non-gradient stochastic sampling based on multidimensional global optimization techniques, mimicking the swarm intelligence of bird flocks [81]. Each particle involved in the PSO is defined by a vector in the multidimensional search space with random initialization. Each particle can be decoded into constituent model parameters and can be used to individually compute helicopter dynamics in the form of translational acceleration (including gravity, as measured by the accelerometer) and angular acceleration in the helicopter's local frame of reference. These acceleration estimates can be compared against acceleration measurements from the VN200 INS on the rover model to assess the accuracy of the model parameters (particle).

During the optimization process, the particles keep track of their best performance and the global best performance (among all particles) and update their current state by comparing against their individual and global best particles. To update any i^{th} particle (X^i) in the swarm, the velocity (V^i) estimates in the k^{th} iteration can be estimated from the individual particle's best performance (X_{ib}) and the global best particle (X_{gb}) respectively as follows:

$$\begin{aligned} X_k^i &= X_{k-1}^i + V_k^i \\ V_N^i &= mV_{k-1}^i + C_1 r_1 (X_{ib}^i - X_{k-1}^i) + C_2 r_2 (X_{gb} - X_{k-1}^i) \end{aligned} \tag{5.16}$$

where, m ($=0.1$) is the inertia coefficient, C_1, C_2 (each equal to 0.2) are exploitation coefficients and r_1, r_2 are exploration coefficient (random numbers generated between 0 and 1). To optimize the model parameters, a swarm of 2000 randomly initialized particles was deployed with an initial global best particle defined by the parameters given in the Table 5.1.

Table 5.1: Helicopter Model Initial Variables/Parameters

Var.	Value	Var.	Value	Var.	Val
R^*	0.673m	$M_H{}^*$	4.975 kg	Ω^*	163.3 rad/s
$I_{xx}{}^‡$	0.3173kg.m^2	$I_{yy}{}^‡$	1.483kg.m^2	$I_{zz}{}^‡$	1.539 kg.m^2
$I_{xz}{}^‡$	-0.0519 kg.m^2	K_β	84.2 Nm/rad	I_β	0.0184 kg.m^2
γ	4.486	e_ζ	0.1071	$a_0{}^†$	6.08 NmJ^{-1}rad^{-1}
$\delta_0{}^†$	7.3034×10^{-3}	$\delta_2{}^†$	4.912×10^{-3}	h_R	0.21m
$h_T{}^‡$	0.012m	$l_H{}^‡$	0.57m	$l_T{}^‡$	0.79m
ρ^*	1.225 kg/m^3	R_T	0.13m	$N_T{}^*$	3.85
$a_{0T}{}^†$	6.08 NmJ^{-1}rad^{-1}	c^*	0.054m	$c_T{}^*$	0.027m
$C_X{}^†$	6.26×10^{-2} Nms^2/kg	$C_Y{}^†$	0.1036 Nms^2/kg	$C_Z{}^†$	2.43×10^{-2} Nms^2/kg
$C_{HF}{}^‡$	7.598×10^{-4} Ns^2/m^2	$C_{VF}{}^‡$	2.2×10^{-3} Ns^2/m^2	A_d	1.4116 m^2
A_{dT}	3.3×10^{-2} m^2	g^*	9.798m/s^2	K_ζ	148.8 Nm/rad
c_1,$c_2{}^*$	0.733,0.663	$\eta_2{}^*$	4.3714	γ_f	0.8002

*Direct measurement/Constant. †From cited studies. ‡From CAD/CFD models.

As some parameters of the RC helicopter model were known with absolute certainty (constants/experimentally measured), particle velocity corresponding to such parameters were ignored and set to zero. Table 5.2 shows the final model parameters obtained after PSO optimization procedure.

Table 5.2: Helicopter Model Variables/Parameters after Optimization

Var.	Value	Var.	Value	Var.	Val
R^*	0.6645m	$M_H{}^*$	4.975 kg	Ω^*	163.3 rad/s
I_{xx}	0.3834kg.m^2	I_{yy}	1.3147kg.m^2	I_{zz}	1.44 kg.m^2
I_{xz}	-0.0521 kg.m^2	K_β	297.16 Nm/rad	I_β	0.0193 kg.m^2
γ	3.3933	e_ζ	0.1091	$a_0{}^\dagger$	2.8739 NmJ^{-1}rad^{-1}
δ_0	0.0702	δ_2	4.646×10^{-3}	h_R	0.2049m
$h_T{}^\ddagger$	0.012m	$l_H{}^\ddagger$	0.5567m	$l_T{}^\ddagger$	0.7978m
ρ^*	1.2249 kg/m^3	R_T	0.1303m	$N_T{}^*$	3.85
a_{0T}	7.09 NmJ^{-1}rad^{-1}	c^*	0.054m	$c_T{}^*$	0.027m
C_X	5.76×10^{-2} Nms^2/kg	C_Y	0.1002 Nms^2/kg	C_Z	2.57×10^{-2} Nms^2/kg
C_{HF}	8.14×10^{-4} Ns^2/m^2	C_{VF}	2.1×10^{-3} Ns^2/m^2	A_d	1.4134m^2
A_{dT}	3.331×10^{-2} m^2	g^*	9.798m/s^2	K_ζ	240.4 Nm/rad
c_1,c_2	0.74,0.52	η_2	5.124	γ_f	0.7868

*Direct measurement/Constant.

Figure 5.7 shows the swarm optimization results on a calibration flight of ~62000 samples (in external wind free environment) over 500 iterations. Figure 5.7A shows asymptotic decrease in the norm of modeling error of the helicopter acceleration (both translational and rotational combined) with PSO iterations. With an RMS error value of 0.848 (units ignored), the performance of the model obtained from the 'global best' swarm particle is presented in the Fig. 5.7B in the form of an error histogram for the prediction of all the 6 acceleration channels on log scale.

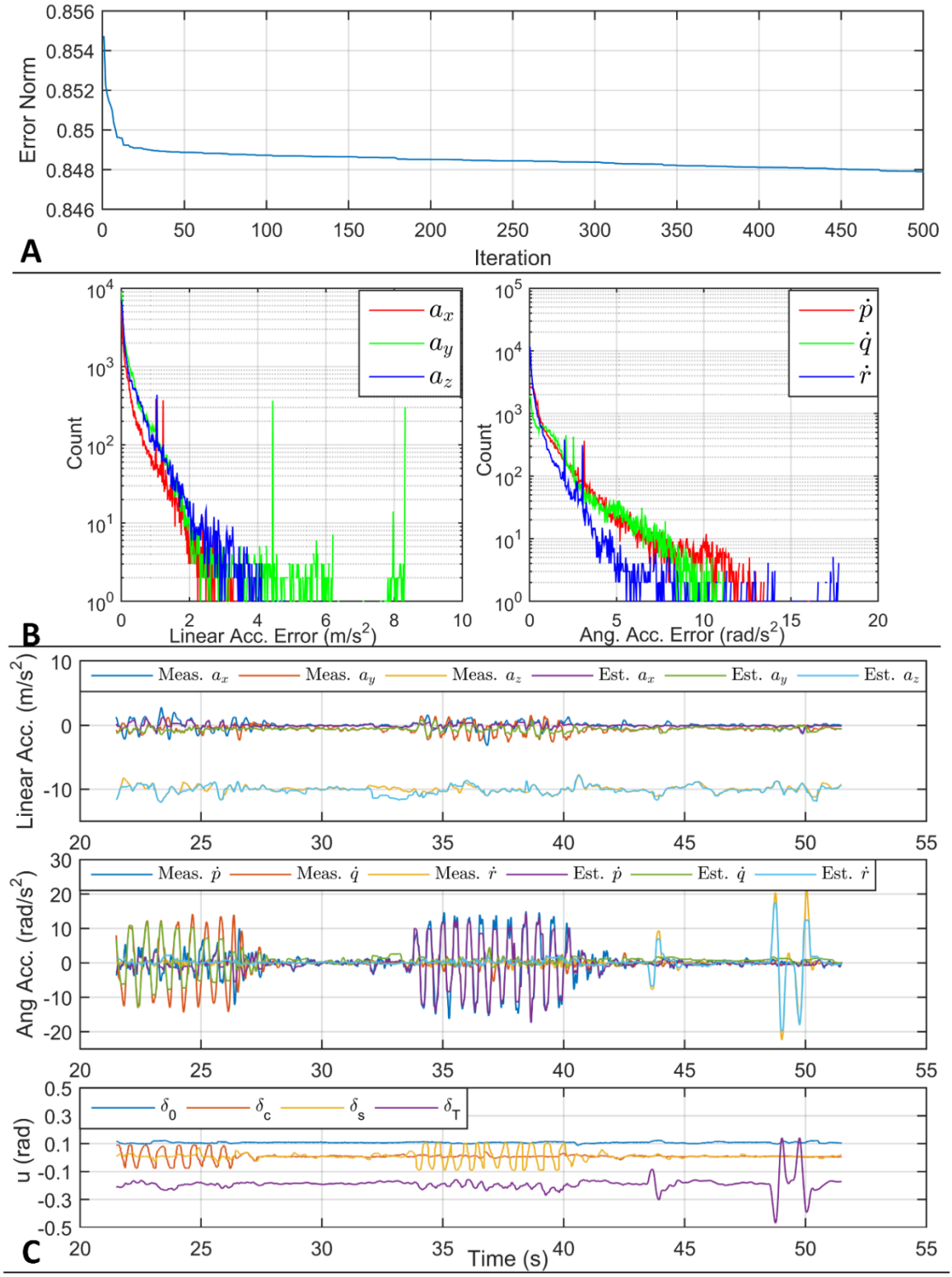

Figure 5.7: Model optimization results: (A) Modelling Error Progression; (B) Model Error Distribution; (C) Model output along with pilot inputs (u) [87].

Furthermore, the acceleration estimates obtained from the optimized model were plotted against the IMU measurements and pilot inputs in Fig. 5.7C. A very good correlation was observed between the estimated and measured accelerations (both linear and rotational).

5.4 Wind Estimation and Results

To test the capability of the proposed system, the helicopter was flown in an environment with known wind conditions (Fig. 5.6). Turbulent wind flow field was generated by the two opposing wind circulation fans. The wind flow pattern was measured using the setup presented in [77], [79] using a three-axis Young™ Ultrasonic Anemometer (Model 81000) [78] mounted on a pole with adjustable height (Fig. 5.8A). The LOSA motion tracking system [67] was used to localize wind measurements and map the wind field in the global (wind source) frame of reference. Attitude and velocity estimates from the motion tracker were further used to adjust for the motion of the anemometer in the wind readings. As discussed in [79], the wind measurements were taken at (~130) different locations and for at least 10 s of duration. At each location, the mean wind vectors and turbulence intensity (defined as the norm of the standard deviation of the wind) vectors were recorded. Figure 5.8B shows the wind flow field (interpolated at a grid of size 5 cm) obtained by using the setup shown in Fig. 5.8A. To characterize the wind flow for further analysis, the 6 parameter linear model $\boldsymbol{w}$ (equation 5.3) was fitted on the local wind flow field in a volume of 1.3 m×1.3 m×0.6 m (equivalent to helicopter's size) using the least squares method.

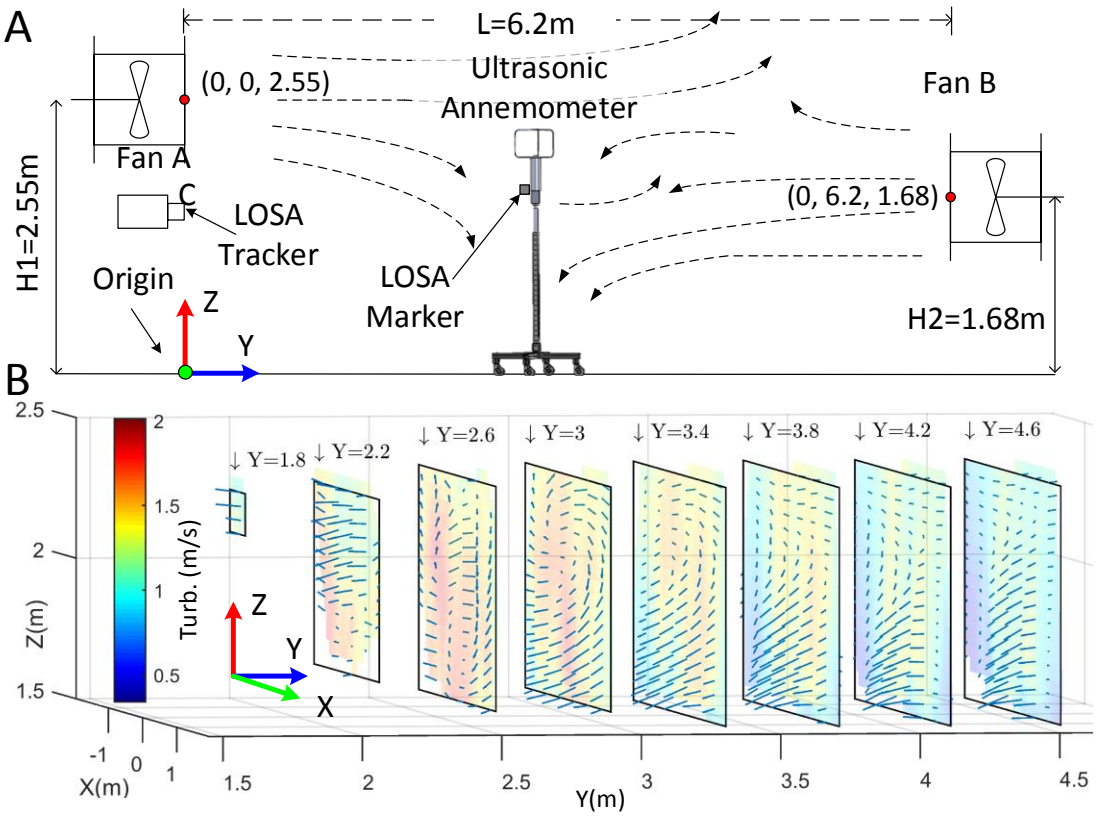

Figure 5.8: Wind Mapping Experiment: (A) Experiment setup; (B) Wind Map [87].

5.4.1 Active Particle Filters

Active particle filters (APFs) are model based tracking algorithms using sequential Monte Carlo methods for representation of probability densities [92]. APF is a type of recursive filter which use simulated samples in the search state space (particles) with associated weights to represent the probability distribution of the random variable. The system is solved for each particle to obtain its fitness value (weighting coefficient). Let χ be a set of N weighted samples, then for each iteration the Probability Distribution Function of random variable x can be estimated using equation (5.17) where, δ is the Delta-Dirac function for sample $\boldsymbol{x}_j$.

$$\begin{aligned} \bar{\boldsymbol{x}} &= E(\boldsymbol{\chi}) = \sum_j \boldsymbol{x}_j p\left(\boldsymbol{x}_j\right) \text{ where } \boldsymbol{\chi} = \{\boldsymbol{x}_j, w_j\}_{j=1..N} \\ w_j &= \exp\left(-\tfrac{1}{\sigma}\|\boldsymbol{z} - \hat{\boldsymbol{z}}\|\right) \text{ and } p(x) = \sum_j w_j . \delta_{x_j}(x) \end{aligned} . \quad (5.17)$$

Here w_j represents the fitness value (weighting coefficient) of the j^{th} particle computed from the measured states ($\boldsymbol{z}$) and expected values of the measured states ($\hat{\boldsymbol{z}}$, using the system model) with σ being the error sensitivity factor. The expected value to the random state variable ($\bar{\boldsymbol{x}}$) is estimated from the expected value of particles of the value of the probability distribution function $p(\boldsymbol{x})$. After each iteration, the particles are updated using $p(\boldsymbol{x})$ through Monte-Carlo regularization method.

5.4.2 Wind Estimation using APF

The APFs are an ideal tool for the estimation of nonlinear systems without requiring prior knowledge of the states to be estimated. Since the turbulent wind flow is a highly stochastic quantity to model statistically, the proposed system uses APFs for the estimation of wind characterization parameters ($\boldsymbol{w}$). To estimate the wind conditions an APF with a population of 2000 (6-dimentional) particles was randomly initialized to scan the search space. Each dimension of the particle was normalized to a value between 0 and 1 on the basis of the extreme values to the wind parameters measured experimentally. For each particle, the linear $\{a_x, a_y, a_z\}$ and rotational $\{\dot{p}, \dot{q}, \dot{r}\}$ accelerations were estimated using the pilot inputs and state measurements and wind condition (from the concerned particles) with the helicopter's model presented in section 5.1. The estimated accelerations ($\hat{\boldsymbol{z}}$) are compared against the acceleration measured using the IMU ($\boldsymbol{z}$) to identify the 'well performing' particle and estimate the wind condition parameters from the expected value of $p(x)$ over particle populations as shown in equation (5.17). For the subsequent iterations,

the ‘fittest’ particles are randomly selecting the particles using the roulette wheel method. This process continues recursively for all input samples.

5.4.3 Results and Discussions

The 6-D wind parameters obtained using the APFs are essentially the result of the dynamics assessment of the helicopter and hence are represented in the helicopter’s local frame of reference. To obtain external wind flow parameters, the wind parameters were converted from the local frame to the inertial frame of reference using the attitude estimates obtained from the LOSA tracker.

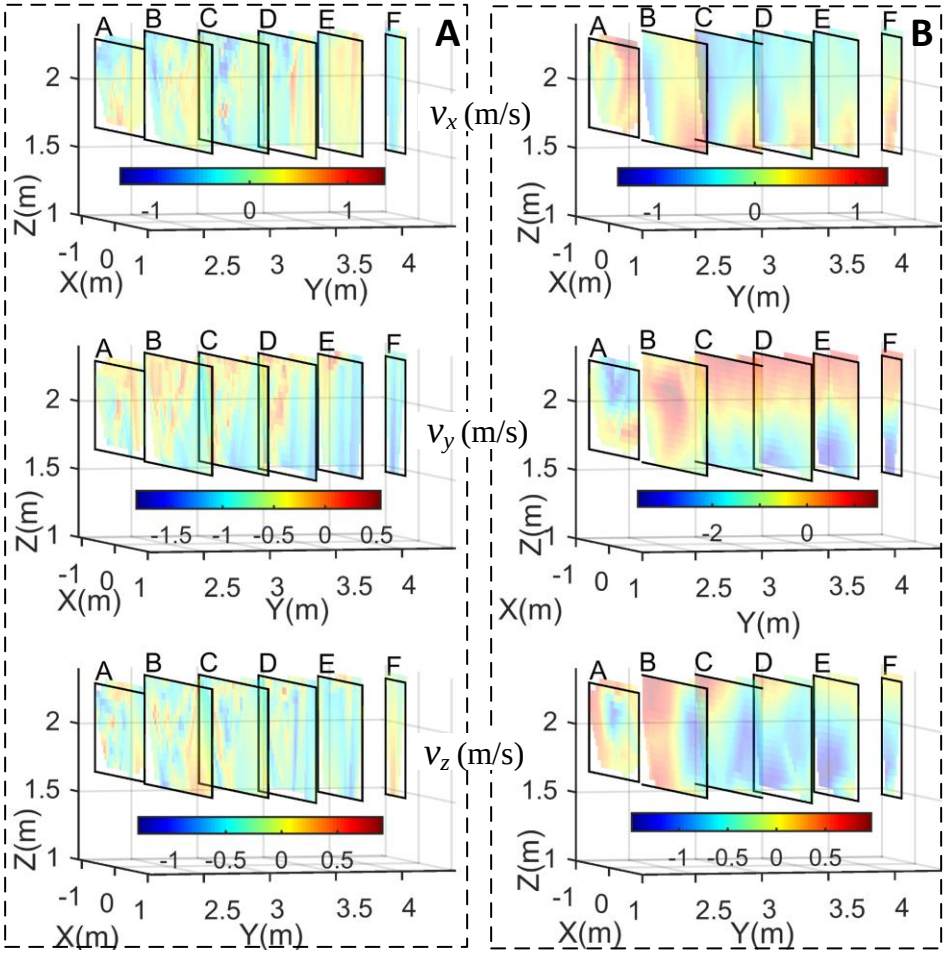

Figure 5.9: Mean wind flow map using: (A) Proposed system; (B) Anemometer[87].

Figure 5.9 shows the mean (linear) wind flow field in the form of 3D slice plots of the velocity components $\{v_x, v_y, v_z\}$ obtained from the proposed system and the wind map generated using anemometer measurements. For each subplot, the velocity data is plotted on 6 planes (namely A-F representing Y = {2.2, 2.6, 3, 3.4, 3.8, 4.2}) in the XZ planes. Similar to steady-state velocity field, Fig. 5.10 shows wind vorticity $\{\omega_x, \omega_y, \omega_z\}$ distribution obtained from the proposed system and anemometer generated map.

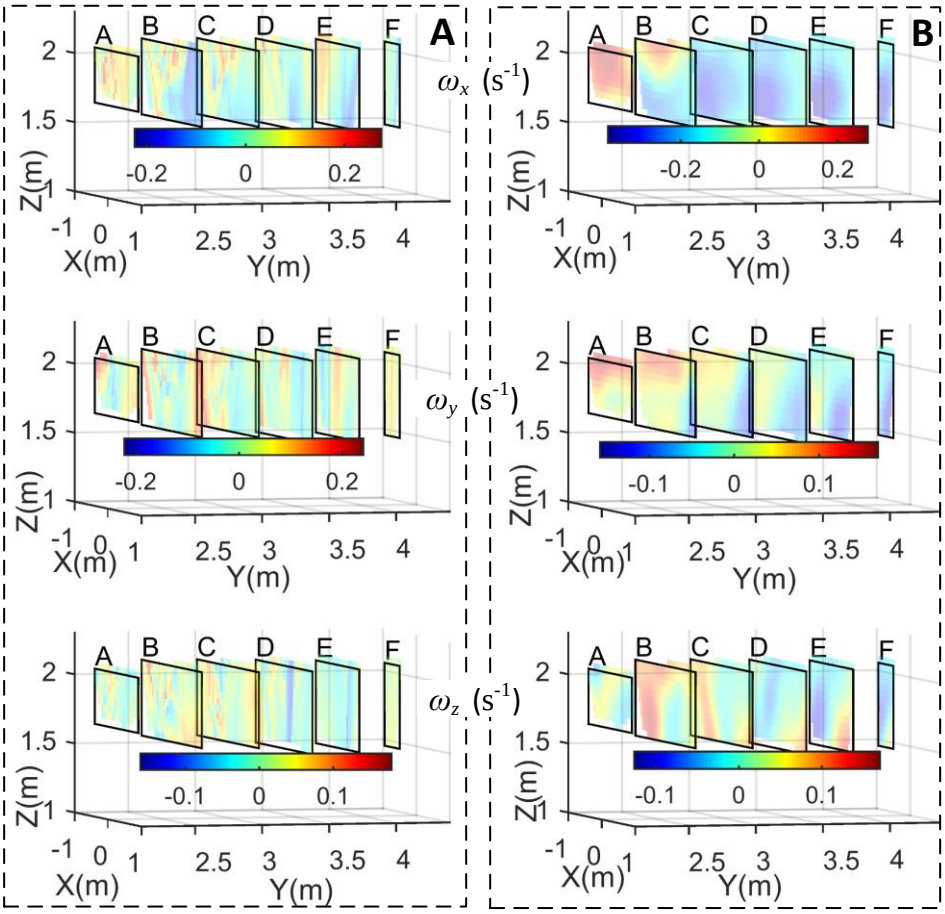

Figure 5.10: Vorticity wind flow map using: (A) Proposed system; (B) Anemometer [87].

The spatial distribution of the wind parameters generated using the RC helicopter demonstrated reasonable accuracy. A good correlation is visible in the v_x, v_y, ω_x, ω_y and ω_z

distributions obtained from the proposed system and anemometer maps. However, no specific wind patterns were observed for the v_z distribution. In addition to this, a high level of discontinuity was also observed in the wind maps obtained from the proposed system.

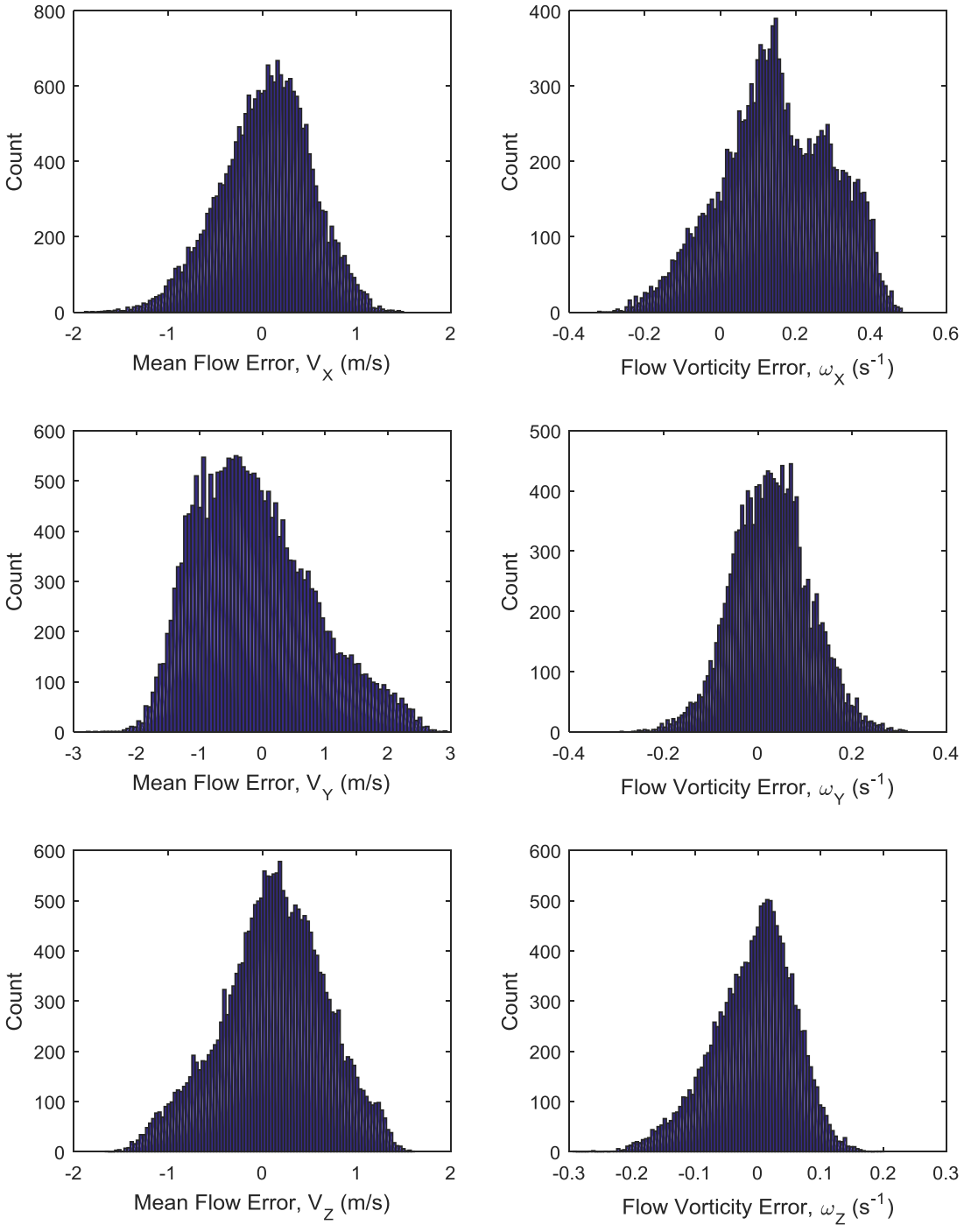

Figure 5.11: Mean flow and vorticity estimation error distribution.

For more quantitative analysis of the wind flow estimates obtained using the proposed system, a point-to-point comparison between the estimated and measured flow components was made in this study. Figure 5.11 shows the error histogram for the mean (linear) flow and vorticity estimates. The ***mean and standard deviation*** values of the estimated error were computed for all six quantities and presented in Table 5.3*:*

Table 5.3: Mean Flow and Vorticity Estimation Error Statistics

Estimation Error Metrics				
	Mean Flow (v) Error (m/s)		**Flow Vorticity (ω) Error (s^{-1})**	
	Mean	*Standard Deviation*	*Mean*	*Standard Deviation*
X Axis	0.0372	0.4761	0.1498	0.1448
Y Axis	-0.1091	0.9299	0.0282	0.0816
Z axis	0.1188	0.5503	-0.0072	0.0645

High standard deviations in the error is a result of high transients visible in the measured quantities shown in Fig 5.9 and Fig 5.10. There are two main reasons behind this behavior:

- In the present study, it was assumed that the rotor wakes are negligible for inflow modelling (visible in v_z distribution).
- Unlike with an anemometer, the helicopter was not stationary during experiments. Therefore, the interpolation process captured the turbulence transients in the dynamics, making the estimates discontinuous.

However, these effects would be less prominent in open areas like ship flight decks. Also, testing the performance against dense velocimetry techniques (like SoDAR/LiDAR) should provide a better assessment of the proposed system in measuring the spatiotemporal aspects of the turbulent wind flow.

CHAPTER 6: CONCLUSION AND FUTURE WORK

This chapter concludes the dissertation with a summary of the current work as well as potential work in the near future.

6.1 Summary

This dissertation is focused on the development and evaluation of an RC helicopter-based instrumentation system for the estimation and mapping of ship airwake. To accomplish this, two separate tracks were explored: one using machine learning for system modeling, and the second using aerodynamic modeling-based state estimation. These approaches were implemented for testing with 3 different iterations of the telemetry system. A comprehensive study of various machine learning algorithms is also presented in this dissertation, with the goal of separating the pilot input component from the airwake component in the helicopter dynamics derived from system measurements. For the calibration of the system, a novel indoor wind mapping system was developed to generate 3D mean wind flow field and turbulence maps. Finally, a novel aerodynamics modelling-based approach was presented in this dissertation to extract 6-parameter wind flow conditions from the system dynamics. Detailed conclusions from the included studies are presented as follows:

- ***Preliminary Investigation*** – demonstrated the effectiveness of an automated method for the analysis of ship airwake data collected using an instrumented RC helicopter. Regions of significant airwake detected by the automated analysis method correspond to such regions predicted by high resolution CFD simulations.

A high correlation between the helicopter's (gyroscopic) vibration patterns and manually detected airwake interaction instances was observed, which corroborated the hypothesis of this research.

- ***Pilot Input Compensation Studies*** – demonstrated a novel use of machine learning tools in separating the components of wind generated helicopter dynamics from IMU measurements. The residual dynamics (hypothesized to be the result of ship airwake) showed a good spatial correlation with the expected patterns generated using CFD models. Two novel telemetry hardware systems were designed, integrated and tested in multiple studies. In addition to Artificial Neural Network (ANN), Bayesian Mixture of Experts (BME) and Adaptive Neuro-Fuzzy Inference Systems (ANFIS) were also examined to model the helicopter's rotational dynamics as a function of pilot inputs and other states. It was observed the ANNs outperform BME and ANFIS in nonlinear regression problems. Also, the discontinuities in the airwake patterns generated in the presented study also suggested that the system responds to instantaneous (unsteady) wind conditions. This study concluded that a temporal component of wind should be added in the airwake description.
- ***Indoor Motion Tracking*** – presented a novel indoor motion tracking system using an anemometer and helicopter (linear and rotational) motion analysis for wind mapping. The proposed motion tracking device achieved mm level accuracy with a field of view of 90˚ and update rate in excess of 300 Hz.
- ***Calibrated Wind Estimation Studies*** – used temporal standard deviation in the wind measurements to quantify airwake intensities and attempted to compare it

against temporal standard deviation in measured dynamics residuals (after subtracting neural networks prediction from measured dynamics). This study demonstrated a very good correlation between the expected and the estimated wind patterns, after minimizing the effects of temporal uncertainty in wind conditions. The outdoor results also showed good relationship with the CFD generated spatial airwake maps. A separate study also corroborated the same conclusion, where ANNs were used to directly predict wind vorticities from helicopter dynamics.

- ***Dynamic modelling of Airwake-Helicopter Interaction*** – demonstrated a novel dynamic modeling of RC helicopter (with 30 states) in a 6-parameter wind environment. Critical effects like rotor dynamics, fuselage/empennage dynamics, inducted rotor inflow and flybar dynamics were modelled to estimate the relationship between the wind condition parameters and measured fuselage dynamics.

With the capability to measure both steady state flow and vorticity components of the wind flow, the proposed systems offer a safe and low cost platform for the testing of control strategies for autonomous operations of helicopters in turbulent environments for both military and civilian applications.

6.2 System Limitations and Future Work

Despite excellent modelling results from the various studies presented in this dissertation, several shortcomings were observed which can be addressed in future work. The most important, along with possible future improvements, are described as follows:

- ***Limited Indoor Wind Map*** – The measured (ground truth) indoor wind map was generated using two opposing fans at different height. The wind flow generated using this indoor setup provided a comparatively small test volume to fly in. A better test setup would be composed of the multiple wind circulation fans (arranged in line) to increase the test volume for the helicopter.
- ***Indoor Positioning Limitations*** – The field of view of the proposed indoor positioning system was another issue which limited the test volume for the calibration experiment. An expandable LOSA motion tracking system is in active development, which should increase the field of view of the system significantly by incorporating multiple trackers.
- ***Rotor Wakes*** – Throughout this research it has been assumed that the rotor downwash does not recirculate and affect the rotor inflow. However this is only true if the helicopter does not decrease altitude and flies at significant height from the ground. This issue can be minimized by increasing the height of the test fans and hence increasing the operational height of the experiment. Also, rotor wake propagation models may also be explored and incorporated into the rotor inflow models to further mitigate this issue.
- ***Autonomous Helicopter Sensing*** – In the presented research, the helicopter was operated by experienced pilots. This results in the pilot's subject bias in deciding the helicopter's trajectory. Autonomous helicopter control strategies may explored in future to make the wind mapping using this research an autonomous and uniformly (spatially) distributed process.

REFERENCES

[1] C. E. Tinney and L. S. Ukeiley, "A study of a 3-D double backward-facing step," *Exp. Fluids*, vol. 47, no. 3, pp. 427–438, 2009.

[2] NAVAIR, "Helicopter operating procedures for air-capable ships NATOPS manual," 2003.

[3] M. R. Snyder, H. S. Kang, C. J. Brownell, L. Luznik, D. S. Miklosovic, J. S. Burks, and C. H. Wilkinson, "USNA Ship Air Wake Program Overview," in *29th AIAA Applied Aerodynamics Conference*, 2011, no. June, pp. 1–12.

[4] M. J. Guillot, "Computational Simulation of the Air Wake over a Naval Transport Vessel," *AIAA J.*, vol. 40, no. 10, pp. 2130–2133, Oct. 2002.

[5] D. Lee, J. Horn, N. Sezer-Uzol, and L. Long, "Simulation of Pilot Control Activity During Helicopter Shipboard Operations," in *AIAA Atmospheric Flight Mechanics Conference and Exhibit*, 2003.

[6] D. Lee, N. Sezer-Uzol, J. F. Horn, and L. N. Long, "Simulation of helicopter shipboard launch and recovery with time-accurate airwakes," in *AHS 53th Annual Forum of the American Helicopter Society*, 2003, vol. 42, no. 2, pp. 448–461.

[7] S. Polsky, R. Imber, R. Czerwiec, and T. Ghee, "A Computational and Experimental Determination of the Air Flow Around the Landing Deck of a US Navy Destroyer (DDG): Part II," in *37th AIAA Fluid Dynamics Conference and Exhibit*, 2007, no. June, pp. 1–12.

[8] D. M. Roper, I. Owen, G. D. Padfield, and S. J. Hodge, "Integrating CFD and piloted simulation to quantify ship-helicopter operating limits," *Aeronaut. J.*, vol. 110, no.

1109, pp. 419–428, 2006.

[9] A. Sharma and L. N. Long, “Airwake Simulation on an LPD 17 Ship,” *AIAA Pap.*, vol. 2589, no. June, p. 11, 2001.

[10] M. J. Guillot and M. A. Walker, “Unsteady analysis of the air wake over the LPD-16,” in *18th Applied Aerodynamics Conference*, 2000.

[11] A. Kumar, P. Ben-Tzvi, M. R. Snyder, and W. Saab, “Instrumentation system for ship air wake measurement,” in *ROSE 2013 - 2013 IEEE International Symposium on Robotic and Sensors Environments, Proceedings*, 2013, no. Code 351, pp. 118–123.

[12] M. R. Snyder, H. S. Kang, and J. S. Burks, “Comparison of Experimental and Computational Ship Air Wakes for a Naval Research Vessel,” in *Proc. 30th AIAA Applied Aerodynamics Conf.*, 2012, no. January, pp. 1–25.

[13] T. D. Ngo and C. Sultan, “Model Predictive Control for Helicopter Shipboard Operations in the Ship Airwakes,” *J. Guid. Control. Dyn.*, vol. 39, no. 3, pp. 574–589, 2016.

[14] R. Bardera-Mora, M. A. Barcala-Montejano, A. Rodríguez-Sevillano, G. G. de Diego, and M. R. de Sotto, “A spectral analysis of laser Doppler anemometry turbulent flow measurements in a ship air wake,” in *Proc. Inst. Mech. Eng. Part G J. Aerosp. Eng.*, 2015, vol. 0, no. 0, pp. 1–12.

[15] M. J. M. Guedes, M. A. da C. Vieira, E. R. Martins, and L. Moraes, “Brazilian Navy Air Wake Program,” in *AIAA Modeling and Simulation Technologies Conference*, 2012, no. August, pp. 1–8.

[16] A. J. Wadcock, G. K. Yamauchi, J. T. Heineck, M. J. Silva, and K. R. Long, “PIV

measurements of the wake of a tandem-rotor helicopter in proximity to a ship," *Am. Helicopter Soc. Aeromechanics Spec. Forum*, pp. 1–23, 2004.

[17] C. H. Kääriä, Y. Wang, G. D. Padfield, J. S. Forrest, and I. Owen, "Aerodynamic Loading Characteristics of a Model-Scale Helicopter in a Ship's Airwake," *J. Aircr.*, vol. 49, no. 5, pp. 1271–1278, Sep. 2012.

[18] B. Allotta, L. Pugi, T. Massai, E. Boni, F. Guidi, and M. Montagni, "Design and calibration of an innovative ultrasonic, arduino based anemometer," in *Conference Proceedings - 2017 17th IEEE International Conference on Environment and Electrical Engineering and 2017 1st IEEE Industrial and Commercial Power Systems Europe, EEEIC / I and CPS Europe 2017*, 2017.

[19] M. R. Snyder, H. S. Kang, C. J. Brownell, and J. S. Burks, "Validation of Ship Air Wake Simulations and Investigation of Ship Air Wake Impact on Rotary Wing Aircraft," *Am. Soc. Nav. Eng. Launch Recover. Symp.*, p. 18, 2012.

[20] M. R. Snyder, A. Kumar, P. Ben-Tzvi, and H. S. Kang, "Validation of Computational Ship Air Wakes for a Naval Research Vessel," in *Proc. 51st AIAA Aerospace Sciences Meeting*, 2013, no. January, pp. 1–25.

[21] C. J. Brownell, L. Luznik, M. R. Snyder, H. S. Kang, and C. H. Wilkinson, "In Situ Velocity Measurements in the Near-Wake of a Ship Superstructure," *J. Aircr.*, vol. 49, no. 5, pp. 1440–1450, 2012.

[22] C. J. Mallon, B. J. Muthig, K. Gamagedara, K. Patil, C. Friedman, T. Lee, and M. R. Snyder, "Measurements of Ship Air Wake Using Airborne Anemometers," in *55th AIAA Aerospace Sciences Meeting*, 2017, no. January, pp. 1–12.

[23] K. Gamagedara, K. Patil, T. Lee, and M. R. Snyder, "Vision-Based Relative

Localization for Airborne Measurements of Ship Air Wake," *2018 AIAA Atmos. Flight Mech. Conf.*, no. January, pp. 1–15, 2018.

[24] J. Gonzalez-Rocha, C. A. Woolsey, C. Sultan, S. de Wekker, and N. Rose, "Measuring Atmospheric Winds from Quadrotor Motion," in *AIAA Atmospheric Flight Mechanics Conference*, 2017, no. January, pp. 1–22.

[25] D. Phelps, K. Gamagedara, J. Waldron, K. Patil, and M. Snyder, "Ship Air Wake Detection Using Small Fixed Wing Unmanned Aerial Vehicle," *2018 AIAA Aerosp. Sci. Meet.*, no. January, pp. 1–11, 2018.

[26] L. Rodriguez, J. A. Cobano, and A. Ollero, "Wind characterization and mapping using fixed-wing small unmanned aerial systems," in *2016 International Conference on Unmanned Aircraft Systems (ICUAS)*, 2016, pp. 178–184.

[27] J. D. Metzger, "Measurement of Ship Air Wake Impact on a Remotely Piloted Aerial Vehicle," 2012.

[28] A. Kumar and P. Ben-tzvi, "Extraction of Impact of Wind Turbulence on RC Helicopters using Machine Learning," in *ASME International Design Engineering Technical Conference*, 2016, pp. 1–7.

[29] M. R. Snyder, A. Kumar, and P. Ben-Tzvi, "Off Ship Measurement of Ship Air Wakes Using Instrumented Unmanned Aerial Vehicles," in *AIAA Applied Aerodynamics Conference*, 2014, no. June, pp. 1–9.

[30] A. Kumar, P. Ben-Tzvi, W. Saab, and M. R. Snyder, "Wireless telemetry system for real-time estimation of ship air wakes with UAVs," *Mechatronics*, vol. 36, pp. 18–26, 2016.

[31] A. Kumar, P. Ben-Tzvi, and M. R. Snyder, "UAV-based Wireless Telemetry System

for the Estimation of Ship Air Wake Patterns," in *ASME International Design Engineering Technical Conference & Computers and Information in Engineering Conference*, 2015, pp. 1–7.

[32] R. Rojas, *Neural Networks - A Systematic Introduction*. Springer-Verlag New York, 1996.

[33] S. Haykin, *Neural Networks: A Comprehensive Foundation*. Prentice-Hall, Englewood Cliffs, NJ, 1999.

[34] P. K. Simpson, *Artificial Neural Systems*. Pergmon Press Elmsford, New York, 1989.

[35] E. D. Karnin, "A simple procedure for pruning back-propagation trained neural networks," *IEEE Trans. Neural Networks*, vol. 1, no. 2, pp. 239–242, Jun. 1990.

[36] R. Kohavi, "A Study of Cross-Validation and Bootstrap for Accuracy Estimation and Model Selection," in *International Joint Conference on Artificial Intelligence*, 1995, vol. 14, no. 12, pp. 1137–1143.

[37] G. D. Padfield, *Helicopter Flight Dynamics: The Theory and Application of Flying Qualities and Simulation Modelling*, 2nd ed. Oxford UK: Blackwell Publishing, 2007.

[38] A. Y. Ng, A. Coates, M. Diel, V. Ganapathi, J. Schulte, B. Tse, E. Berger, and E. Liang, "Autonomous Inverted Helicopter Flight via Reinforcement Learning," in *Experimental Robotics IX. Springer Trackts in Advanced Robotics*, M. H. Ang and K. O., Eds. Springer, Berlin, Heidelberg, 2006, pp. 363–372.

[39] J. Seddon, *Basic Helicopter Aerodynamics.pdf*. BSP Professional Books, Oxford, 1990.

[40] K. Levenberg, “A method for the solution of certain non-linear problems in least squares,” *Q. Appl. Math.*, vol. 2, no. 2, pp. 164–168, Jul. 1944.

[41] D. W. Marquardt, “An Algorithm for Least-Squares Estimation of Nonlinear Parameters,” *J. Soc. Ind. Appl. Math.*, vol. 11, no. 2, pp. 431–441, Jun. 1963.

[42] C. M. Bishop and M. Svensen, “Bayesian Hierarchical Mixtures of Experts,” *Proc. Ninet. Conf. Uncertain. Artif. Intell.*, pp. 57–64, 2003.

[43] K. Murphy, “The Bayes Net Toolbox for Matlab,” *Comput. Sci. Stat.*, vol. 32, no. 2, pp. 1024–1034, 2001.

[44] J.-S. R. Jang, “ANFIS: adaptive-network-based fuzzy inference system,” *IEEE Trans. Syst. Man. Cybern.*, vol. 23, no. 3, pp. 665–685, 1993.

[45] Z. He, X. Wen, H. Liu, and J. Du, “A comparative study of artificial neural network, adaptive neuro fuzzy inference system and support vector machine for forecasting river flow in the semiarid mountain region,” *J. Hydrol.*, vol. 509, pp. 379–386, Feb. 2014.

[46] G. Welch and E. Foxlin, “Motion tracking: no silver bullet, but a respectable arsenal,” *IEEE Comput. Graph. Appl.*, vol. 22, no. 6, pp. 24–38, Nov. 2002.

[47] H. Liu, H. Darabi, P. Banerjee, and J. Liu, “Survey of Wireless Indoor Positioning Techniques and Systems,” *IEEE Trans. Syst. Man Cybern. Part C (Applications Rev.*, vol. 37, no. 6, pp. 1067–1080, Nov. 2007.

[48] Y. Gu, A. Lo, and I. Niemegeers, “A survey of indoor positioning systems for wireless personal networks,” *IEEE Commun. Surv. Tutorials*, vol. 11, no. 1, pp. 13–32, 2009.

[49] J. P. Rolland, Y. Baillot, and A. A. Goon, “A Survey of Tracking Technology for

Virtual Environments," *Fundam. Wearable Comput. Augment. Real.*, pp. 69–112, 2001.

[50] K. Murakami, T. Hasegawa, K. Shigematsu, F. Sueyasu, Y. Nohara, Byong Won Ahn, and R. Kurazume, "Position tracking system of everyday objects in an everyday environment," in *2010 IEEE/RSJ International Conference on Intelligent Robots and Systems*, 2010, pp. 3712–3718.

[51] S. Song, H. Ren, and H. Yu, "An Improved Magnetic Tracking Method Using Rotating Uniaxial Coil With Sparse Points and Closed Form Analytic Solution," *IEEE Sens. J.*, vol. 14, no. 10, pp. 3585–3592, Oct. 2014.

[52] P. W. Schönle, K. Gräbe, P. Wenig, J. Höhne, J. Schrader, and B. Conrad, "Electromagnetic articulography: Use of alternating magnetic fields for tracking movements of multiple points inside and outside the vocal tract," *Brain Lang.*, vol. 31, no. 1, pp. 26–35, May 1987.

[53] C. Hu, M. Li, S. Song, W. Yang, R. Zhang, and M. Q.-H. Meng, "A Cubic 3-Axis Magnetic Sensor Array for Wirelessly Tracking Magnet Position and Orientation," *IEEE Sens. J.*, vol. 10, no. 5, pp. 903–913, May 2010.

[54] Zhuxin Dong, U. C. Wejinya, and W. J. Li, "An Optical-Tracking Calibration Method for MEMS-Based Digital Writing Instrument," *IEEE Sens. J.*, vol. 10, no. 10, pp. 1543–1551, Oct. 2010.

[55] R. Zhang, F. Hoflinger, and L. Reindl, "Inertial Sensor Based Indoor Localization and Monitoring System for Emergency Responders," *IEEE Sens. J.*, vol. 13, no. 2, pp. 838–848, Feb. 2013.

[56] G. V. Zàruba, M. Huber, F. A. Kamangar, and I. Chlamtac, "Indoor location tracking

using RSSI readings from a single Wi-Fi access point," *Wirel. Networks*, vol. 13, no. 2, pp. 221–235, Apr. 2007.

[57] X. Luo, W. J. O'Brien, and C. L. Julien, "Comparative evaluation of Received Signal-Strength Index (RSSI) based indoor localization techniques for construction jobsites," *Adv. Eng. Informatics*, vol. 25, no. 2, pp. 355–363, Apr. 2011.

[58] A. Erol, G. Bebis, M. Nicolescu, R. D. Boyle, and X. Twombly, "Vision-based hand pose estimation: A review," *Comput. Vis. Image Underst.*, vol. 108, no. 1–2, pp. 52–73, Oct. 2007.

[59] R. Hartley and A. Zisserman, *Multiple view geometry in computer vision*. .

[60] C. D. Metcalf, S. V. Notley, P. H. Chappell, J. H. Burridge, and V. T. Yule, "Validation and Application of a Computational Model for Wrist and Hand Movements Using Surface Markers," *IEEE Trans. Biomed. Eng.*, vol. 55, no. 3, pp. 1199–1210, Mar. 2008.

[61] C. Celozzi, G. Paravati, A. Sanna, and F. Lamberti, "A 6-DOF ARTag-based tracking system," *IEEE Trans. Consum. Electron.*, vol. 56, no. 1, pp. 203–210, Feb. 2010.

[62] H. J. Woltring, "New possibilities for human motion studies by real-time light spot position measurement.," *Biotelemetry*, vol. 1, no. 3, pp. 132–46, 1974.

[63] "Motion Capture for Object Tracking and Robotics | VICON." [Online]. Available: https://www.vicon.com/motion-capture/engineering. [Accessed: 04-Feb-2018].

[64] J. Maccormick, "How does the Kinect work?"

[65] R. Xiao, C. Harrison, K. D. D. Willis, S. E. Hudson, and I. Poupyrev, "Lumitrack: Low Cost, High Precision and High Speed Tracking with Projected m-Sequences,"

in *26th Annual ACM Symposium on User interface Software and Technology*, 2013, pp. 3–12.

[66] A. Mohan, G. Woo, S. Hiura, Q. Smithwick, R. Raskar, A. Mohan, G. Woo, S. Hiura, Q. Smithwick, and R. Raskar, "Bokode: imperceptible visual tags for camera based interaction from a distance," in *ACM SIGGRAPH 2009 papers on - SIGGRAPH '09*, 2009, vol. 28, no. 3, p. 1.

[67] A. Kumar and P. Ben-Tzvi, "Spatial Object Tracking System Based on Linear Optical Sensor Arrays," *IEEE Sens. J.*, vol. 16, no. 22, pp. 7933–7940, 2016.

[68] Q. Wen and J. Wu, "Linear CCD Based Optical Tracking Using Stereo Correspondence Algorithm," in *2009 International Conference on Artificial Intelligence and Computational Intelligence*, 2009, pp. 422–425.

[69] Y. Ruichek, "A hierarchical neural stereo matching approach for real-time obstacle detection using linear cameras," in *Proceedings of the 2003 IEEE International Conference on Intelligent Transportation Systems*, pp. 299–304.

[70] J.-C. Burie and J.-G. Postaire, "Enhancement of the road safety with a stereo vision system based on linear cameras," in *Proceedings of Conference on Intelligent Vehicles*, pp. 147–152.

[71] "Teensy USB Development Board." [Online]. Available: https://www.pjrc.com/teensy/index.html. [Accessed: 05-Feb-2016].

[72] Lord Rayleigh, "On Pin-hole photography," *London, Edinbg. Dublin Philos. Mag. J. Sci.*, vol. 5, no. 31.

[73] X. Yun and E. R. Bachmann, "Design, Implementation, and Experimental Results of a Quaternion-Based Kalman Filter for Human Body Motion Tracking," *IEEE*

Trans. Robot., vol. 22, no. 6, pp. 1216–1227, Dec. 2006.

[74] H. Zhao and Z. Wang, "Motion Measurement Using Inertial Sensors, Ultrasonic Sensors, and Magnetometers With Extended Kalman Filter for Data Fusion," *IEEE Sens. J.*, vol. 12, no. 5, pp. 943–953, May 2012.

[75] VectorNav, "Application Note: Quaternion Math." [Online]. Available: https://www.vectornav.com/docs/default-source/documentation/vn-100-documentation/AN002.pdf?sfvrsn=10. [Accessed: 04-Feb-2018].

[76] VectorNav, "VN-200 Specifications - VectorNav Technologies." [Online]. Available: https://www.vectornav.com/products/vn-200/specifications. [Accessed: 04-Feb-2018].

[77] A. Kumar and P. Ben-Tzvi, "An Inertial Sensor To Measure Wind Turbulence With RC Helicopters," in *Proceedings of the ASME 2017 Dynamic Systems and Control Conference*, 2017, pp. 2–7.

[78] "R. M. Young Company Ultrasonic Anemometer - Model 81000." [Online]. Available: http://www.youngusa.com/products/6/3.html. [Accessed: 16-Sep-2016].

[79] A. Kumar and P. Ben-Tzvi, "Novel Wireless Sensing Platform for Experimental Mapping and Validation of Ship Air Wake (Accepted for Publication, March 2018)," *Mechatronics*, 2018.

[80] C. M. Bishop, *Pattern Recognition and Machine Learning*, vol. 1. Springer-Verlag New York, 2006.

[81] M. Clerc and J. Kennedy, "The particle swarm-explosion, stability, and convergence in a multidimensional complex space," *IEEE Trans. Evol. Comput.*, vol. 6, no. 1, pp. 58–73, 2002.

[82] J. Malik, R. Mishra, and I. Singh, "PSO-ANN Approach For Estimating Drilling Induced Damage In Cfrp Laminates," *Adv. Prod. Eng. Manag. APEM*, vol. 6, no. 2, pp. 95–104, 2011.

[83] Martin A. Fischler and R. C. Bolles, "Random Sample Consensus: A Paradigm for Model Fitting with Applications to Image Analysis and Automated Cartography," *Comm. ACM*, vol. 24, no. 6, pp. 381–395, 1981.

[84] B. Sunden, "VORTEX SHEDDING," in *A-to-Z Guide to Thermodynamics, Heat and Mass Transfer, and Fluids Engineering*, Begellhouse.

[85] J. Lusardi, "Control equivalent turbulence input model for the UH-60 helicopter," University of California, Davis, 2004.

[86] R. T. N. Chen, "A survey of nonuniform inflow models for rotorcraft flight dynamics and control applications," *Nasa Tech. Memo.*, vol. 14, no. 2, pp. 147–184, 1990.

[87] A. Kumar and P. Ben-Tzvi, "Estimation of Wind Conditions Utilizing RC Helicopter with Active Particle Filters," *IEEE/ASME Trans. Mechatronics (Submitted 2018)*, 2018.

[88] R. Cunha and C. Silvestre, "Dynamic Modeling and Stability Analysis of Model-Scale Helicopters with Bell-Hiller Stabilizing Bar," *AIAA Guid. Navig. Control Conf. Exhib.*, no. August, pp. 1–11, 2003.

[89] D. A. Spera, "Models of Lift and Drag Coefficients of Stalled and Unstalled Airfoils in Wind Turbines and Wind Tunnels," 2008.

[90] J. A. Demoss, "Drag Measurements on an Ellipsoidal Body," Virginia Polytechnic Institute and State University, 2007.

[91] Vishay, “TSMP6000: IR Sensor Module for Remote Control Systems.” [Online]. Available: https://www.vishay.com/docs/82620/tsmp6000.pdf. [Accessed: 20-May-2017].

[92] M. S. Arulampalam, S. Maskell, N. Gordon, and T. Clapp, “A tutorial on particle filters for online nonlinear/nongaussian bayesian tracking,” *IEEE Trans. Signal Process.*, vol. 50, no. 2, pp. 723–737, 2002.